
# Turbulent Kinetic Energy Dissipation Rate in the Rhine Region of Freshwater Influence

Diploma Thesis

Elisabeth Fischer

# Turbulent Kinetic Energy Dissipation Rate in the Rhine Region of Freshwater Influence

Diploma Thesis

at the
Leibniz Institute for Baltic Sea Research
Department of Physical Oceanography and Instrumentation

by Elisabeth Fischer

University of Rostock
Faculty of Mathematics and Natural Sciences
Institute of Physics

| | |
|---|---|
| Supervisor and First Reviewer: | Prof. Dr. Hans Burchard<br>Leibniz Institute for Baltic Sea Research<br>Warnemünde, Germany |
| Second Reviewer: | Dr. Alejandro J. Souza<br>Proudman Oceanographic Laboratory<br>Liverpool, UK |

Rostock, 5 January 2009

# Contents

# Preface

## Annotation

The reader interested in the main results of this work is referred to chapter 5. That chapter corresponds to a large extent with a paper submitted to the PECS 2008 special issue of *Ocean Dynamics*. The authors of that paper are Elisabeth Fischer[1], Hans Burchard[1] and Robert D. Hetland[2] from the following institutions:

1. Leibniz Institute for Baltic Sea Research Warnemünde,
   Seestrasse 15, 18119 Rostock, Germany

2. Department of Oceanography, Texas A&M University,
   3158 TAMU, College Station TX 77845, USA

The first two paragraphs of section 5.4 have been written by Hans Burchard; the remainder is entirely the writing of Elisabeth Fischer.
In order to maintain the self-contained independence of the paper as well as the role of its first three sections as a summary of the chapters 1 and 2, a certain overlapping with the preceding chapters has been accepted.
The pdf file of this diploma thesis can be found on the follwing website:
`http://www.io-warnemuende.de/homepages/wgburchard/index.php?Itemid=83`
After acceptance, the original publication (chapter 5) will be available at:
`http://www.springerlink.com`

## Nomenclature

Numbers are stated with a point as decimal separator and a comma as thousands separator.
For proper names of countries, cities, rivers etc., the English term is used if available. The German and Dutch waters in the sections 1.1 and 1.2 are denoted by their native names in *italic* type; mostly a literal interpretation is added in parentheses and quotation marks.
Besides generally known abbreviations, formula symbols and units of measurement, the following nomenclature is applied:

| | |
|---|---|
| $\varepsilon = \varepsilon_m$ | turbulent kinetic energy dissipation rate per unit mass $(\mathrm{W/kg} = \mathrm{m^2/s^3})$ |
| $\varepsilon_V$ | turbulent kinetic energy dissipation rate per unit volume $(\mathrm{W/m^3} = \mathrm{kg/(ms^3)})$ |
| GETM | General Estuarine Transport Model |
| GOTM | General Ocean Turbulence Model |
| HW | high water |
| LW | low water |
| $\mathrm{mab}$ | metres above the bottom/bed |
| $\mathrm{mbs}$ | metres below the surface |
| ROFI | region of freshwater influence |
| SIPS | strain-induced periodic stratification |
| $\mathrm{TKE}$ | turbulent kinetic energy |

# Part I

# Introduction, Observations and Method

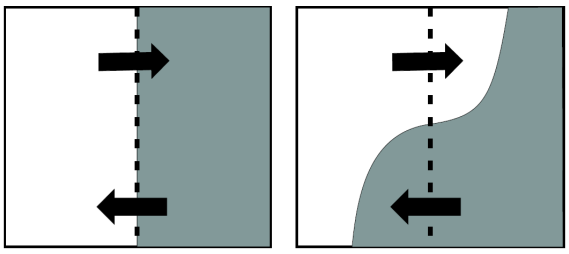

# Chapter 1

# General Information on the Rhine

**Figure 1.1:** Satellite image of the North Sea and the Southern Bight.
(For maps with geographical coordinates, see Fig.s 1.4 and 5.1.)
(`http://commons.wikimedia.org/wiki/Image:NASA_NorthSea1_2.jpg`)

With a length of approximately $1,320\ \mathrm{km}$ and an average discharge of $2,200\ \mathrm{m^3/s}$ (before the delta), the Rhine river is one of the longest and most important European rivers as well as the biggest North Sea inflow. It is a significant waterway for economy and tourism, but also a natural habitat for many plants and animals.
This chapter provides general information on the course, the drainage basin and the discharge of the river, on its influence on the Southern Bight of the North Sea and on its relevance for the coastal ecosystem.

# 1.1 River Course and Drainage Basin

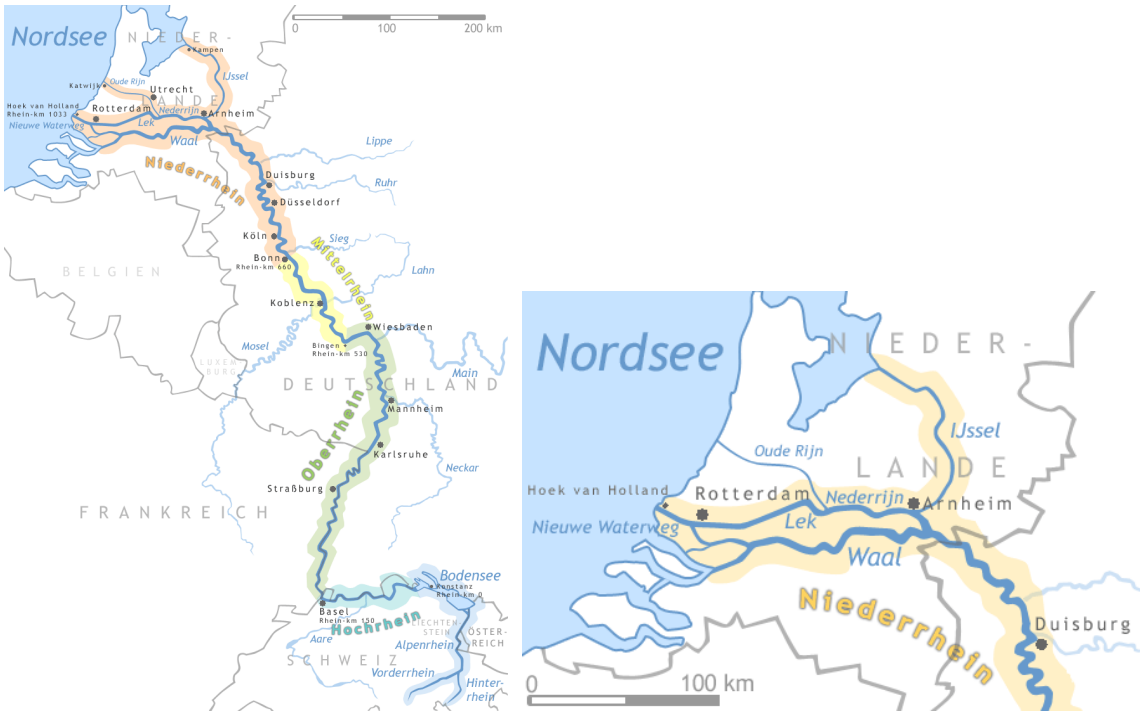


**Figure 1.2:** Rhine river course and delta (`http://en.wikipedia.org/wiki/Rhine`)

The Rhine (Fig. 1.2) rises in Switzerland, flows through Lake Constance and *Untersee* ("Lower Lake"), then along the border between Switzerland and Germany and, turning around the so-called Rhine knee, along the southern part of the Franco-German border. After having entered Germany, the Rhine turns northeastward until it crosses the Dutch border, after which the Rhine-Meuse-Scheldt delta begins. The Rhine splits up into the *Waal*, the *Nederrijn* ("Lower Rhine") and the *IJssel*. The *Waal*, which carries approximately two-thirds of the Rhine water, partly flows into the *Hollands Diep* ("Holland's Deep") strait and partly re-merges with the *Nederrijn* (two-ninths of the Rhine water), which is now called *Lek* ("Waterway"). The latter flows through the *Nieuwe Waterweg* ("New Waterway", also Rotterdam Waterway) into the North Sea; the *Hollands Diep*, into which the Meuse river discharges $250\ \mathrm{m}^3/\mathrm{s}$ on average[1], is connected to the North Sea via the *Haringvliet* ("Herring Rivulet") strait, but the *Haringvliet* dam limits the water exchange (see sec. 1.2).
The Rhine's drainage basin of $185,000\ \mathrm{km}^2$ covers area of nine countries[2]: The biggest of them comprises $100,000\ \mathrm{km}^2$, i.e. approximately $28\%$, of Germany; smaller parts fall upon Switzerland, France and the Netherlands (between $20,000$ and $30,000\ \mathrm{km}^2$ each); the remainder is distributed among Austria, Luxembourg (approximately $2,500\ \mathrm{km}^2$

[1] `http://www.geo.uu.nl/fg/palaeogeography/rhine-meuse-delta`
[2] areas according to the International Commission for the Protection of the Rhine, `http://www.iksr.org/index.php?id=117`

each), Italy, Liechtenstein and Belgium.
The drainage basin of the $925\ \mathrm{km}$ long Meuse river covers an area of approximately $35,000\ \mathrm{km}^2$, which is distributed as follows[3]: Belgium $14,000\ \mathrm{km}^2$, France $9,000\ \mathrm{km}^2$, the Netherlands $8,000\ \mathrm{km}^2$, Germany $4,000\ \mathrm{km}^2$ and Luxembourg less than $500\ \mathrm{km}^2$.

## 1.2 Artificial Constructions in the Rhine-Meuse-Scheldt Delta


**Figure 1.3:** Dams in the Rhine-Meuse-Scheldt delta (`http://www.deltawerken.com/The-Works/318.html`)

Already in the 13th century people began to modify the Rhine-Meuse-Scheldt delta by erecting dikes in order to protect the land, most of which lies beneath the sea level, against the water. As settlement and urbanisation increased over the years, so did economic and social requirements, namely flood protection, freshwater supply and navigation (Backx et al., 2002). Hence, the Rhine branches were more and more canalised and re-routed by dams to meet these needs so that today there is no natural river delta left in the Netherlands.
The most severe structural alterations were decided by the Deltacommission[4] founded

[3] `http://nl.wikipedia.org/wiki/Stroomgebied_van_de_Maas`
[4] `http://www.deltawerken.com`

in February 1953, the month of one of the biggest floods in the history of the Netherlands. Its Deltaplan involved the following Deltaworks, among others (also see Fig. 1.3): damming the *Zandkreek*, the *Veerse Gat*, the *Grevelingen*, the *Volkerak*, the *Haringvliet* and the *Brouwershavense Gat*, as well as the storm surge barriers in the *Hollandse IJssel* and at the *Oosterschelde* (original plans for a dam revised in 1976).
Of these buildings, the $5\ \mathrm{km}$ long *Haringvliet* dam is of most interest for the Rhine and Meuse outflow because its 17 sluices ($62\ \mathrm{m}$ each) are operated to regulate the discharge through the New Waterway (de Ruijter et al., 1992): In order to prevent salt-water intrusions, a runoff of $1,500\ \mathrm{m^3/s}$ is aimed at. In case of higher outflows, the remainder passes the opened sluices into the North Sea. However, if the rivers' discharge exceeds $6,000\ \mathrm{m^3/s}$, additional water masses flow through the New Waterway (also see Fig. 1.5(b)).

## 1.3 Details on the Rhine Discharge and its Influencing Factors

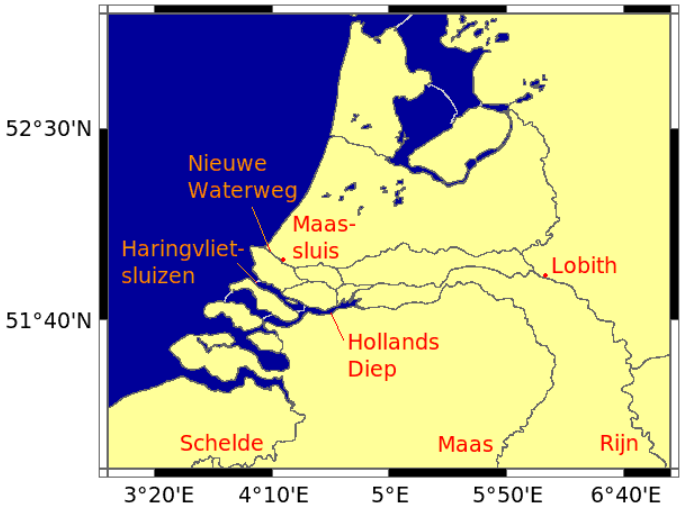


**Figure 1.4:** Map of the Rhine-Meuse-Scheldt delta
(adapted from `http://rimmer.ngdc.noaa.gov/mgg/coast/getcoast.html`)

| location | discharge ($\mathrm{m^3/s}$) | | | period |
|---|---|---|---|---|
| | highest | average | lowest | |
| Lobith | $12,600$ | $2,200$ | $620$ | 1901-1990 |
| *Maassluis* | $3,843$ | $1,335$ | $-2,744$ | 1981-1990 |
| *Haringvlietsluizen* | $6,425$ | $785$ | $0$ | 1976-1990 |

**Table 1.1:** Average and extreme discharge values of the Rhine at three different locations (see Fig. 1.4; data from `http://www.waternormalen.nl`). A negative discharge means an upstream flow.

The discharge of the Rhine is highly variable due to its dependence on the weather pattern in the large drainage basin, which extends from the Alpine high mountain range to the North Sea coast. The average discharge at Lobith (before the delta, Fig. 1.4) is $2,200\ \mathrm{m^3/s}$, but minima less than a third of this (e.g. $620\ \mathrm{m^3/s}$ on 4 November 1947) and maxima greater than five times this value (e.g. $12,600\ \mathrm{m^3/s}$ on 3 January 1926) have been observed (Tab. 1.1). Once every ten years[5] the outflow exceeds $9,670\ \mathrm{m^3/s}$, once every $100$ years $12,320\ \mathrm{m^3/s}$ and once every $1,250$ years $15,000\ \mathrm{m^3/s}$.
A river's discharge is determined by the availability of liquid water in its drainage basin, i.e. by the ratio of precipitation and melting on the one hand and evaporation and freezing on the other hand. Consequently, it follows a seasonal cycle as visible in Fig. 1.5(a) for the Rhine. The associated climate is exemplified by Fig. 1.6.
From November to February, minimum temperatures inhibit evaporation and thus enhance the Rhine discharge, though part of the considerable precipitation is stored in snow and ice; in March, rising temperatures cause melting in the low land and mountains and continuously high discharges. Then, from April to May, precipitation increases, but so do temperature and evaporation; the discharge is reduced. In June, snow and ice melting in the high mountains together with maximum precipitation pause this reduction before, from July to August, maximum temperatures and decreasing precipitation minimise the discharge. From September to October, falling temperatures and decreasing precipitation balance each other so that the discharge remains constantly low.
The actual discharge may substantially differ from the mean annual cycle. E.g. in February 1999, heavy snowfall followed by thaw and torrential rain caused a Rhine high water (Fig. 1.5(b)). Three months later, snow melting in the Alps and heavy rain led to peak water gauges along the *Oberrhein* ("Upper Rhine")[6].
Fig. 1.5(b) also shows the discharge through the New Waterway (*Maassluis*) and the *Haringvliet* sluices (*Haringvlietsluizen*). As explained in section 1.2, the latter are operated in order to obtain an outflow of about $1,500\ \mathrm{m^3/s}$ through the New Waterway; e.g., the sluices are opened in February and March and closed in August and September.

## 1.4 Significance for the North Sea and the Dutch Coastal Current

The water masses transported by the Rhine and the Meuse have a direct impact on an approximately $30\ \mathrm{km}$ wide coast-parallel strip of the Southern Bight of the North Sea, which is called a region of freshwater influence (ROFI, term adopted by Simpson et al. (1993); Fig. 1.7). The water column in this $20\ \mathrm{m}$ deep region is determined by an alteration between stratification and vertical homogeneity, which is controlled by tides, wind, waves and variations in river discharge (for details see sec.s 2.4 and 2.5).
Under the influence of the Coriolis force as well as predominant west and southwest

[5] http://www.waternormalen.nl
[6] http://www.3sat.de/nano/bstuecke/63758/index.html

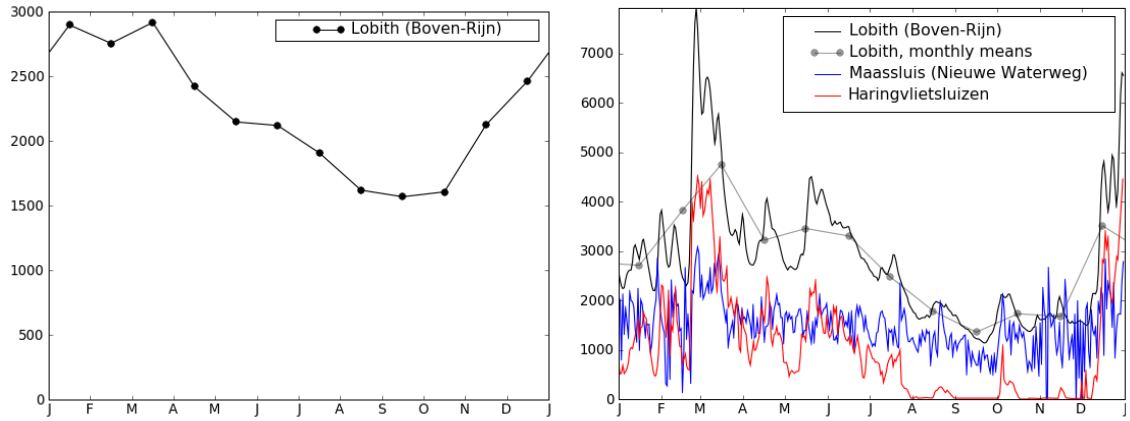


(a) Mean annual cycle (averaged over 1989-2007) of the monthly mean discharges at Lobith.

(b) Cycles of discharge at Lobith, *Maassluis* and the *Haringvlietsluizen* in 1999.

**Figure 1.5:** Annual cycles of the Rhine discharge ($\mathrm{m}^3/\mathrm{s}$) at three different locations (see Fig. 1.4; data from `http://www.waterbase.nl`).

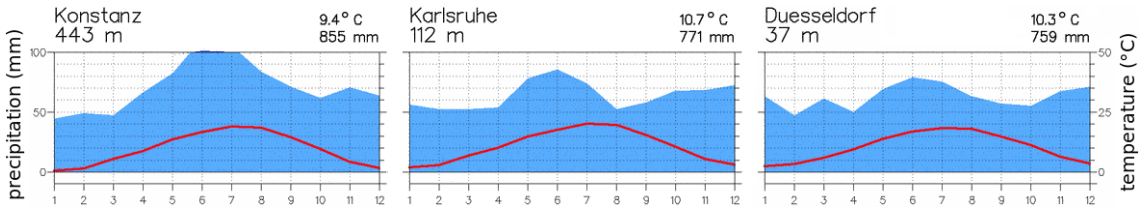


**Figure 1.6:** Climate charts of Konstanz, Karlsruhe (monthly means averaged over 1971-2000) and Düsseldorf (monthly means averaged over 1961-1990) with precipitation (left ordinate, blue background) and temperature (right ordinate, red curve; `http://www.klimadiagramme.de`). The numbers along the abscissa indicate the months of the year.

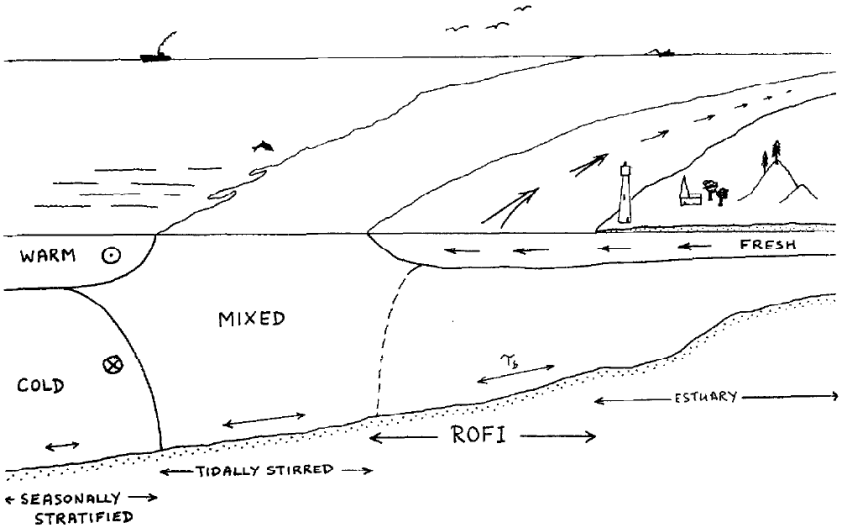


**Figure 1.7:** Schematic of the characteristic regimes of shelf and estuary (Simpson, 1997, Fig. 1)

winds, the Rhine outflow turns right and provides the main freshwater contribution to the wind- and density-driven Dutch coastal current (also see sec. 2.5.2), which extends northeastward and into the German Bight. Here it merges with the freshwater input from the Ems, the Weser and the Elbe and flows along the Danish coast into the *Skagerrak* (Simpson et al., 1993).

## 1.5 Relevance for the Coastal Ecosystem

In a ROFI, the interface between estuary and continental shelf sea, not only freshwater, but also dissolved and particulate matter, e.g. nutrients and anthropogenic contaminants, is exchanged. Especially the large rivers transport high quantities of nutrients and other matter, natural as well as dumped by agriculture and industry, from the continent into the oceans. Stratification and mixing in the ROFI control their accumulation and spreading and, thus, the optical depth of the water column and the primary production (Simpson et al., 1993).
Primary producers[7], also called autotrophs[8], are those organisms which produce organic material from inorganic nutrients, e.g. nitrogen ($\mathrm{N}$) and phosphorus ($\mathrm{P}$); the necessary energy is, in most cases, generated by the photosynthesis of sunlight. Phytoplankton[9] (cyanobacteria, microscopic algae and others) belong to this group of organisms. Zooplankton[10] (jellyfish, krill and others) are the heterotrophic[11] plankton, which live on organic material. An increase of the nutrient input into a water body results in an increased primary production[12] and can have negative effects on the aquatic ecosystem, e.g. high turbidity, depletion of dissolved oxygen and considerable fish kills.
The nutrient load of the Rhine (and of rivers and coastal waters in general) has been reported to have risen in the past 100 years (de Jonge, 1990; Nienhuis, 1992; Laane, 2005). This affects the freshwater ecosystem itself as well as the marine ecosystem; e.g. the gain in phosphate concentration in the Rhine has, via the Rhine branch *IJssel*, significantly stimulated the primary production in the Wadden Sea (de Jonge, 1990). In order to estimate the dimensions of potential hazards, the knowledge and comprehension of the physical processes are essential.

[7] http://en.wikipedia.org/wiki/Primary_producers
[8] http://en.wikipedia.org/wiki/Autotroph
[9] http://en.wikipedia.org/wiki/Phytoplankton
[10] http://en.wikipedia.org/wiki/Zooplankton
[11] http://en.wikipedia.org/wiki/Heterotroph
[12] http://en.wikipedia.org/wiki/Eutrophication

# Chapter 2

# State-of-the-Art

Dutch oceanographers have primarily investigated the Rhine region of freshwater influence (ROFI) in order to establish a suitable coastal zone management. In the eighties and nineties of the 20th century, the area became research subject of many scientists; some of their works' foci are listed below together with references to the sections dealing with the respective topic:

- features of the Rhine river plume and ROFI (sec. 2.2, 2.4)
- circulations and residual currents (sec. 2.1, 2.5.2)
- tides and Kelvin waves (sec. 2.5.3, 2.5.4)
- stratification, current ellipses and tidal straining (sec. 2.5.1, 2.5.5, 2.5.6)
- turbulent kinetic energy dissipation rate (sec. 2.5.7)

A recurring issue is the semi-diurnal cycle of stratification in the Rhine ROFI with stable stratification at high water and mixed water columns at low water (cp. sec. 2.5.6). This is contrary to the stratification pattern occurring in most estuaries, where stratification is maximum at low water, but it can easily be understood when considering the rotary tidal current (sec. 2.5.5).

## 2.1 Estuarine Circulation

An estuary, i.e. the mouth section of a river or a bay which is supplied by a river, is influenced by the river outflow as well as by the seawater. Depending on its width, the freshwater discharge and the salinity, different types of density-driven circulation (Fig. 2.1) develop.
The classical estuarine circulation, referring to the residual, i.e. tidal mean water movement, consists of a downstream current of freshwater at the surface and an upstream current of saline seawater at the bottom: Since density increases with salinity, freshwater is lighter than seawater and thus floats on top, whereas the seawater forms a wedge at the bed. Due to friction, mixing takes place between the buoyant freshwater and the

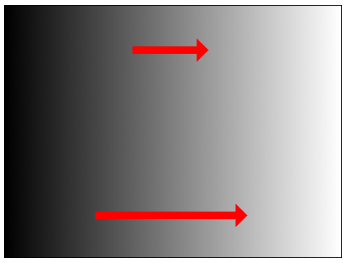

(a) The pressure gradient force is directed from high- to low-density water columns and, like pressure itself, increases with depth.

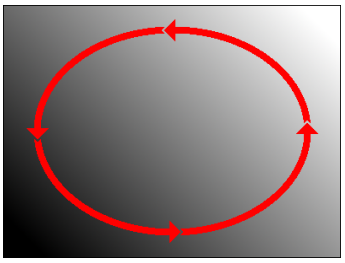

(b) A density-driven circulation is generated, which continues as long as the density gradient is maintained by opposing currents or heat or salt fluxes.

(c) Without opposing currents or heat or salt fluxes (sec. 2.5.1), stable stratification is attained and the circulation stops.

**Figure 2.1:** Schematic of a density-driven circulation forced by horizontal density gradients. Dark shading represents high density and light shading represents low density.

underlying seawater, so that part of the seawater flows out with the freshwater near the surface and needs to be replaced. As counterpart to the river discharge, this exchange flow completes the circulation. However, the time- and depth-averaged current always goes downstream. If the freshwater discharge is very high, the flow may be directed downstream over the whole depth.
In very shallow estuaries with low discharges, especially in arid climates, reverse estuarine circulation occurs: If evaporation rates are higher than freshwater input, the water in the estuary is more saline and thus heavier than the open ocean water. Consequently, seawater flows in at the surface, while bottom currents point downstream.
If the estuary is very wide and the discharge low, salinity and current direction may vary not with depth, but with width: Due to the Coriolis force, the freshwater outflow as well as the seawater inflow are attached to the coast, either on their right- (with respect to the flow direction, northern hemisphere) or on their left-hand side (southern hemisphere). Thus, on one side of the estuary freshwater flows out and on the other side seawater flows in.

## 2.2 Classification of River Plumes

Rivers, coastlines and continental shelf seas may have a lot of different features, e.g. concerning dimensions and shape, discharge, salinity and tidal forcing. Consequently, there are various types of river plumes, i.e. the less dense freshwater from the river overlying the saline seawater. In the following, five possible classification schemes are introduced; their application to the Rhine plume is discussed in section 2.4. Please note that the first four classifications neglect tides.

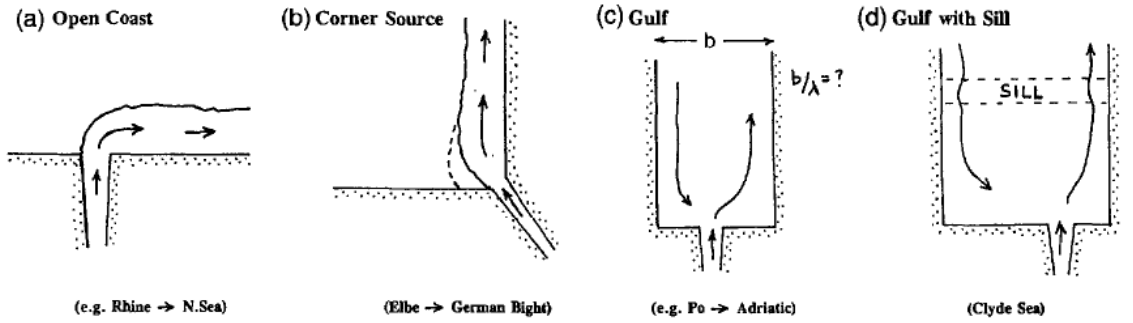


**Figure 2.2:** Topographic constraints of ROFIs. For (c) and (d): $b$ gulf width, $\lambda$ internal Rossby radius, $b/\lambda$ Kelvin number. See text for descriptions. (Simpson, 1997, Fig. 2)

### 2.2.1 Topographic Constraints

The perhaps most obvious differentiation of river plumes is in accordance with topographic constraints, such as coastline shapes and bathymetry in connection with ambient flow. Simpson (1997) gave the following examples (Fig. 2.2):

Open coast: After entering the sea at a straight coastline, the river water is deflected by the Coriolis force, in the northern hemisphere to the right and in the southern hemisphere to the left, and then runs alongside the coast as a coastal current. An ambient flow, e.g. strong coast-parallel wind, may enforce or reverse this current.

Corner source: The river pours in the sea at a (concave) corner of an angled coastline, which limits the plume to a smaller potential extent.

Gulf or bay: The freshwater discharge enters a gulf or bay, the width of which may be small enough (comparable to the internal Rossby radius, i.e. Kelvin number $\approx 1$, see sec. 2.2.3) so that the classical estuarine circulation (cp. sec. 2.1) applies in the gulf or bay. Further limitation by a sill at the open sea boundary may hold back most of the river water and confine the inflow of sea water to a minimum. Thus, no typical salt- and freshwater wedges can develop and only a thin plume floats on the open sea.

### 2.2.2 Outflow Geometry and Recirculating Bulges

A detailed experimental investigation of the influence of outflow geometry on the formation of a recirculating bulge was done by Avicola and Huq (2003b, Fig. 2, 3). A schematic of their experimental setup is shown in Fig. 2.3(a): Through a modifiable bay, freshwater enters into a saltwater basin and forms a plume. In order to simulate the Coriolis force, the basin is mounted on a turntable. Dependent on the bay exit angle and the radius of curvature, the plume may or may not produce a recirculating bulge (Fig. 2.3(b)) before flowing along the coast. The results can be summarised as follows (bay width varied such that the bay exit Kelvin number was of the order of one, see sec. 2.2.3):

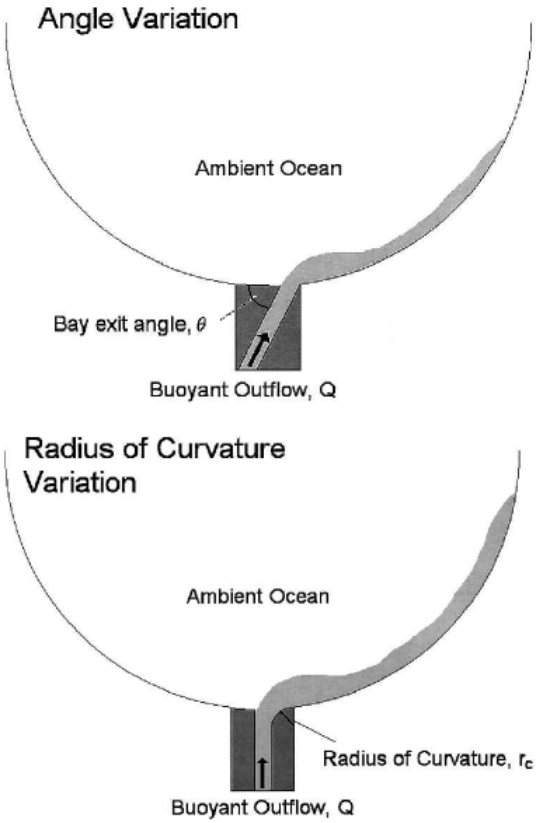


(a) Schematic of the experimental setup (top view)

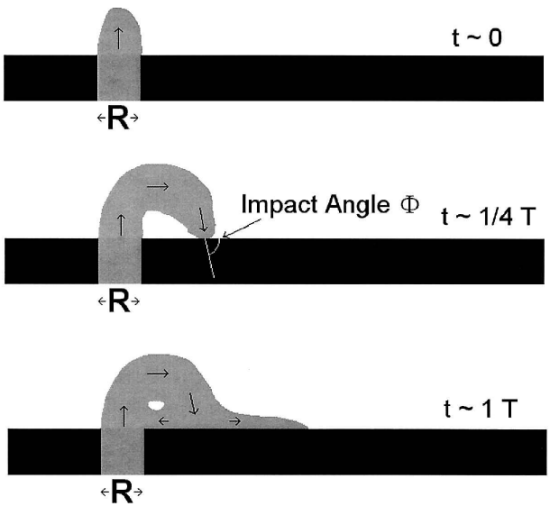


(b) Schematic of the initial stages of a buoyant outflow

**Figure 2.3:** Outflow geometry and its influence on the formation of a recirculating bulge (adapted from Avicola and Huq, 2003b, Fig. 2, 3). See text for details.

Radius of curvature, $r_c$ (bay exit angle $\theta = 90°$): In agreement with former experiments (Bormans and Garrett, 1989), a recirculating bulge forms, if the bay exit Rossby number is greater than one, $\mathrm{Ro} = u/(fr_c) > 1$, where $u$ is the velocity of the fluid turning the corner and $f$ the Coriolis parameter. That is to say, an outflow recirculates due to a high velocity or rather a small radius of curvature, meaning a sharp corner between bay and coastal ocean.

Bay exit angle, $\theta$: Even for high bay exit Rossby numbers, $\mathrm{Ro} > 13$ or even $\mathrm{Ro} > 33$, no recirculating bulge forms, if the bay exit angle is less than or equal to $60°$, $\theta \leq 60°$. I.e., $\theta > 60°$ and $\mathrm{Ro} > 1$ need to be fulfilled.

Of course there are intermediate stages between a distinct recirculating bulge and a coastal current only, called jet. E.g., the plume may detach from the coast, form a bulge and re-approach the coast under an impact angle (Fig. 2.3(b)) small enough, $\Phi < 60°$, so that no recirculation occurs. $\Phi$ depends on $f$, $u$, $r_c$ and $\theta$. For a detailed description see Avicola and Huq (2003b).
Furthermore it should be noted that the formation of a recirculating bulge has considerable influence on the coastal current: Since approximately $60\%$ of the source freshwater

flux is stored in the bulge, the currents width, length and velocities are remarkably reduced (Avicola and Huq, 2003a).

### 2.2.3 Kelvin Number

Another classification of buoyant outflows is a hierarchy according to the Kelvin number, $K$. This is the ratio of the across-shore length scale, i.e. the plume width, $W$, and the internal Rossby radius, $R_1$: $K = W/R_1$. The internal Rossby radius is $R_1 = c_1/f$, where $c_1 = \sqrt{g' H_\mathrm{p}}$ is the phase speed of the first baroclinic wave, $g' = g \cdot (\rho_\mathrm{a} - \rho_\mathrm{p})/\rho_\mathrm{a}$ the reduced gravitational acceleration with $\rho_\mathrm{p}$ the average density of the plume and $\rho_\mathrm{a}$ the density of the ambient coastal water, $H_\mathrm{p}$ the mean plume depth and $f$ the Coriolis parameter. The approximation $H_\mathrm{p} H_\mathrm{a}/(H_\mathrm{p} + H_\mathrm{a}) \approx H_\mathrm{p}$ for $H_\mathrm{p} \ll H_\mathrm{a}$ has been used. Garvine (1995) and Wiseman and Garvine (1995) distinguished between the following limiting cases:

Small-scale discharges, $K \ll 1$ (small $W$ or rather large $R_1$ (large $c_1$, small $f$)): Since the effects of planetary rotation are unimportant for such flows, the deflection of their plumes is dominated by ambient currents and not by the Coriolis force. Typical examples are discharges from narrow river mouths, engineering structures and near-equatorial sites.

Large-scale discharges, $K \gg 1$ (large $W$ or rather small $R_1$ (small $c_1$, large $f$)): Planetary rotation plays an important role and deflects the plume, so that a coastal current develops which cannot be reversed by ambient wind-driven flows in the opposite direction. A large recirculating bulge may form. Compared to its alongshore extent, the plume or rather the coastal current is thin cross-shore.

The features of intermediate cases, like $K \approx 1$ ($W \approx R$), lie in-between these limiting cases.

### 2.2.4 Bottom- and Surface-Advected Plumes

The differentiation into bottom- and surface-advected plumes was formulated by Yankovsky and Chapman (1997). Dependent on inflow properties, bathymetry and ambient flows, the plume structure may vary (Fig. 2.4).

Bottom-advected plumes: Large discharges with rather low density differences from the ambient sea form plumes occupying the water column from surface to bottom. Density gradients are strongest in horizontal directions, whereas there is only low stratification in the vertical. Due to the bottom contact, the plume's behaviour is controlled by advection in the bottom boundary layer. Typical scales are an offshore extent of $100\ \mathrm{km}$ and an attained depth of $200\ \mathrm{m}$.

Surface-advected plumes: No matter how high the inflow velocities may be, for density differences above a critical value, the buoyant input lays itself on top of the ambient water and forms a thin plume at the surface. A pronounced vertical stratification

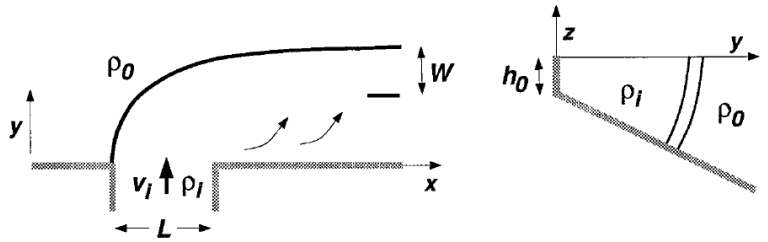


(a) Schematic of a bottom-advected plume

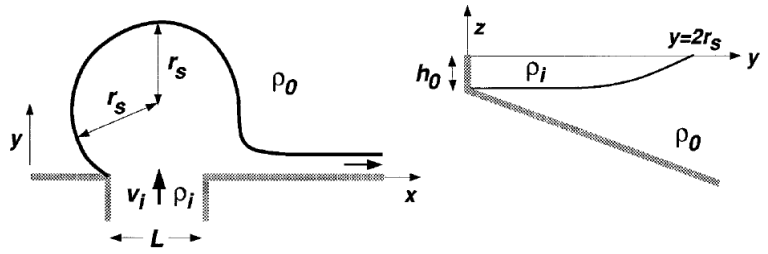


(b) Schematic of a surface-advected plume

**Figure 2.4:** Bottom- and surface-advected plumes. Left panels: top view, right panels: side view. (Yankovsky and Chapman, 1997, Fig. 1, 2)

develops. Such a plume is more susceptible to external influences like wind and the Coriolis force. Its typical thickness is $10\ \mathrm{m}$, offshore extents lie between $10$ and $15\ \mathrm{km}$.

Intermediate plumes are composed of both these types: Near the shore the plume is connected with the bottom, but at a certain distance it detaches and grows thin. The density fronts gradually incline from vertical to nearly horizontal with increasing height.

### 2.2.5 Pulsed River Discharge and Plume

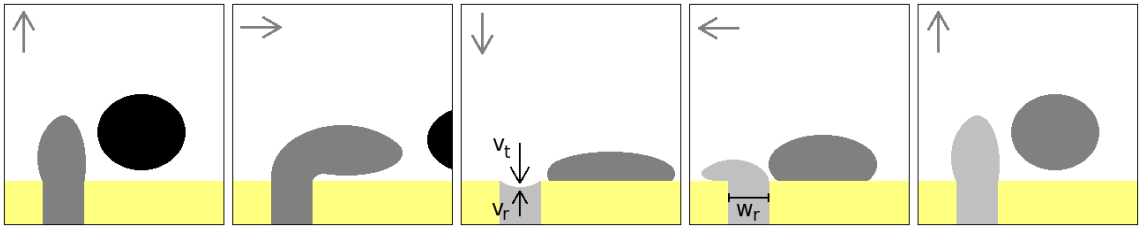


**Figure 2.5:** Schematic of a pulsed river discharge and plume. The arrows indicate the direction of the surface tidal current, which rotates clockwise in this example. Three different shades of grey identify the successive pulses. (See text for definition of $v_\mathrm{t}$, $v_\mathrm{r}$ and $w_\mathrm{r}$. $r_i$ cannot sensibly be drawn into a tidal figure; $r_i = r_s$ in Fig. 2.4(b).)

For tidal estuaries, another feature of plume structure is patchiness, i.e. that the river water does not flow out continuously, but in discrete pulses, which form separate lenses

of fresher water in the coastal zone (Fig. 2.5). In order to make this possible, two basic criteria have to be fulfilled (de Ruijter et al., 1997; Fig. 2.6):

Pinching-off criterion: The freshwater discharge is withheld by opposing tidal currents once every tidal period, i.e. the plume is disrupted. Therefor, the tidal current velocity component, $v_\mathrm{t}$, in the upstream direction of the river has to be greater than the outflow velocity, $v_\mathrm{r}$, of the riverine water, i.e. $v_\mathrm{r}/v_\mathrm{t} < 1$.

Separation criterion: In order to prevent interference of successive discharge pulses, a pulse has to move far enough from the river mouth within one tidal period. Assuming the existence of an inertial turning region at the estuary, this means that the inertial radius, $r_\mathrm{i} = v_\mathrm{r}/f$, has to be greater than the river mouth width, $w_\mathrm{r}$, i.e. $v_\mathrm{r}/(f w_\mathrm{r}) > 1$. (This is a simplified view not considering the interaction with ambient sea water.)

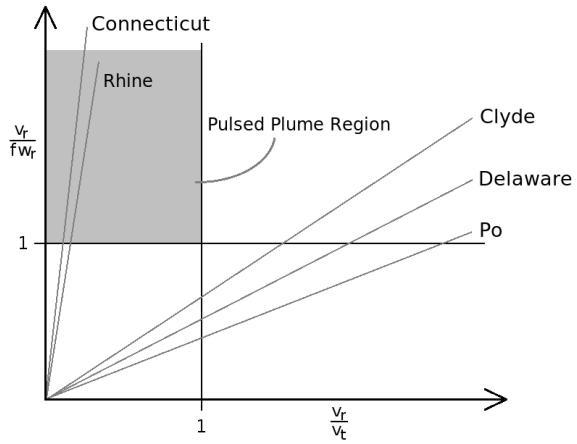


**Figure 2.6:** For a pulsed river discharge and plume, two criteria have to be satisfied (adapted from de Ruijter et al., 1997, Fig. 7). The Rhine achieves this for average and higher discharges. See text for description and section 2.4 for calculation.

The velocity $v_\mathrm{r}$ refers to the out-flowing freshwater in the upper part of the water column and is greater than the net discharge velocity.
In case a river fulfils both these criteria for a certain range of $v_\mathrm{r}$ and when the actual discharge coincides with this range (shaded area in Fig. 2.6), the outflow is separated into pulses and the near-field plume (see sec. 2.3) consists of individual patches of fresher water. The life time of these patches depends strongly on tidal and wind mixing and generally spans a few days to weeks (de Ruijter et al., 1997).

## 2.3 Differentiation between Near and Far Field

The near field is that part of a region of freshwater influence in which the buoyant outflow is supercritical, i.e. where the internal Froude number is greater than or equal to one, $Fr = v_\mathrm{r}/c_1 \geq 1$. $v_\mathrm{r}$ is the outflow velocity as given above and $c_1$ is the phase

speed of the first baroclinic wave (cp. sec. 2.2.3). The dynamics in the near field are controlled by advection and shear mixing whereas in the far field, the Earth's rotation, tides and wind play the major role (Hetland, 2008).

## 2.4 Rhine River Plume and Region of Freshwater Influence

As described in section 1.2, the Rhine and the Meuse water reach the North Sea mainly through the New Waterway and the *Haringvliet* strait. (To simplify matters, I will henceforth speak of the Rhine only.) When entering the open sea, the freshwater forms a buoyant plume and is deflected to the right, i.e. northeastward, under influence of the Coriolis force and ambient wind-induced currents. Further deflection of the flow is inhibited by the coast, where the Coriolis force is balanced by the pressure gradient force exerted by the water mounted up against the land (Kelvin wave, see sec. 2.5.4).
According to the given classifications of river plumes (sec. 2.2), the Rhine plume can be specified as follows (also cp. sec. 6.1):

Open coast: The river discharge enters the North Sea at a straight coast line. Only the artificial island of the *Maasvlakte* ("Meuse Plain") industrial area southwest and a breakwater northeast of the New Waterway confine the potential plume area, in addition to the coast itself.

Recirculating bulge: The angle between the New Waterway and the coastline is perpendicular. Due to the breakwater, there is no curved transition from the canal to the shore, but a sharp edge. Under these conditions, the development of a recirculating bulge is expected.

Kelvin number greater than one: The Rhine presents a large-scale discharge. The internal Rossby radius is $R_1 = 6.7\ \mathrm{km}$, for which the following properties have been applied: $\rho_\mathrm{p} = 1,005\ \mathrm{kg/m^3}$, $\rho_\mathrm{a} = 1,020\ \mathrm{kg/m^3}$, $H_\mathrm{p} = 5\ \mathrm{m}$, $H_\mathrm{a} = 15\ \mathrm{m}$ (van Alphen et al., 1988, characteristic values), $g = 9.81\ \mathrm{m/s^2}$ and $f = 1.1 \cdot 10^{-4}/\mathrm{s}$. Assuming a plume width $W = 20\ \mathrm{km}$ (de Ruijter et al., 1997), the Kelvin number results in $K = 2.99 > 1$, what is in very good agreement with the literature (e.g. $K = 3.0$ in Garvine, 1995, Tab. 1). That is to say, the Earth's rotation acts on the buoyant outflow, which, however, may also be controlled by wind.

Intermediate case between bottom- and surface-advected plume: The discharge of the Rhine is high (approx. $2,200\ \mathrm{m^3/s}$ on average), but so is the density difference between the North Sea (salinity of approx. $32\ \mathrm{g/kg}$) and the river's freshwater. As visible in Fig. 2.7(a), isohalines are vertical in the lower half of the water column. Above, they bend offshore or rather form a smooth basin around the surface water of lowest salinity. In the centre of this, the isohalines lie horizontally. The plume is influenced to some degree by external forces, i.e. the Coriolis force and wind.

Pulsed discharge and plume: In the mouth region of the Rhine, near surface tidal currents reach $1\ \mathrm{m/s}$ with variations of about $30\%$ occurring during the spring-neap cycle (de Ruijter et al., 1997); the Coriolis parameter, $f = 1.1 \cdot 10^{-4}/\mathrm{s}$, and the river mouth width, $w_\mathrm{r} = 500\ \mathrm{m}$ (New Waterway), give $f w_\mathrm{r} = 5.5 \cdot 10^{-2}\ \mathrm{m/s}$. Thus, the outflow velocity needs to fulfil $0.055\ \mathrm{m/s} < v_\mathrm{r} < 1\ \mathrm{m/s}$, which is true most of the time. E.g., for a close-to-average discharge of $2,600\ \mathrm{m^3/s}$ (at Lobith), $v_\mathrm{r} = 0.6\ \mathrm{m/s}$ is suggested (van Alphen et al., 1988; de Ruijter et al., 1997). Consequently, the Rhine exhibits a distinctly pulsed discharge, but due to strong mixing in the estuarine shelf sea, the life time of the freshwater pulses does not exceed $1$ week (average discharges, light winds). For winds of Beaufort $\geq 5$, this may decrease to $2$ days and less, whereas in periods of high discharge and relatively strong coast-parallel southwesterlies (predominant in December and January, cp. Fig.s 1.5 and 2.8) the pronounced Dutch coastal current can carry a train of freshwater lenses over distances longer than $80\ \mathrm{km}$ (de Ruijter et al., 1997).

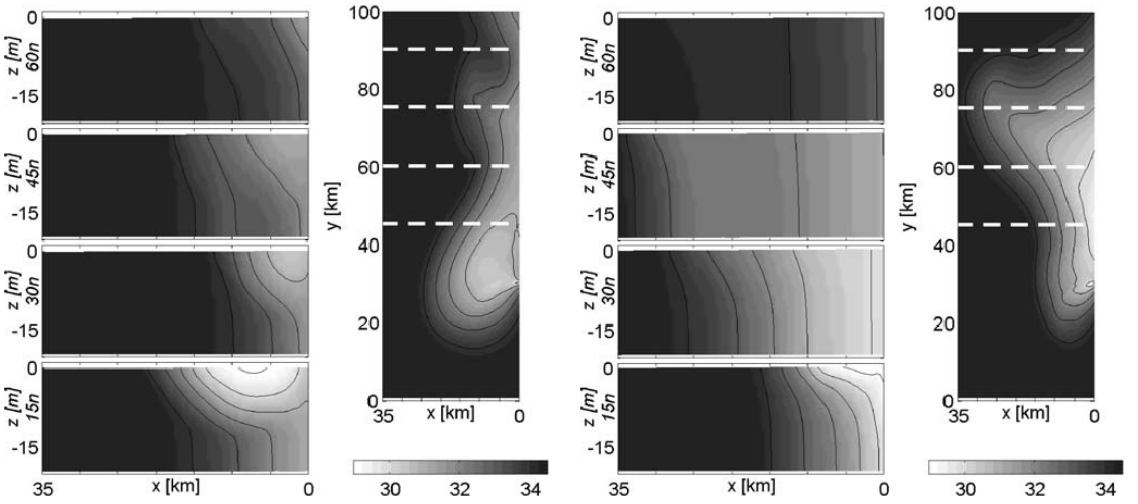


(a) Neap tide: Stratification is stable close to the river mouth and decreasing with distance from the freshwater source.

(b) Spring tide: Tidal stirring is much more intense; except in the near field, the water columns are well mixed.

**Figure 2.7:** Time-averaged Rhine plume salinity (psu) at neap and spring tide as derived from numerical simulations. Left panel: cross-shore cross-sections at $15$, $30$, $45$ and $60\ \mathrm{km}$ northeast of the river mouth; right panel: depth-averaged top view with dashed lines at the locations of the cross-sections. (de Boer et al., 2006, Fig. 4, 5)

With a plume structure as described above, the Rhine ROFI lies parallel to the Dutch coast and is approximately $30\ \mathrm{km}$ wide and $100\ \mathrm{km}$ long (Souza and Simpson, 1997). Like all other ROFIs, it is affected by several different processes, some of which are universal, e.g. tides and wind, and some of which are typical for coasts with estuaries only, e.g. the inflow of freshwater. While the tides occur periodically (also see sec. 2.5.3), river discharge and wind (Fig.s 1.5, 2.8) follow a seasonal cycle with unpredictable changes

at short time scales. The Rhine runoff mostly ranges between $1,000$ and $2,500\ \mathrm{m^3/s}$, though extreme values of $600\ \mathrm{m^3/s}$ minimum and $13,000\ \mathrm{m^3/s}$ maximum can occur (de Ruijter et al., 1992) (cp. sec. 1.3). The interplay of tides, wind and discharge is responsible for a variety of possible plume forms (see, e.g. Hessner et al., 2001, radar images) with different extents of stratification (Fig. 2.10).

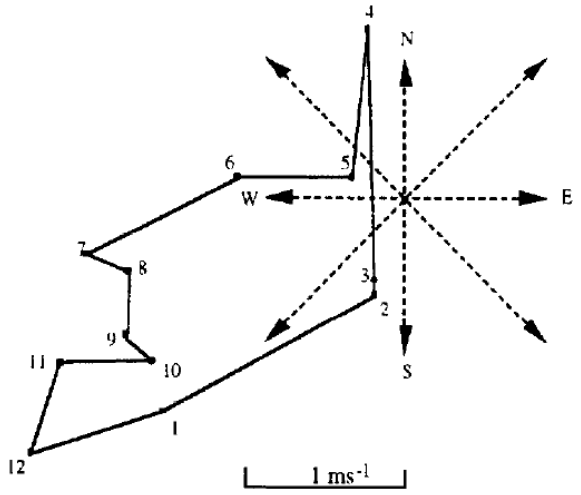


**Figure 2.8:** Mean annual cycle (averaged over 1953-1981) of the monthly mean wind direction (i.e. origin) and speed ($\mathrm{m/s}$) as derived from measurements at the light vessel *Noord-Hinder* ($51.6°\mathrm{N}, 2.5°\mathrm{E}$) in the Rhine ROFI (Visser et al., 1991, Fig. 2a). The numbers indicate the months of the year. Wind speed is maximum from mid summer to mid winter when winds come from southwest; only from April to June, the average wind direction is northwest.

## 2.5 Relevant Physical Processes in a ROFI

As already indicated, a ROFI represents the interactive zone between the open sea and an estuary and is thus a complex system characterised by many variables and processes. In this section, the most important physical processes of ROFIs in general and of the Rhine ROFI in particular are explained.

### 2.5.1 Stratification and Mixing

A water column is referred to as stably stratified if its density increases with depth. Conversely, if water of higher density overlies water of lower density, the water column is regarded as unstably stratified. For these two situations, the occurrence of horizontal layers with distinct properties is typical. Another case is a mixed water column, in which the density profile is homogeneous from surface to bottom.
In the development of stratification, different processes can play a role:

Temperature-induced stratification: If the surface water is heated (but not evaporated, see below), e.g. by solar radiation, its density decreases (above the maximum

density temperature); the water column becomes stably stratified. On the contrary, if the surface temperature is lowered, e.g. by cooling winds, the surface density increases; the water column becomes unstably stratified.

Salinity-induced stratification: In saline water bodies, an input of freshwater means an input of buoyancy. If this water of less density is added at the surface, as is the case for the principal freshwater sources rivers, precipitation and melting ice floes, stable stratification occurs. If, by contrast, freshwater is removed from the surface, e.g. by evaporation or freezing, water of higher salinity and density remains, which implies a de-stabilisation.

Straining, deformation: Stratification can also be provoked by a deformation of the water body. Where horizontal density gradients exist, as for two differently dense water columns next to each other, a vertical shear of the horizontal velocity can force less dense over denser water and so induce stable stratification (see Fig.s 2.9(a), (b)) or it can force denser over less dense water and so induce unstable stratification (also see sec. 2.5.6). Additionally, the horizontal density gradient itself induces a circulation stratifying the water column (Fig. 2.1 in sec. 2.1).

Advection, displacement: If, at a certain location, a water column is replaced by another, the stratification situation at this location may change, even though the displaced water column itself remains the same (see Fig. 2.9(c)).

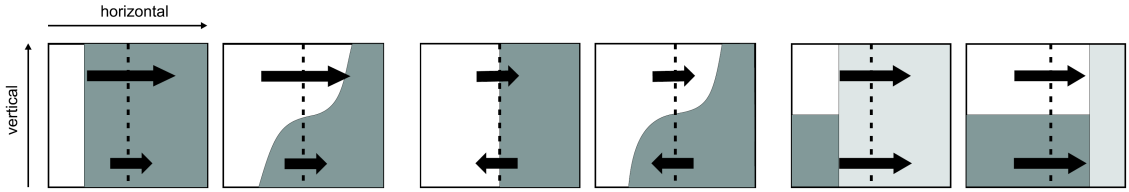


(a) Shear and straining (b) Shear and straining (c) Horizontal advection

**Figure 2.9:** Schematic of straining and advection in a water body with horizontal and vertical density gradients. Dark shading represents high density and light shading represents low density; left panels precede right panels (Hofmeister, 2006, Fig. 1).

As the name implies, stable stratification does not break down of its own accord. An unstably stratified water column, on the other hand, mixes by convective motions in the vertical direction. This convection is driven by gravitation, which is stronger for the relatively heavier water at the surface than for the lighter water at the bottom. (In other words, the buoyancy force is stronger for the lighter water.) Consequently the surface water moves downwards and the bottom water moves upwards, an exchange flow which goes along with mixing. The available potential energy is transformed into kinetic energy or rather turbulent kinetic energy, which, in turn, is dissipated into heat (see sec. 2.5.7). All water bodies are subjected to the mixing effects of tides, wind, waves, diffusion and combined processes like dispersion. Tides, wind and, to some degree, waves induce currents, which can transport remarkable amounts of water over long distances and

consequently add to the large-scale spreading and mixing. A small-scale mixing effect is due to viscosity, i.e. internal friction, and drag, which cause turbulent eddies inside the stream and at its boundaries to adjacent water, the bottom or rather the atmosphere. For waves, an additional contribution can be made if they break. Eddies literally stir the water and thus mix up its properties, e.g. temperature or any solute's concentration. Wind has the same effect, but mostly only affects the surface layer. Another mixing component is molecular diffusion, the random motion of micro-scale particles like molecules, which brings about a macro-scale mass transfer. Since statistically the flux of a certain property, e.g. salinity, is directed from regions of higher to regions of lower concentration, the result is a smoothing of gradients and thereby a homogenisation of the water body. An example of a combined process is shear flow dispersion, which implies the diffusion of particles transported in an inhomogeneous velocity field.
In a ROFI, all these processes interact, though some of them are more significant than others. In contrast to the open ocean and those parts of the continental shelf sea which are not adjacent to river mouths, stratification in a ROFI is controlled by salinity rather than by temperature. Instead of surface heating, freshwater input and tidal straining of the plume are the principal stratifying processes opposing mixing.
The Rhine discharges a great amount of freshwater into or rather onto the southern North Sea so that a strong stable stratification occurs. The river water floats as a buoyant plume above the denser sea water and is deflected to its right-hand side, i.e. northeastward, by the Coriolis force and ambient wind-induced currents; the wind- and buoyancy-driven Dutch coastal current develops. At the plume fronts, diffusion and shear-induced eddies smooth the salinity and density gradients; the plume becomes wider and less defined with growing distance from the source. Additionally, wind and waves may stir the upper part of the water column; a vertically homogeneous layer of less dense water remains on top of the unaffected bottom layer. On account of the shallow depth of $20\ \mathrm{m}$, strong winds may homogenise the water from surface to bottom. Tides can have both a stratifying and a mixing effect: Each one is associated with tidal straining (see sec. 2.5.6), but the latter is significantly enhanced by turbulence, which increases with rising tidal amplitude and current speed. I.e., the impact of tidal stirring follows the fortnightly spring-neap cycle and is maximum at spring tides. For winds less than $\mathrm{Bf.}\ 2$, tides represent the dominating mixing process, whereas for winds stronger than $\mathrm{Bf.}\ 3$, wind stirring dominates (van Alphen et al., 1988). Fig. 2.10 shows the average, minimum and maximum extent of the stratified area of the Rhine ROFI.

### 2.5.2 Residual Current

The poorly defined term of a residual current mostly refers to the average water movement of a tidal cycle, i.e. the non-oscillatory part of the flow. It comprises density- and wind-driven components as well as, if applicable, a component resulting from non-linear interactions of tides and local topography (Fischer et al., 1979, p. 237).
In the southern North Sea, predominant west and southwest winds give rise to a northeastward coastal current. The freshwater input from the Rhine and other rivers provides a significant density-driven component (Bowden, 1983, p. 206), which, due to the Cori-

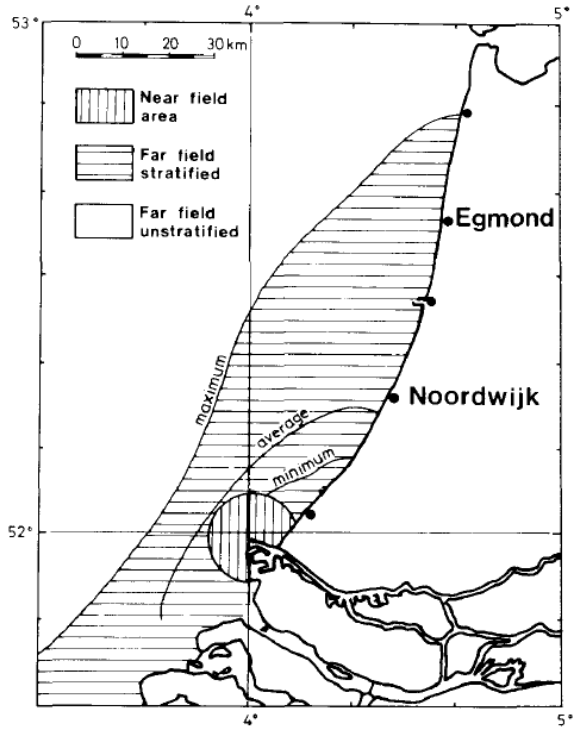


**Figure 2.10:** Stratified area of the Rhine ROFI under average and extreme discharge and wind conditions, based on measured data from 1985 (van der Giessen et al., 1990, Fig. 5).

olis force, contributes to the same direction (also see sec. 1.4). Since wind acts on the surface, due to bottom friction and because of the sense of rotation of the density-driven circulation, the velocity of the residual current increases with height above the bed. Inside the ROFI, the depth-averaged residual varies between $3$ and $8\ \mathrm{cm/s}$ (van Alphen et al., 1988) and the surface residual varies between $15$ and $20\ \mathrm{cm/s}$ (Simpson et al., 1993), all pointing northeastward. Outside the ROFI, where there are no remarkable horizontal density gradients, the flow is much weaker and more susceptible to changes in wind strength and direction.

### 2.5.3 Tides, Tidal Constituents and Amphidromic Points

Tides play an important role for the processes related to water levels, currents, mixing and stratification. In order to investigate these processes in a temporal context, diverse tidal constituents need to be considered with respect to their period and amplitude.
It is assumed that the formation of tides is known, i.e. that the interaction of the gravitational forces of the Earth, the Moon and the Sun on the water body is understood. The tidal potential at a certain location and time is determined by a number of parameters, e.g. angles and distances, which have different significance and periodicity. It can be resolved into a sum of harmonic constituents, the more important of which are specified in Tab. 2.1.
To what extent a tidal constituent occurs in the actual tides at a certain location depends

| symbol | period | constituent | cause |
|---|---|---|---|
| | hours | semi-diurnal | |
| $M_2$ | 12.42 | principal lunar | rotation of Earth relative to Moon |
| $S_2$ | 12.00 | principal solar | rotation of Earth relative to Sun |
| $N_2$ | 12.66 | larger lunar elliptic | ellipticity of Moon's orbit |
| $K_2$ | 11.97 | luni-solar | declination of Moon and Sun |
| | hours | diurnal | |
| $K_1$ | 23.93 | luni-solar | declination of Moon and Sun |
| $O_1$ | 26.87 | principal lunar | declination of Moon |
| $P_1$ | 24.07 | principal solar | declination of Sun |
| | days | long period | |
| Mf | 13.66 | lunar fortnightly | declination of Moon |
| Mm | 27.55 | lunar monthly | ellipticity of Moon's orbit |
| Ssa | 182.70 | solar semi-annual | declination of Sun |

**Table 2.1:** Important harmonic constituents (adapted from Bowden, 1983, Tab. 2.1). The luni-solar synodic fortnightly constituent, Msf (not listed), which is responsible for the spring-neap cycle, has a periodic time of approx. 14.76 days, what is referred to as a fortnight or half a synodic month. The causing parameter is the angle between the Moon, the Earth and the Sun: If they are aligned (syzygy), the gravitational forces of the Moon and the Sun add, bringing about spring tide; if they form an angle of $90°$, the forces partly cancel each other, resulting in neap tide.

on the geographical position and circumstances. Since the continents and the limited depth of the oceans inhibit a free movement of tidal water bulges around the rotating globe, the tides develop complex patterns inside the ocean basins. Along the coastlines, three basic types result; they and their global distribution are shown in Fig. 2.11.
For each constituent, the tide waves move around so-called amphidromic points or amphidromes (Greek *amphi* = "on both sides", "around"; *dromos* = "course", "way"), and that counterclockwise on the northern and clockwise on the southern hemisphere due to the Coriolis force. The tidal amplitude increases with distance from the amphidromic point, at which there is almost no vertical water movement.
Small and shallow water bodies are not directly affected by the tidal potential, but by the tide waves in adjacent oceans. Due to the Coriolis force, the semi-diurnal North Atlantic tide wave turns around Scotland into the North Sea, where it flows southward along the east coast of Great Britain. In the Southern Bight, it meets another tide wave, which has entered through the English Channel and the Strait of Dover and which has a higher tidal range, but transports much less mass. They form an amphidromic point and proceed northeastward along the Dutch, German and Danish coastline (see Fig. 2.12).
In the southern North Sea, the $M_2$ tide dominates, but $S_2$ and $N_2$ make significant contributions (Visser et al., 1994). The tidal range near the New Waterway outlet spans $1.5$ m at neap and $1.9$ m at spring tide; maximum surface currents are $0.8$ or $1.1$ m/s northeastward during flood and $0.7$ or $0.9$ m/s southwestward during ebb, respectively at neap or spring (van Alphen et al., 1988). For a description of tidal current types, see

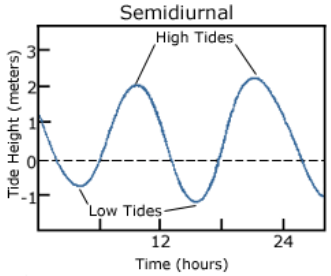


(a) Two high and two low tides of approximately the same height per lunar day.

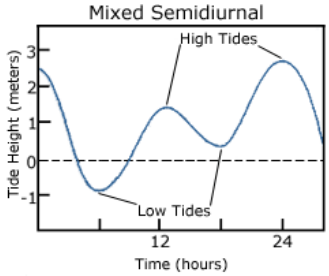


(b) Two high and two low tides of different height per lunar day (diurnal inequality).

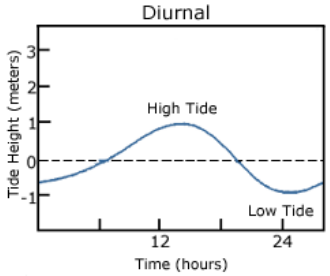


(c) One high and one low tide per lunar day.

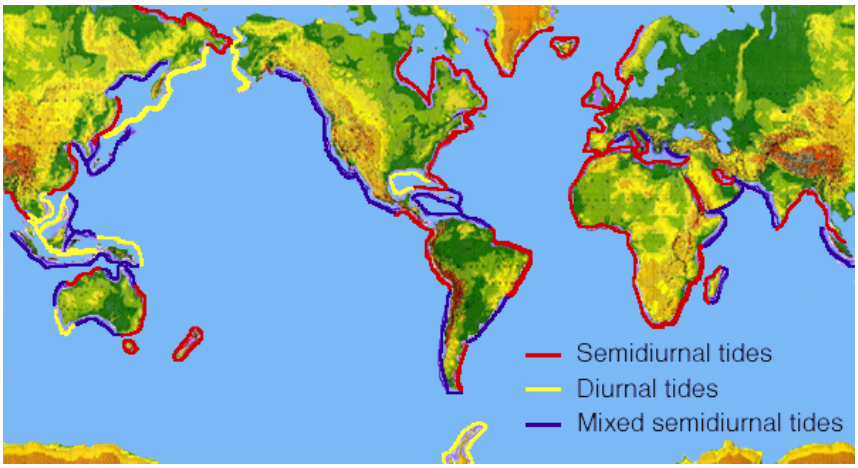


(d) Global distribution of the tidal patterns.

**Figure 2.11:** The three basic tidal patterns semi-diurnal, mixed semi-diurnal and diurnal as well as their distribution (`http://oceanservice.noaa.gov/education/kits/tides/tides07_cycles.html`).

section 2.5.5.

## 2.5.4 Kelvin Wave and Tidal Range

Like all moving objects seen from a rotating frame of reference, waves in the ocean or atmosphere are affected by the Coriolis force, i.e. on the northern hemisphere (southern hemisphere) they are deflected to their right-hand side (left-hand side) in the sense of wave propagation. (To simplify matters, I will henceforth consider the northern hemisphere only.) If an ocean wave travels with a topographic boundary to its right-hand side, e.g. a coast, it cannot be further deflected, but it will "lean" against the boundary. The emerging water bulge gives rise to a pressure gradient force opposing and balancing the Coriolis force. Such a wave is called Kelvin wave or, more precisely, coastal Kelvin wave (Fig. 2.13(a)). Its amplitude is maximum at the coast and exponentially declines with distance from the coast. There are also equatorial Kelvin waves (Fig. 2.13(b)), for which the equator represents the boundary and which can only travel from west to east.

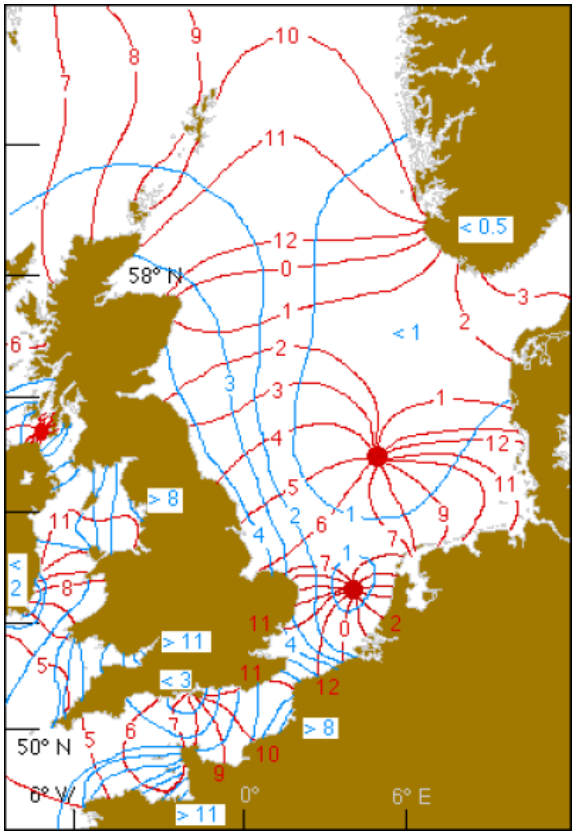


**Figure 2.12:** Tides in the North Sea as derived from observations. Red: amphidromic points and co-tidal, i.e. co-phase lines of the $M_2$ tide; numbers are hours after the Moon's transit through the meridian of Greenwich. Blue: co-range lines of the sum of $M_2$ and $S_2$; numbers are mean tidal range at spring tide. (`http://www.es.flinders.edu.au/~mattom/IntroOc/lecture11.html`, Fig. 11.5)

The opposing Coriolis forces of the northern and the southern hemisphere prevent the water bulge from diverging.
In an ocean basin, the tide wave moving around an amphidromic point can be regarded as a progressive Kelvin wave. The tidal range is maximum at the coasts, where the tidal elevation periodically alternates with time according to the dominating tidal constituents (see sec. 2.5.3). Along straight coastlines where co-tidal lines are equidistant, like along the east coast of Northern England and the Dutch coast (cp. Fig. 2.12), the elevation likewise periodically alternates in space and that in the coast-parallel direction. Equations (2.1) and (2.2) apply to the sea surface elevation $\eta(x, y, t)$ and the alongshore velocity $v(x, y, t)$ of the Kelvin wave (for derivations, see app. A.1):

$$\eta = a \exp\left(f\frac{x}{c}\right) \cos(ky - \omega t) \tag{2.1}$$

$$v = a\sqrt{\frac{g}{H}} \exp\left(f\frac{x}{c}\right) \cos(ky - \omega t) \tag{2.2}$$

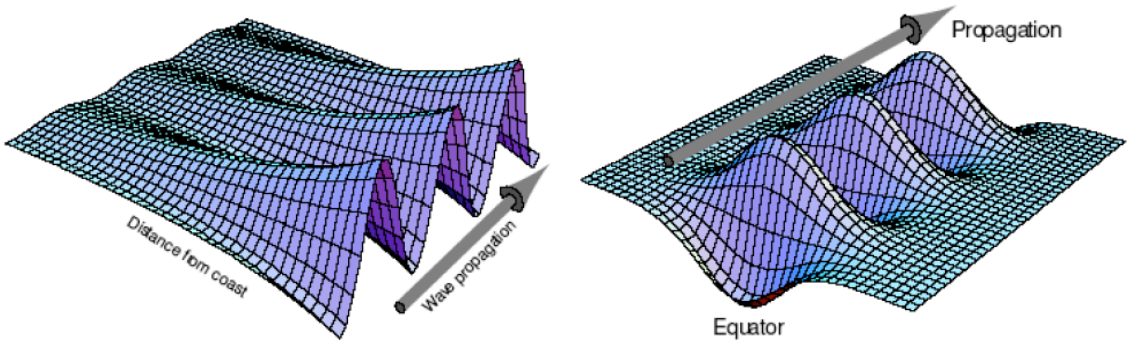


(a) Coastal Kelvin wave (b) Equatorial Kelvin wave

**Figure 2.13:** Schematics of Kelvin waves (`http://www.gps.caltech.edu/~claudia/ese148b/pdfs/lec16.pdf`). See text for description.

with $a$ the amplitude at the coast, $f$ the Coriolis frequency, $c = \sqrt{gH}$ the wave speed ($g$ gravitational acceleration, $H$ water depth), $k = \omega/c$ the wave number and $\omega = 2\pi/T$ the angular frequency ($T$ periodic time). $x$ is the distance from the coast (negative, $0$ at coast), $y$ the alongshore dimension and $t$ the time.
The Coriolis force has a great influence on tidal ranges: On the right-hand side of a tidal wave, i.e. at the coast the Kelvin wave leans against, the tidal range is much higher than on the other side. This explains the difference in the English Channel between $3$ to $5$ m at the English and up to $11$ m at the French coast, by way of example.

### 2.5.5 Tidal Currents and Ellipses

A tidal current is referred to as the horizontal water movement associated with the tides, i.e. with the vertical rise and fall of the sea surface. It is commonly called flood between low and high water and ebb between high and low water. (About the ambiguity in case of rotary currents, see the caption of Tab. 2.2.) Slack water, also called slack only, is the moment when the depth-mean current speed is near zero.
In narrow, partially enclosed water bodies, in which rotational effects can be neglected, like in narrow bays, estuaries and rivers, the tidal wave resembles a standing wave. The tidal current basically flows back and forth along the principal axis; it is called reversing or rectilinear. The flood current moves onshore or up an estuary or tidal river until high water is reached; then the ebb current moves offshore or downstream until low water. Slack waters coincide with both low and high water, when the current direction reverses. Maximum current speeds occur midway between low and high water (maximum flood) as well as midway between high and low water (maximum ebb) (see Tab. 2.2 and Fig. 2.14).

Away from coastal limitations, the tidal current is rotary. Due to the Coriolis force and the interaction of tidal constituents, the current vector traces out an elliptical-shaped hodograph, the so-called tidal current ellipse. Its sense of rotation is not obvious, but depends on a number of factors. Observations vary from a pure clockwise to a pure counter-clockwise rotation and also comprise examples where the direction turns from clockwise

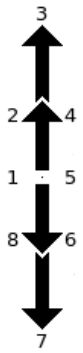


| reversing current (standing wave) | stage | | rotary current (progressive wave) |
|---|---|---|---|
| slack before flood | 1 | LW | maximum ebb |
| increasing flood | 2 | ↑ | decreasing ebb |
| maximum flood | 3 | ↑ | minimum before flood |
| decreasing flood | 4 | ↑ | increasing flood |
| slack before ebb | 5 | HW | maximum flood |
| increasing ebb | 6 | ↓ | decreasing flood |
| maximum ebb | 7 | ↓ | minimum before ebb |
| decreasing ebb | 8 | ↓ | increasing ebb |
| slack before flood | 1 | LW | maximum ebb |

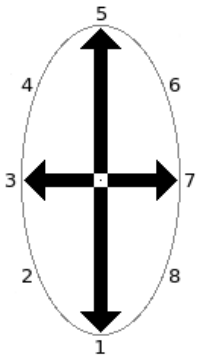


**Table 2.2:** Reversing and (near-degenerate) rotary tidal current.
The numbers in the middle column correspond to the numbers in the figures. Next to them, the sea level rise (↑) and fall (↓) are indicated; low water (LW) is at stage 1, high water (HW) is at stage 5. The rotary current represented here has a clockwise sense of rotation. For a near-degenerate ellipse, the minor axis has to be regarded as oversized (see text for occurrence and further description; also cp. Fig. 2.14).
The terms "flood" and "ebb" are not well defined for rotary currents: Although commonly applied to the horizontal water movement related to sea level rise (1 to 5) or rather fall (5 to 1), literature uses them for the two semi-major axes of the ellipse (3 to 7, 7 to 3), so that the flood and the ebb current are governed by opposing directions.

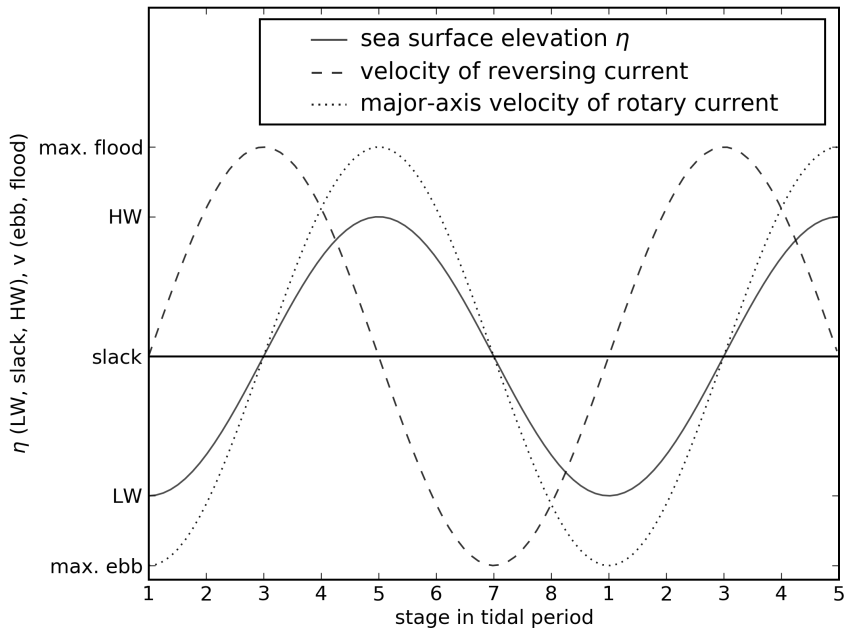


**Figure 2.14:** Graph depicting the phase relationship between the sea surface elevation, $\eta$, and the velocities, $v$, of a reversing current and of the major axis of a rotary current. The numbers along the abscissa correspond to the numbers in Tab. 2.2 (1 low water, 5 high water; i.e. representing the temporal course); the ordinate only serves as an orientation for both $\eta$ and $v$ and is not to any scale.

at the surface to counterclockwise at the bottom (northern hemisphere; Soulsby, 1990, p. 527). Correlations between the sense of rotation and features of the respective amphidromic system have been investigated: Prandle (1982) showed that in regions with equally spaced co-range lines, the rotation is cyclonic; Carbajal (2000) found anticyclonic rotation to occur there where the gradients of sea surface elevation and current phase tend to be parallel or close to zero.
Along straight coastlines, the tidal wave can be regarded as a progressive Kelvin wave (sec. 2.5.4). The depth-averaged tidal ellipse is near-degenerate, i.e. the depth-averaged current is nearly rectilinear, with the major axis parallel to the coast. Though apparently resembling the reversing current, it behaves different with respect to the phase relationship between surface elevation and current speed and direction: Slack water, i.e. minimum current speed, does not coincide with low and high water, but occurs midway between them, when the current direction turns at its highest rate. Maximum current speeds occur at both low and high water (see Tab. 2.2 and Fig. 2.14).
A useful parameter for the description of rotary tidal currents is the ellipticity, $\varepsilon$, which is defined as the ratio of the semi-minor axis, $B$, to the semi-major axis, $A$: $\varepsilon = B/A$. The two extremes are $\varepsilon = 0$ for a rectilinear current and $\varepsilon = \pm 1$ for a circular current. $A$ is defined positive; the sign of $B$ and $\varepsilon$ is determined by the sense of rotation: Positive means cyclonic (counterclockwise) and negative means anticyclonic (clockwise in the northern hemisphere) (cp. app. A.2).
In the North Sea, there are regions with clockwise as well as regions with counterclockwise rotating surface tidal currents; Fig. 2.15 shows a model result of their distribution. The southeast part of the Southern Bight is dominated by counterclockwise rotation.
Closer to the Dutch coast, the stratification becomes stronger and this has an influence on the ellipticity of the surface (see Fig. 2.16) and the bottom tidal current as it has been investigated by e.g. Visser et al. (1994) and Souza and Simpson (1996). Since a detailed description of the dynamics would go beyond the scope of this work, the relationships are briefly exemplified in Fig. 2.17. For fundamental understanding one has to know that a vector tracing out an ellipse can be regarded as the sum of two counter-rotating phasors; accordingly, the elliptical tidal current can be decomposed into a counterclockwise and a clockwise rotating component (see app. A.2). For these two, bottom friction is differently significant with respect to the penetration height of internal stresses, a length called the boundary layer thickness (Prandle, 1982). In the Rhine ROFI, this is $\delta_+ = 10\ \mathrm{m}$ for the counterclockwise and $\delta_- = 30\ \mathrm{m}$ for the clockwise component, i.e. the counterclockwise component reaches its free-stream value at mid-depth whereas the clockwise component is affected up to the surface (Souza and Simpson, 1996).
Please refer to appendix A.3 for a simple two-layer model yielding a clockwise surface ellipse and a counterclockwise bottom ellipse.

### 2.5.6 Tidal Straining

The interaction of tidal shear, i.e. a vertical gradient of the tidal current's horizontal velocity, with horizontal density gradients is called tidal straining. As already indicated in section 2.5.1, this process plays an important role in stratifying and mixing. If stratifica-

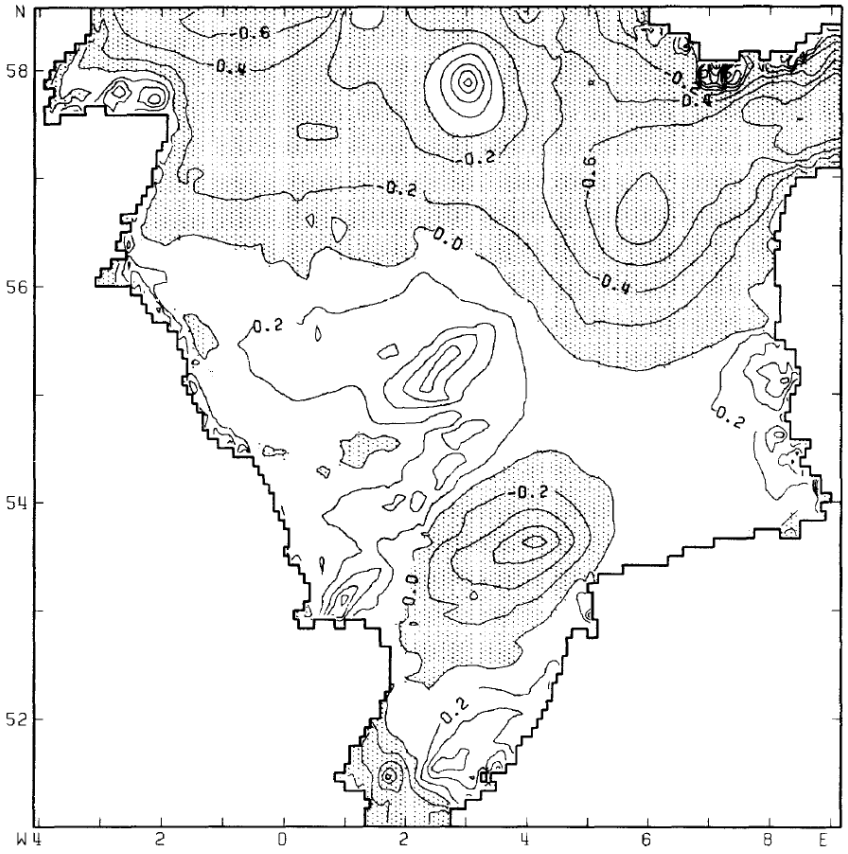


**Figure 2.15:** Tidal current ellipticity in the surface layer (upper $10\ \mathrm{m}$) in the North Sea as derived from a numerical model. Areas of clockwise rotation (negative ellipticity) are shaded (Xia et al., 1995, Fig. 6(d)).

tion principally increases and decreases due to tidal straining, it is called strain-induced periodic stratification (SIPS, Simpson et al. (1990)). In accordance with the differentiation of two types of tidal currents (Tab. 2.2, Fig. 2.14), two types of tidal straining can be distinguished with respect to the phase relationship between surface elevation and stratification.

In a tidal river or estuary, the reversing tidal current as well as the main horizontal density gradient are directed along the principal axis and thus lie parallel to each other. Consequently, the current profile has a direct impact on the inclination of the isopycnals, as shown in Fig. 2.18.

Close to a straight coastline, as in the Rhine ROFI, the depth-averaged tidal current is rectilinear (degenerate ellipse). For periods of low tidal (neap tides) and wind stirring, the surface tidal current is rotary in the clockwise direction and the bottom tidal current is rotary in the counterclockwise direction (cp. sec. 2.5.5, Fig. 2.17(b)). The major axes of the surface and of the bottom current ellipse lie coast-parallel: Both surface and bottom currents point northeastward at high water and southwestward at low water. In-between, the cross-shore velocity components oppose each other due to the contrary sense of rotation. This tidal shear interacts with the horizontal density gradient, which

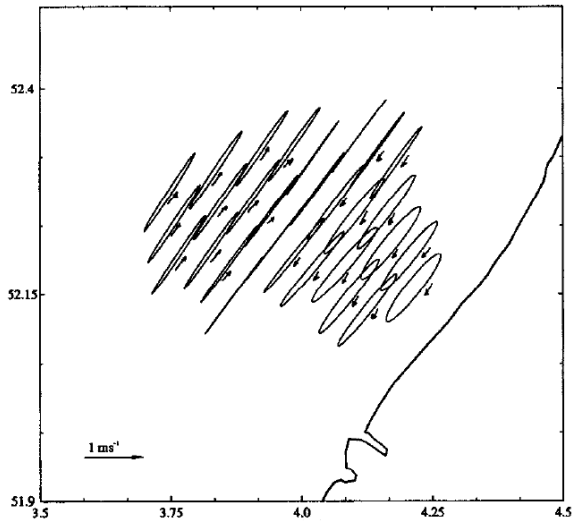


**Figure 2.16:** Mean $M_2$ tidal current ellipses at the surface in the Rhine ROFI acquired from radar observations (7 to 18 October 1990) (Souza et al., 1997, Fig. 2(a)).
The ellipticity changes from $-0.3$ (clockwise) near the coast to $0.08$ (weakly counterclockwise) in the distance; it is zero (degenerate ellipses) at about $20\ \mathrm{km}$ from the coast. The semi-major axis is about constant with approximately $0.8\ \mathrm{m/s}$ and lies coast-parallel.

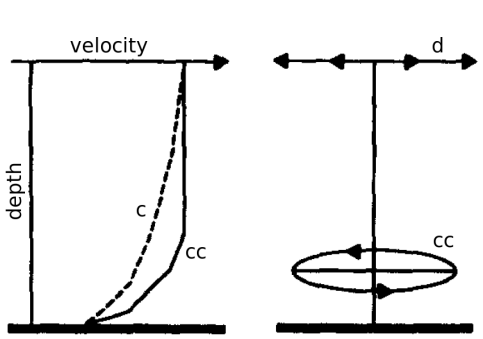


(a) Homogeneous water column. By way of illustration, a homogeneous water column with a degenerate surface ellipse is assumed, i.e. the surface current is rectilinear. Near the bottom, the clockwise component is reduced more than the counterclockwise component, so that the near-bottom ellipse exhibits counterclockwise rotation.

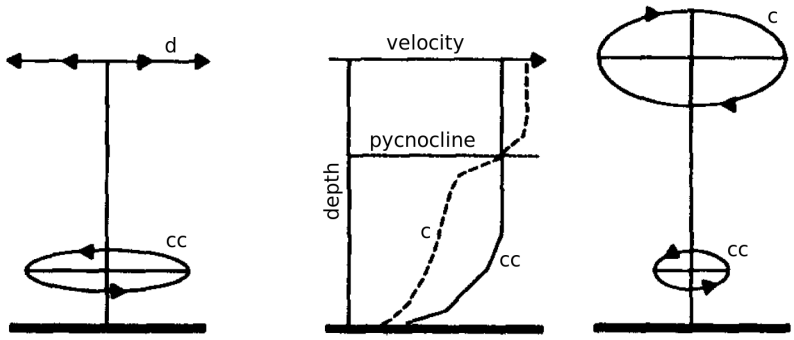


(b) Stratified water column. The decoupling into two layers restrains the transfer of momentum so that the clockwise component reaches its free-stream value in the upper layer whereas its reduction by friction intensifies in the lower layer. Current ellipses are clockwise at the surface and counterclockwise near the bottom.

**Figure 2.17:** Dependency of the ellipticity of a rotary current on depth and stratification (adapted from Souza and Simpson, 1996, Fig. 6).
The tidal forcing is the same for both situations. There is no significant effect on the counterclockwise component because this one acquires its free-stream value already below the pycnocline. Abbreviations: d degenerate, c clockwise, cc counterclockwise.

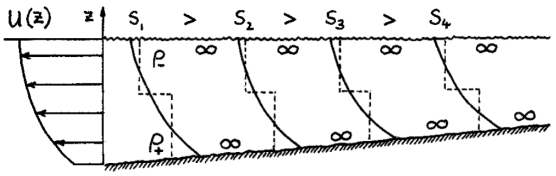


(a) Downstream current profile during ebb and stratified water columns at low water. The tidal shear of the ebb current inclines the isohalines (solid lines); surface and bottom mixing ($\infty$) form a two-layer profile (broken lines).

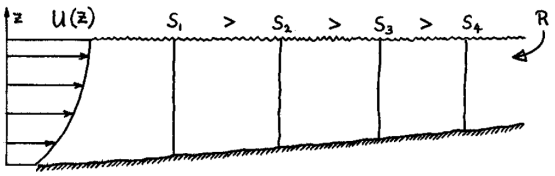


(b) Upstream current profile during flood and homogeneous water columns at high water. The tidal shear of the flood current re-straightens the isohalines; the water columns become well mixed. After high water, the cycle starts over.

**Figure 2.18:** Tidal straining in case of a reversing tidal current flowing back and forth parallel to the horizontal density gradients (adapted from Simpson et al., 1990, Fig. 2).
Salinity (S) decreases from left (open ocean) to right (river head, R). Stratification is established during ebb and diminished or even destroyed during flood, i.e. it is maximum at low water and minimum at high water.

is strongest in the cross-shore direction; stratification is induced or reduced as shown in Fig. 2.19. The result is a strain-induced periodic (semi-diurnal) cycle of stratification (SIPS) with maximum stable stratification occurring around high water.
For high tidal (spring tides) and wind stirring, the surface and bottom tidal current ellipses become more degenerate and the water column is well mixed over the entire tidal cycle.

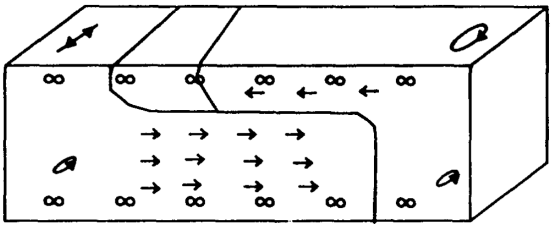


(a) Between low and high water, surface currents point offshore and near-bottom currents point onshore. The strong tidal shear inclines the isohalines, which are further modified by surface and bottom mixing ($\infty$) so that a two-layer profile is formed.

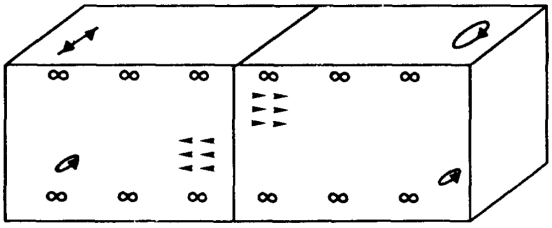


(b) Between high and low water, surface currents point onshore and near-bottom currents point offshore. The strong tidal shear re-straightens the isohalines so that the water column becomes well mixed. After low water, the cycle starts over.

**Figure 2.19:** Tidal straining in case of rotary surface and bottom tidal currents with the major axes perpendicular to the horizontal density gradients (Souza and James, 1996, Fig. 4).
Salinity decreases from left (open ocean) to right (coastline). Stratification is established between low and high water and diminished or even destroyed between high and low water, i.e. it is maximum at high and minimum at low water.

### 2.5.7 Turbulence and the Turbulent Kinetic Energy Budget

In a laminar flow (Latin *lamina* = "sheet", "slice") the fluid (water or air) smoothly moves in layers gliding past each other without eddies; the only mixing process is molecular

diffusion. A turbulent flow, on the contrary, is characterised by eddies, which significantly increase stirring and mixing. Since it is frequently seen in everyday life, everybody has an idea what turbulence is, but there is no exact definition. Nevertheless, turbulence can be identified by a number of properties describing turbulent flow (Lesieur, 1997; Burchard and Umlauf, 2007):

Randomness: A turbulent flow is unpredictable in the sense of a deterministic chaos.

Diffusivity: Turbulence significantly increases the interface between fluid volumes with different properties and thus it increases the mixing between them.

Vorticity: The fluid motion shows eddies with a wide size range.

Dissipation: Due to viscosity, turbulent kinetic energy is dissipated into heat (see below) at the small eddy sizes.

Non-linearity: Small perturbances propagate non-linearly and cause the flow to be statically unstable, i.e. to become more turbulent.

Reynolds (1895) introduced the decomposition (now called Reynolds decomposition) of a variable, $u$, into its mean, $\overline{u}$, and a fluctuating part, $\tilde{u}$ (e.g. Burchard and Umlauf, 2007):

$$\begin{aligned} u &= \overline{u} + \tilde{u} \\ \overline{u} &= \langle u \rangle = \frac{1}{T} \int_{t-T/2}^{t+T/2} u(\tau)\, \mathrm{d}\tau \\ \langle \tilde{u} \rangle &= 0 \end{aligned} \tag{2.3}$$

($\langle u \rangle$ denotes ensemble averages.) This is used to obtain the Reynolds-averaged continuity, momentum and Navier-Stokes equations, by way of example (Kundu and Cohen, 2002; Burchard and Umlauf, 2007). The turbulent kinetic energy ($\mathrm{TKE}$) can be written as

$$\mathrm{TKE} = \frac{1}{2} \left\langle \tilde{u}_i^2 \right\rangle = \frac{1}{2} \left\langle \tilde{u}^2 + \tilde{v}^2 + \tilde{w}^2 \right\rangle . \tag{2.4}$$

Potential ($E_{\mathrm{pot}}$), kinetic ($E_{\mathrm{kin}}$), turbulent kinetic ($\mathrm{TKE}$) and heat energy ($E_{\mathrm{heat}}$) are the four principal forms of energy in the ocean. The generation and destruction of turbulent kinetic energy comes along with various physical processes, as exemplified by

the following chart and the budget equation (2.5) of the TKE per unit mass:

$$\begin{array}{ccccc} & & E_{\mathrm{kin}} & & \\ & & \downarrow P & & \\ E_{\mathrm{pot}} & \overset{B_+}{\longrightarrow} \atop \underset{B_-}{\longleftarrow} & \mathrm{TKE} & \overset{\varepsilon}{\longrightarrow} E_{\mathrm{heat}} & \\ & & \uparrow\downarrow Tr & & \\ & & \mathrm{vicinity} & & \end{array} \qquad \frac{\mathrm{D(TKE)}}{\mathrm{D}t} = B + P - \varepsilon + Tr \tag{2.5}$$

Here,

$$\frac{\mathrm{D}}{\mathrm{D}t} = \frac{\partial}{\partial t} + \frac{\partial x_i}{\partial t}\frac{\partial}{\partial x_i} = \frac{\partial}{\partial t} + u_i\frac{\partial}{\partial x_i} \tag{2.6}$$

is the total derivative with respect to time. The Einstein summation convention has been used in equation (2.6). The four processes modifying the TKE are the following (Hofmeister, 2006; Kundu and Cohen, 2002):

$B$, buoyancy production (+) and consumption (−): In an unstably stratified water column, potential energy is stored and tends to be reduced by convective motions in favour of turbulent kinetic energy. Since the driving mechanism of this process is gravitation and buoyancy, it is called buoyancy production of TKE.
Contrariwise, if turbulence mixes a stably stratified water column, TKE is transformed into potential energy. This is called buoyancy consumption of TKE.

$$B = -\nu_t' N^2 \ , \ N^2 = -\frac{g}{\rho_0}\frac{\partial \rho}{\partial z} \tag{2.7}$$

with $\nu_t'$ the eddy diffusivity and $N^2$ the Brunt-Väisälä or buoyancy frequency squared, which is negative for unstable and positive for stable stratification.

$P$, shear production: In a shear flow with velocity gradients perpendicular to the flow direction, eddies form. Part of the kinetic energy of the flow is transformed into TKE, the energy of the eddies. Since shear is the cause of this, the process is called shear production of TKE. $P$ is almost always positive[1].

$$P = \nu_t S^2 \ , \ S^2 = \left(\frac{\partial u}{\partial z}\right)^2 + \left(\frac{\partial v}{\partial z}\right)^2 \tag{2.8}$$

with $\nu_t$ the eddy viscosity of momentum and $S^2$ the shear squared. For equation (2.8), the boundary layer approximation (horizontal homogeneity) as well as the traditional approximation ($w \ll u, v$) have been applied.

$\varepsilon$, dissipation rate: Due to viscosity, i.e. internal friction, the eddies loose TKE, which is dissipated into heat. However, the effect on temperature is mostly neglectable

[1] http://amsglossary.allenpress.com/glossary/search?id=shear-production1

in the ocean.

$$\varepsilon = 2\nu \left\langle (\tilde{e}_{ij})^2 \right\rangle \ , \ \tilde{e}_{ij} = \frac{1}{2}\left(\frac{\partial \tilde{u}_i}{\partial x_j} + \frac{\partial \tilde{u}_j}{\partial x_i}\right) \tag{2.9}$$

with $\nu$ the kinematic viscosity, $\tilde{e}_{ij}$ the fluctuating rates of strain and $\tilde{u}_i$ the velocity fluctuations (see eq. (2.3)).

$Tr$, transport terms: External forces and the turbulent eddies themselves transport $\mathrm{TKE}$ to and from the vicinity.

In turbulence equilibrium, i.e. for stationary turbulence ($\mathrm{D(TKE)}/\mathrm{D}t = 0$) and without energy fluxes ($Tr = 0$), equation (2.5) becomes (e.g. Burchard and Umlauf, 2007, sec. 5.4):

$$\varepsilon = B + P \tag{2.10}$$

The physical unit of the turbulent kinetic energy dissipation rate per unit mass is $[\varepsilon] = [\varepsilon_m] = 1\ \mathrm{W/kg} = 1\ \mathrm{m^2/s^3}$. Some scientists use the $\mathrm{TKE}$ dissipation rate per unit volume, which is $\varepsilon_V = \rho\ \varepsilon_m$ and which has the physical unit $[\varepsilon_V] = 1\ \mathrm{W/m^3} = 1\ \mathrm{kg/(ms^3)}$.
The ratio of the quantities $N^2$ and $S^2$ gives the gradient Richardson number, $Ri_\mathrm{g} = N^2/S^2$, which describes the dynamic stability of a stratified flow. The more stable the stratification is, the greater are $N^2$ and $Ri_\mathrm{g}$ and the more energy is needed for mixing; the more shear and thus turbulence exists in the flow, the greater is $S^2$, the smaller is $Ri_\mathrm{g}$ and the more energy is available for mixing. The critical Richardson number is taken to be $Ri_\mathrm{c} = 0.25$: If the actual $Ri_\mathrm{g}$ is greater than this everywhere in the flow, then the flow is linearly stable (Kundu and Cohen, 2002).

# Chapter 3

# Measured and Modelled $\mathrm{TKE}$ Dissipation Rate in the Rhine ROFI

Turbulent kinetic energy dissipation was measured in the Rhine ROFI in 1999 and showed a maximum in the upper half of the water column around high water, which could not yet be fully explained. The measurements were reproduced by one-dimensional models in 2006 and the dissipation maximum was attributed to a strong shear. This chapter provides detailed information about these measurements and models.

## 3.1 Measurements of the Dissipation Rate

The turbulent kinetic energy dissipation rate, $\varepsilon$, can be calculated from viscosity and velocity shear (eq. (2.9)), the latter of which is measured by means of a free-fall microstructure profiler, e.g. by a FLY (Fast Light Yoyo) (Dewey et al., 1987). This was done in the Rhine ROFI (see Fig. 5.1) over four periods of $15\ \mathrm{h}$ between 29 March and 21 May 1999 (Fisher et al., 2002).
During the first two of these periods, there were only light winds with a surface wind stress $< 0.07\ \mathrm{Pa}$. The data collected then is patched together to form two tidal cycles as shown in Fig. 3.1 for the time series of $\varepsilon_V$ and the density difference $\Delta\rho$ between $6$ and $16\ \mathrm{mab}$ (metres above the bottom).
A positive $\Delta\rho$ means that the density is higher at $6$ than at $16\ \mathrm{mab}$, i.e. stable stratification; a negative $\Delta\rho$ means the opposite; $\Delta\rho \approx 0$ characterises a homogeneous water column. Tidal straining (sec. 2.5.6) in the Rhine ROFI causes $\Delta\rho$ to be maximum at high and minimum at low water.
$\varepsilon$ has maxima at the bottom at both high and low water ($\mathrm{M}_4$ cycle), when the tidal current is alongshore, i.e. at the semi-major axes of the current ellipse. These are caused by strong tidal shear production due to bottom friction. In accordance with the north-eastward residual current (see sec. 2.5.2), the maxima are more pronounced at high than at low water. The phase delay due to the required response time for the upward penetra-

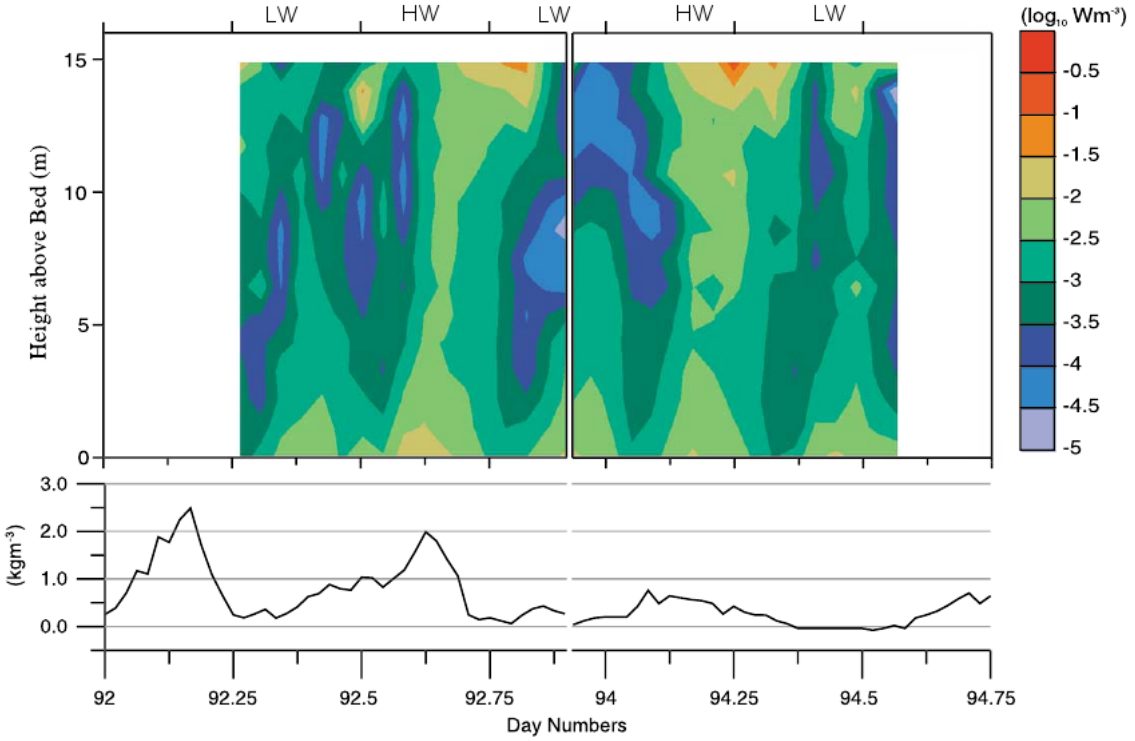


**Figure 3.1:** Measured turbulent kinetic energy dissipation rate, $\varepsilon_V$, per unit volume and density difference, $\Delta\rho$, between $6$ and $16$ mab over two tidal cycles (adapted from Fisher et al., 2002, Fig. 6). See text for description.

tion increases with height. Since tidal shear decreases with distance from the bottom, so does $\varepsilon$ up to mid-depth. Further upwards, shortly after high water, $\varepsilon$ increases again and peaks at the highest level of observation ($15$ mab, $4$ mbs (metres below the surface)). This maximum was suggested to be related to convective motions caused by unstable stratification (Fisher et al., 2002), but the water column is stably stratified around high water.

## 3.2 Modelled Dissipation Rate

The measured stratification pattern and dissipation rate was simulated by a one-dimensional Mellor-Yamada turbulence closure model (Mellor and Yamada, 1974, 1982) of levels $2$ and $2.2$ (Souza et al., 2008). In level $2$, turbulence equilibrium is assumed, i.e. equation (2.10), whereas level $2.2$ does include the time derivative and the diffusion of turbulent kinetic energy. The model was forced with horizontal sea surface slopes, cross-shore density gradients and meteorological conditions, all of which were set according to the measured data. The results are shown in Fig. 3.2.
Although the modelled dissipation rate is a factor of $5$ higher than the measured $\varepsilon$, the models well reproduce the measurements for the lower part of the water column: At the bottom, both the level $2$ and the level $2.2$ results exhibit an $M_4$ cycle of $\varepsilon$ with

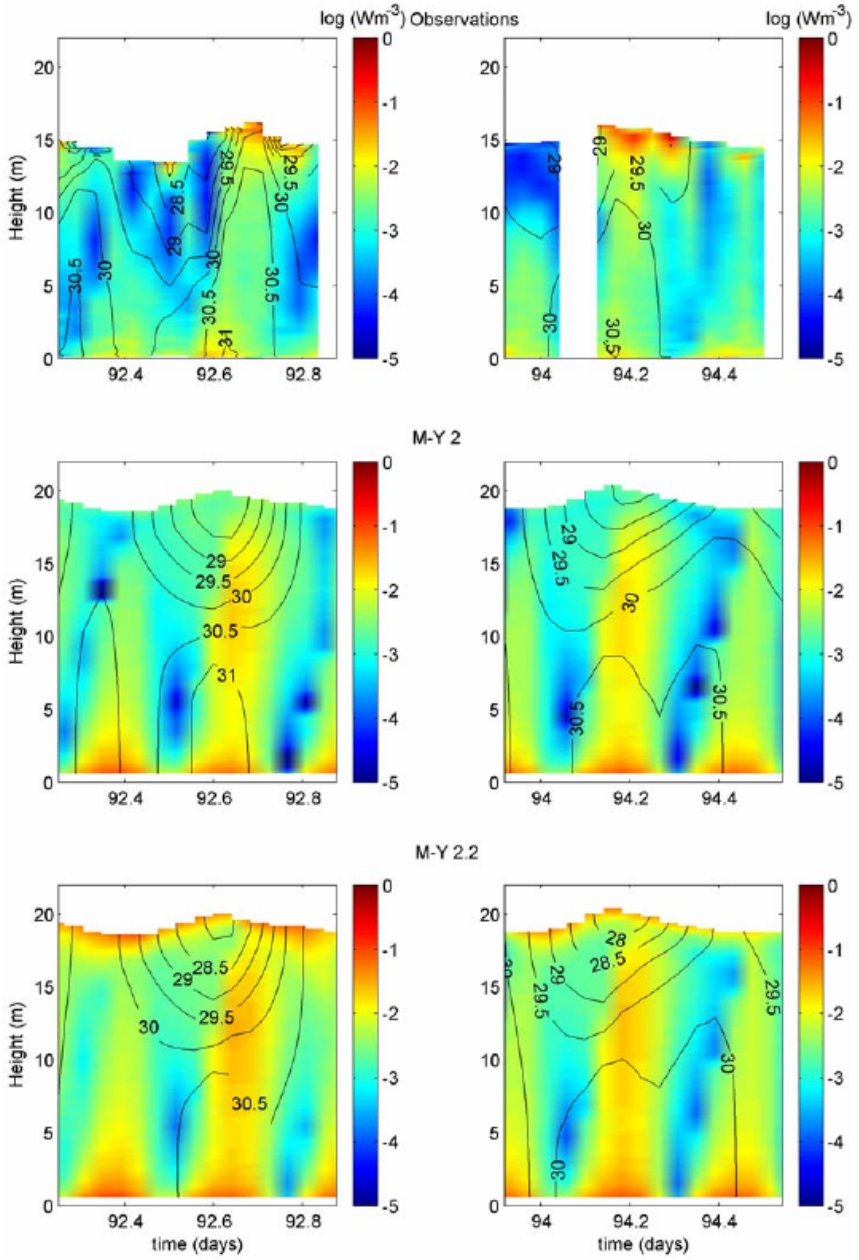


**Figure 3.2:** Measured and modelled turbulent kinetic energy dissipation rate, $\varepsilon_V$, per unit volume and salinity contours (psu) for the first two observational periods (Souza et al., 2008, Fig. 8). See text for description.

high water values greater than low water values and minima in-between. The bottom maxima decrease with height and exhibit a phase delay. However, the increase of $\varepsilon$ from mid-depth to the surface is not very well patterned: With level $2$ there is hardly any increase at all and with level $2.2$ it involves only the upper $3\ \mathrm{m}$. The difference between the models was suggested to be due to the fact that in level $2$ there is no transport of turbulent kinetic energy.
Souza et al. (2008) attributed the high dissipation rate in the upper half of the water column (days $92.7$, $94.3$) to the strong shear around and after high water, as is visible in Fig. 3.3: At HW (maximum water depth in Fig. 3.3a), the alongshore shear (b) has maximum absolute values, which are, due to the residual current, in the northeastward direction, double as great as the extreme values at low water or those of the cross-shore shear (c). Approximately six hours later, the cross-shore shear is maximum.
Furthermore, stratification is almost always stable: Only around low water, a small negative salinity difference occurs (d).

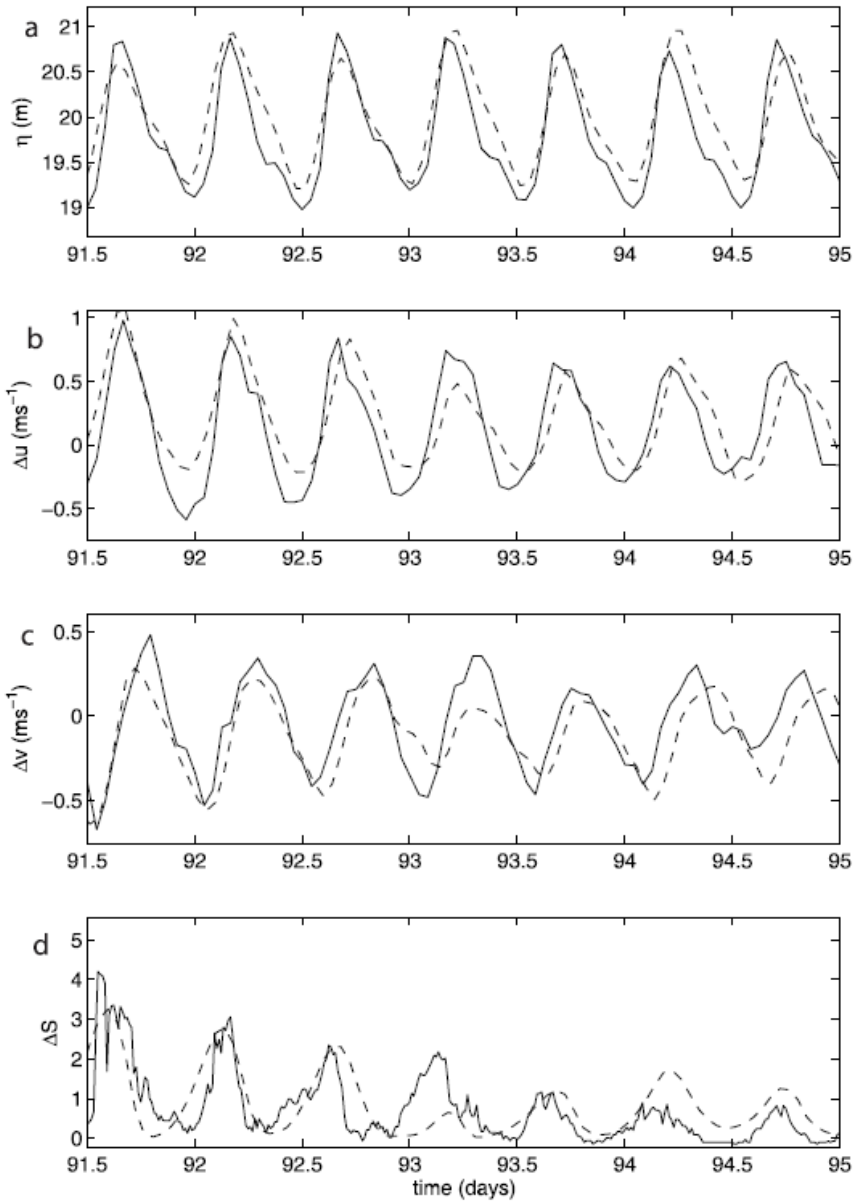


**Figure 3.3:** Comparison of modelled (dashed) and measured data (solid line): **a** surface elevation, **b** alongshore and **c** cross-shore shear defined as the velocity difference between $16$ and $2$ mab, **d** salinity difference (psu) between $13.5$ and $3.5$ mab (Souza et al., 2008, Fig. 6). See text for description.

# Chapter 4

# Method: Simulations with GETM

The temporal and spatial evolution of the turbulent kinetic energy dissipation rate, $\varepsilon$, and relevant physical properties are investigated by means of three-dimensional simulations using the General Estuarine Transport Model (GETM). The applied set-up and boundary conditions are described in this chapter.

## 4.1 General Estuarine Transport Model

For information on the General Estuarine Transport Model (GETM[1]), please refer to section 5.4.

## 4.2 Model Set-Up

The Rhine ROFI is simulated by the grid de Boer et al. (2006) used for their investigations. It is a rectilinear grid with grid cells of $500\ \mathrm{m} \times 500\ \mathrm{m}$ close to the plume region and zooming out toward the northwest (left) and -east (top) boundary (see Fig. 4.1(b)). The orientation is such that the right-hand side of the domain aligns with the coast, which is idealised by a straight line. The water depth is $20\ \mathrm{m}$ in the open sea, i.e. the bottom is flat; the depth of the Rhine river, which is $500\ \mathrm{m}$ wide (one grid cell) and $75\ \mathrm{km}$ long, linearly decreases from $20\ \mathrm{m}$ at the mouth to $5\ \mathrm{m}$ at the freshwater source. In order to save storage and simulation time, the river is angled and lies parallel to the coastline. It cannot be omitted since it is needed for the development of an estuarine circulation and the related formation of a salt wedge (see sec. 2.1).
The model is forced by a constant river runoff, a surface elevation according to a Kelvin wave solution at the three open boundaries and, in one case, a constant wind. These three forcings are varied according to Tab. 5.1 in order to investigate the influence of discharge volume, tidal range and wind.
The sea surface elevation in the entire domain is determined by the elevation $\eta(x, y, t)$

[1] http://www.getm.eu

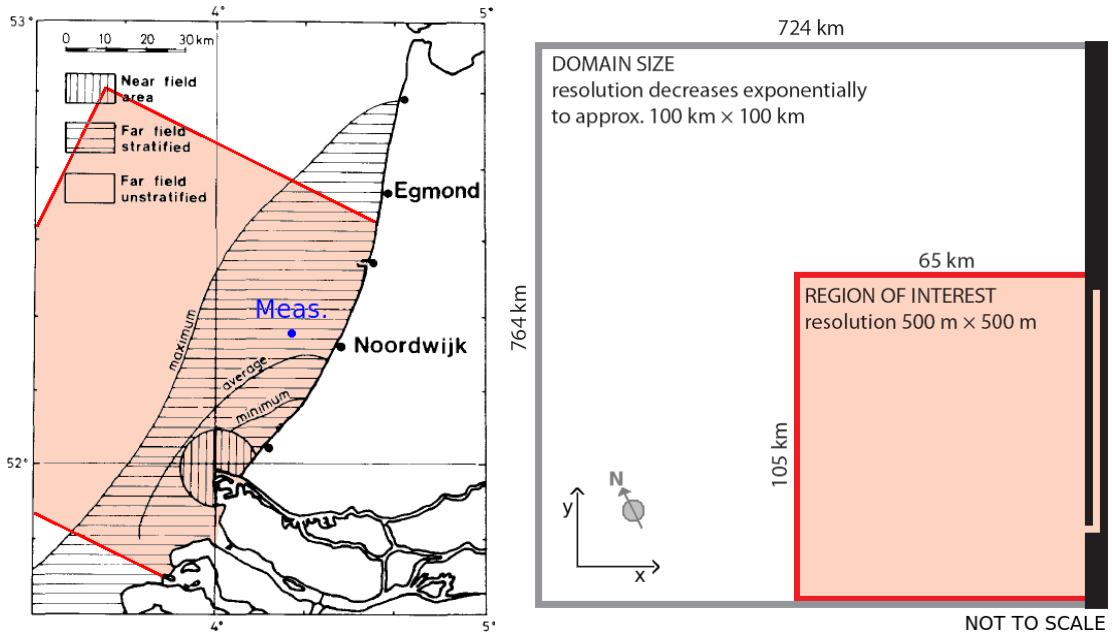


(a) Approximate position of the inner model(b) Schematic of the model domain with information on domain (red box) and the water column of thelengths and grid resolution. The compass rose indicates measurements (blue dot, B in Fig. 5.1). the orientation.

**Figure 4.1:** Position and schematic of the model domain. From (a) (adapted from van der Giessen et al., 1990, Fig. 5) to (b) (by R. D. Hetland and E. Fischer), the coordinate system is rotated approx. $30°$ in the counterclockwise direction.

at the open boundaries (cp. sec. 2.5.4, eq. (2.1); derivation in app. A.1):

$$\eta = a \exp\left(\frac{f}{c}x\right) \cos(ky - \omega t)$$

with the parameters as given in Tab. 4.1. $x$ is the distance from the coast (negative, $0$ at coast), $y$ the alongshore dimension and $t$ the time.

| parameter | meaning | value |
|---|---|---|
| $a$ | amplitude at coast | $1\ \mathrm{m}$ or $1.25\ \mathrm{m}$ |
| $f = 2\omega \sin(\mathrm{lat})$ | Coriolis frequency | $1.146 \cdot 10^{-4}/\mathrm{s}$ |
| $c = \sqrt{gH}$ | wave speed | $14.005\ \mathrm{m/s}$ |
| $g$ | gravitational acceleration | $9.80665\ \mathrm{m/s^2}$ |
| $H$ | water depth | $20\ \mathrm{m}$ |
| $k = \omega/c$ | wave number | $1.003 \cdot 10^{-5}/\mathrm{m}$ |
| $\omega = 2\pi/T$ | angular frequency | $1.405 \cdot 10^{-4}/\mathrm{s}$ |
| $T$ | tidal periodic time | $44,714\ \mathrm{s}\ (\mathrm{M}_2)$ |

**Table 4.1:** Parameters for the sea surface elevation $\eta$. ($\mathrm{lat}$ means latitude; for the simulations, a constant latitude of $52°\mathrm{N}$ is assumed.)

# Part II

# Results, Discussions and Conclusions

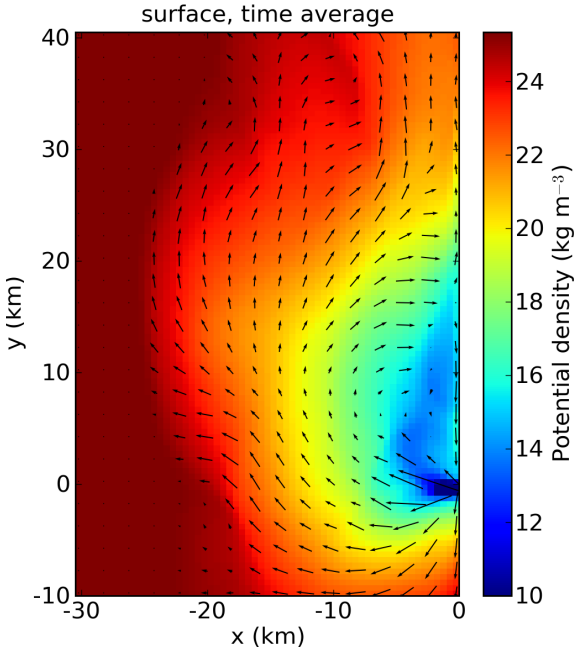

# Chapter 5

# Numerical Investigations of the TKE Dissipation Rate in the Rhine ROFI

This chapter agrees to a large extent with a paper submitted to the PECS 2008 special issue of *Ocean Dynamics*. The authors are Elisabeth Fischer[1], Hans Burchard[1] and Robert D. Hetland[2].

**Abstract** The turbulent kinetic energy dissipation rate, $\varepsilon$, in tidal seas is maximum at the bottom during full flood and during full ebb, i.e. when tidal currents are strongest. In coastal regions with tides similar to a Kelvin wave, this coincides with high water and low water. Stratification in such a region is most stable at high water and least at low water, assuming an estuary in the vicinity supplying freshwater.
Measurements of $\varepsilon$ in the Rhine region of freshwater influence have revealed bottom maxima at both high and low water. In addition, a maximum in the upper half of the water column was found around high water, which cannot be explained by tidal shear at the bottom, convective instabilities or wind mixing.
This study investigates the dissipation rate and relevant physical properties in the Rhine region of freshwater influence by means of three-dimensional numerical simulations using the General Estuarine Transport Model and idealised conditions. The measurements are well reproduced; two distinct peaks of $\varepsilon$ are evident in the upper layer shortly before as well as after high water. These maxima turn out to be due to strong peaks in the alongshore shear occurring when the fore- and the back front of the plume transit the water column.

**Keywords** dissipation rate maximum · Rhine ROFI · 3D numerical modelling

[1] Leibniz Institute for Baltic Sea Research Warnemünde, Seestrasse 15, 18119 Rostock, Germany
[2] Department of Oceanography, Texas A&M University, 3158 TAMU, College Station TX 77845, USA

## 5.1 Introduction

A region of freshwater influence (ROFI, term adopted by Simpson et al., 1993) is that part of a shelf sea which is adjacent to an estuary and, thus, strongly affected by the buoyancy input due to riverine water. The freshwater forms a buoyant plume, the extension and life time of which depend on the respective circumstances, e.g. river run-off and ambient currents. The stratification in ROFIs is strongly subjected to these conditions, especially to the stirring by tides and wind, which are particularly effective because of the shallowness. If mixing is low, tidal straining drives a periodic cycle of stratification (Simpson et al., 1990).

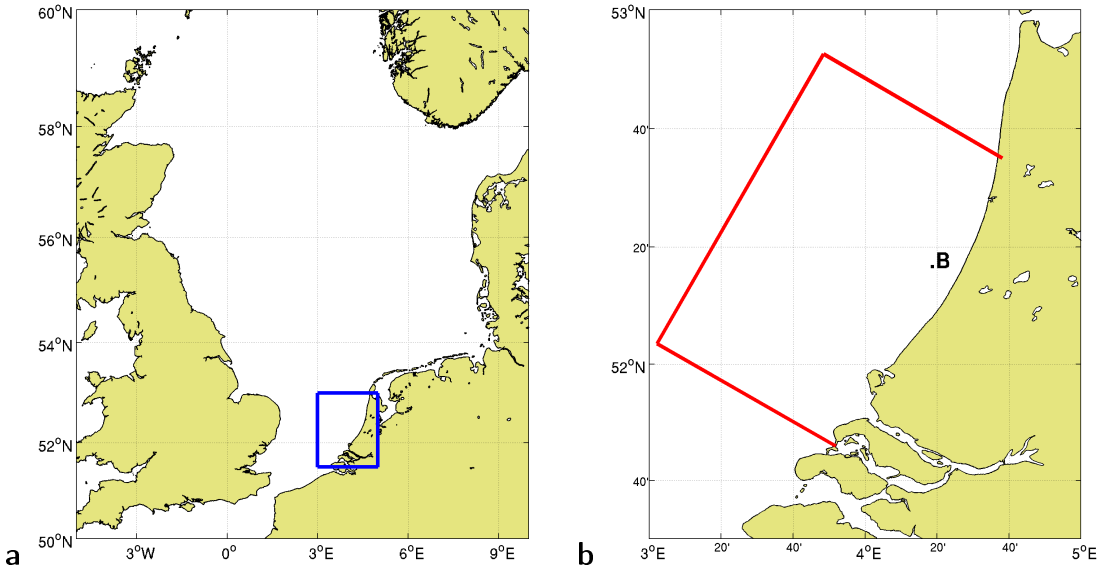


**Figure 5.1:** **a** North Sea and **b** Dutch coast with the Rhine-Meuse delta. The measurements were taken at position B ($52°18'\mathrm{N}$, $04°18'\mathrm{E}$), that is approx. $11\ \mathrm{km}$ offshore and $41\ \mathrm{km}$ north-east of the Rhine estuary. The red lines indicate the inner model domain (compare Fig. 5.3).

At the southeast coast of the Southern Bight of the North Sea (Fig. 5.1), the Rhine discharges $2,200\ \mathrm{m^3/s}$ on average, which gives rise to an approximately $30\ \mathrm{km}$ wide and $100\ \mathrm{km}$ long ROFI along the Dutch coast: the Rhine ROFI (Souza and Simpson, 1997). Due to the Coriolis force and the prevailing west and southwest winds, the Rhine plume is deflected northeastward and provides the main freshwater input to the Dutch coastal current (Souza and Simpson, 1996; de Ruijter et al., 1997). The depth-averaged residual flow, i.e. the depth-averaged tidal mean velocity, points northeastward and ranges between $3$ and $8\ \mathrm{cm/s}$ (van Alphen et al., 1988). The surface residual reaches $15$ to $20\ \mathrm{cm/s}$ in the stratified area, but is much weaker outside (Simpson et al., 1993). Stratification in the Rhine ROFI is governed by variable discharge and wind as well as by periodic tides. Both discharge and wind follow a seasonal cycle with maximum discharge in winter and early spring and strongest southwest winds from mid summer to mid winter (Visser et al., 1991), but they are unpredictable on short time scales. The dominating tide is the semi-diurnal principal lunar tide, $M_2$, which can be regarded as a Kelvin wave

progressing northeastward along the Dutch coast. The tidal range at the coast is $1.5\ \mathrm{m}$ at neap and $1.9\ \mathrm{m}$ at spring. Maximum surface currents are $0.8$ or $1.1\ \mathrm{m/s}$ northeastward during flood and $0.7$ or $0.9\ \mathrm{m/s}$ southwestward during ebb, respectively at neap or spring (van Alphen et al., 1988).

The vertically averaged tidal current is rectilinear alongshore, but stratification has a significant impact on the tidal ellipses and vice versa (Visser et al., 1994; Souza and Simpson, 1996; Souza and James, 1996): During well mixed conditions, the ellipses are near-degenerate with a very slight clockwise component at the surface and a small counterclockwise component at the bottom. During neap tides with weak wind forcing, estuarine circulation driven by horizontal density gradients induces stratification. At the pycnocline between $5$ and $10\ \mathrm{mbs}$ (metres below surface), the decoupling into two layers restrains the transfer of momentum which has different significance for the two rotary components (Prandle, 1982): Since in the Rhine ROFI the characteristic bottom boundary layer thickness, up to which bottom friction influences the flow, is $30\ \mathrm{m}$ for the clockwise and $10\ \mathrm{m}$ for the counterclockwise component, the latter reaches its free-stream value at mid-depth, i.e. already below the pycnocline, so that it is not affected by the decoupling. For the clockwise component, on the other hand, the reduction of friction in the upper layer means a significant enhancement giving rise to a plainly clockwise rotation of the surface ellipses. Simultaneously, the frictional forces intensify in the lower layer and further reduce the clockwise component so that bottom ellipses gain a counterclockwise rotation (Souza and Simpson, 1996).

With the current structure as described, the alongshore velocities at both surface and bottom are in phase with the sea surface elevation. The cross-shore velocities at surface and bottom, in contrast, are $180°$ out of phase to each other with maximum onshore currents occurring at the surface between high and low water and at the bottom between low and high water (as explained by a linearised water column model with constant viscosity (Prandle, 1982) and a simple two-layer model with linear bed and interfacial friction (Visser et al., 1994)). This results in a strong periodic cross-shore shear which interacts with the horizontal density gradients, a process called tidal straining, which drives a periodic cycle of stratification (Strain-Induced Periodic Stratification, SIPS, Simpson et al. (1990)): Between low and high water, fresher water is transported offshore at the surface and saline water is forced onshore below so that stratification is established and reaches its maximum at high water. In the other half cycle, shear points in the opposite direction and tidal straining reduces stratification to a minimum at low water (Souza and James, 1996). In a recent study, de Boer et al. (2008) could show that also alongshore density gradients are significant and that the effective straining is a combination of along- and cross-shore contributions. However, if stirring is too high, e.g. due to strong winds or at spring tide, there is no SIPS, but the water column is well mixed over the entire tidal cycle.

Shear has maxima at the bottom at both high and low water when currents are directed alongshore and exhibit their highest velocity. This tidal shear is due to bottom friction reducing the tidal current velocity. At the surface, wind stress may cause wind shear. Shear appears in a source term of the turbulent kinetic energy ($\mathrm{TKE}$) budget equation,

which, after adopting the eddy viscosity assumption, reads as:

$$\frac{\mathrm{D(TKE)}}{\mathrm{D}t} = P + B - \varepsilon + T \tag{5.1}$$

with $\mathrm{D}/\mathrm{D}t = \partial/\partial t + u_i \partial/\partial x_i$ the total derivative, $P = \nu_t S^2$ the shear production ($\nu_t$ eddy viscosity of momentum, $S^2 = (\partial u/\partial z)^2 + (\partial v/\partial z)^2$ shear squared), $B = -\nu_t' N^2$ the buoyancy production ($\nu_t'$ eddy diffusivity, $N^2 = -g/\rho_0 \cdot \partial\rho/\partial z$ Brunt-Väisälä or buoyancy frequency), $\varepsilon$ the $\mathrm{TKE}$ dissipation rate and $T$ transport terms.
In turbulence equilibrium, equation (5.1) becomes

$$\varepsilon = P + B \; . \tag{5.2}$$

$P$ is always a source term of $\mathrm{TKE}$; $B$ is positive ($\mathrm{TKE}$ production) for unstable stratification (conversion of potential into turbulent kinetic energy) and negative ($\mathrm{TKE}$ consumption) for stable stratification (conversion of turbulent kinetic into potential energy). $\varepsilon$ is positive and means a conversion of $\mathrm{TKE}$ into heat. According to equation (5.2), $\varepsilon$ can be high for two reasons: Either there is strong shear or there is unstable stratification causing convective motions.

In the next section, the measurements of $\mathrm{TKE}$ dissipation in the Rhine ROFI are described. Section 5.4 gives detailed information on the numerical model used for this work; the results are presented and discussed in the sections 5.5 and 5.6. Summary and conclusion can be found in section 5.7.

## 5.2 Observations

The turbulent kinetic energy dissipation rate, $\varepsilon$, was measured by means of the free-fall microstructure profiler FLY (Fast Light Yoyo) in the Rhine ROFI (approx. $11\ \mathrm{km}$ offshore and $41\ \mathrm{km}$ northeast of the Rhine estuary, see Fig. 5.1) over four periods of $15\ \mathrm{h}$ between 29 March and 9 April 1999 (Fisher et al., 2002). During the first two of these periods, there were only light winds with surface wind stress $< 0.07\ \mathrm{Pa}$. The data collected then is shown in Fig. 5.2.
$\varepsilon$ has maxima at the bottom at both high and low water ($\mathrm{M}_4$ cycle), which are caused by strong tidal shear production due to bottom friction occurring when the tidal current is alongshore, i.e. at the semi-major axes of the current ellipse. In accordance with the northeastward residual current, the maxima are more pronounced at high than at low water. They exhibit a phase delay increasing with height, which is due to the time lag in the upward penetration of the frictional effects. Since tidal shear decreases with distance from the bottom, so does $\varepsilon$ up to mid-depth. Further upwards, shortly after high water, $\varepsilon$ increases again and peaks at the highest level of observation ($15\ \mathrm{mab}$ (metres above bottom), $4\ \mathrm{mbs}$). Fisher et al. (2002) suggested this maximum to be related to convective motions caused by unstable stratification, but the water column is stably stratified around high water.

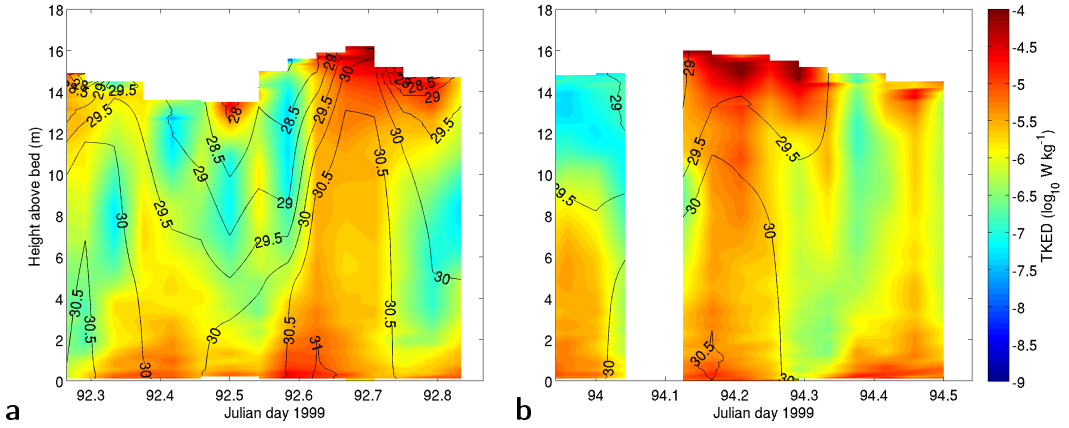


**Figure 5.2:** Temporal evolution of turbulent kinetic energy dissipation rate, $\varepsilon$, and salinity (g/kg) measured approximately $11$ km offshore and $41$ km northeast of the Rhine estuary on **a** 2 and **b** 4 April 1999.

The measured stratification pattern and dissipation rate have been simulated by (Souza et al., 2008) using a one-dimensional turbulence closure model. The model was forced with horizontal sea surface slopes, cross-shore density gradients and meteorological conditions, all of which were set according to the measured data. The results are in good agreement with the measurements though the increase of $\varepsilon$ from mid-depth to the surface is not very well reproduced.
Souza et al. (2008) attributed the high dissipation rate in the upper half of the water column to a strong shear around and after high water (according to their model): At HW, the alongshore shear has maximum absolute values, which are, due to the northeastward residual current, double as great as the extreme values at low water or those of the cross-shore shear. Approximately six hours later, the cross-shore shear is maximum.

## 5.3 Motivation

The observed maximum of the turbulent kinetic energy dissipation rate is not caused by tidal shear production at the bottom, for $\varepsilon$ increases in the upper half of the water column; it is not generated by convective motions resulting from instabilities, for stratification is stable, especially at high water, and it is not related to meteorology, for winds were weak during the measurements. The maximum appears to be caused by strong alongshore shear at high water and cross-shore shear shortly thereafter. However, the following questions have not yet been considered, among others:

- Why is there such a strong shear production around $5$ mbs, where the measured $\varepsilon$ is maximum?
- What does $\varepsilon$ look like in the upper $5$ m of the water column?
- Is there a spatial context between $\varepsilon$ or rather the shear and the freshwater plume?

These questions are to be answered by idealised three-dimensional simulations without assimilating specific conditions taken from the measurements like in Souza et al. (2008).

## 5.4 Model Set-Up

The General Estuarine Transport Model (GETM, see Burchard and Bolding (2002), Burchard et al. (2004)), which has been used for the present three-dimensional numerical study, uses bottom and surface fitted coordinates and is equipped with high-order advection schemes, as described by Pietrzak (1998). The vertical turbulent transport is calculated by means of the General Ocean Turbulence Model (GOTM, see Umlauf et al. (2005)), including two-equation turbulence closure models as discussed by Burchard and Bolding (2001) and Umlauf and Burchard (2003). In the simulations presented here, the $k$-$\varepsilon$ model coupled to the algebraic second-moment closure by Cheng et al. (2002) is used.
GETM has been successfully applied to several coastal, shelf sea and limnic scenarios, see e.g. Stanev et al. (2003) and Burchard et al. (2008) for turbulent flows in the Wadden Sea, Stips et al. (2004) for dynamics in the North Sea, Staneva et al. (2009) for sediment dynamics in the German Bight, Burchard et al. (2005) and Burchard et al. (2009) for studies of dense bottom current passages in the Western Baltic Sea, Banas and Hickey (2005) for estimating exchange and residence times in the Willapa Bay in Washington State and Umlauf and Lemmin (2005) for a basin-exchange study in Lake Geneva.

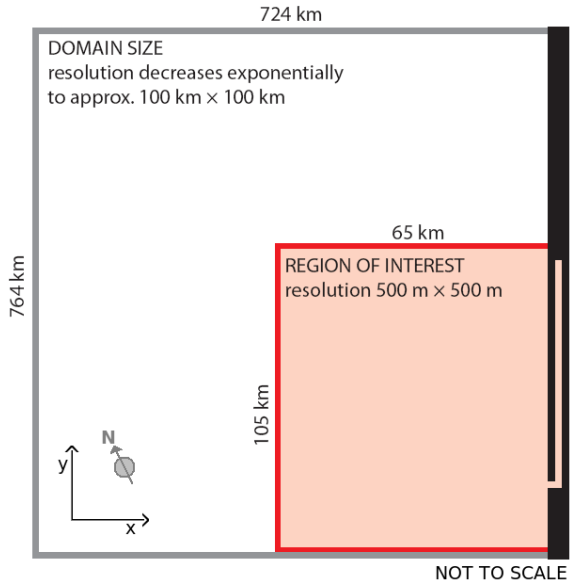


**Figure 5.3:** Schematic of the model domain with information on lengths and grid resolution. The compass rose indicates the orientation: Relative to Fig. 5.1, the coordinate system is rotated by approx. $30°$ in the counterclockwise direction.

The Rhine ROFI is simulated by the grid de Boer et al. (2006) used for their investiga-

tions. It is a rectilinear grid with grid cells of $500\ \mathrm{m} \times 500\ \mathrm{m}$ close to the plume region and zooming out toward the northwest (left) and -east (top) boundary (see Fig. 5.3); the vertical resolution is $40$ layers, i.e. $0.5\ \mathrm{m}$ (tidal mean). The orientation is such that the right-hand side of the domain aligns with the coast, which is idealised by a straight line. The water depth in the open sea is $20\ \mathrm{m}$, i.e. the bottom is flat; the depth of the Rhine river, which is $500\ \mathrm{m}$ wide (one grid cell) and $75\ \mathrm{km}$ long, linearly decreases from $20\ \mathrm{m}$ at the mouth to $5\ \mathrm{m}$ at the freshwater source. In order to save memory, the river is angled and lies parallel to the coastline. It cannot be omitted since it is needed for the development of an estuarine circulation and the related formation of a salt wedge. The model is forced by a constant river runoff, a surface elevation according to a Kelvin wave solution ($\mathrm{M}_2$, $T = 44,714\ \mathrm{s}$) at the three open boundaries and, in one case, a constant wind. These three forcings are varied according to Tab. 5.1 in order to investigate the influence of discharge volume, tidal range and wind. The LMC set-up corresponds to the average state. (In the introduction, a tidal range of $1.9\ \mathrm{m}$ has been associated with spring tide. However, we considered the magnitude of the currents to be more important and a comparison of the simulated currents with the literature data showed that a tidal range of $2.0\ \mathrm{m}$ leads to mean tidal currents.)

| set-up ID | discharge ($\mathrm{m}^3/\mathrm{s}$) | tidal range ($\mathrm{m}$) | wind stress ($\mathrm{Pa}$) |
|---|---|---|---|
| LMC | $1,500$ | $2.00$ | none |
| HMC | $2,200$ | $2.00$ | none |
| LSC | $1,500$ | $2.50$ | none |
| LMW | $1,500$ | $2.00$ | $0.125$ from SW |

**Table 5.1:** Variations of the model forcings. The three set-up ID digits respectively stand for one of the two options of the forcings: discharge (H high, L low), tidal range (S spring, M mean) and wind (W southwest wind, C calm). The tidal range refers to the range at the coast.

At the beginning of each model run, the forcings are spun up linearly; the spin-up times are $24\ \mathrm{h}$ for the Rhine river discharge, a quarter tidal period ($\approx 3.1\ \mathrm{h}$) for the sea surface elevation and, as the case may be, one tidal period ($T = 44,714\ \mathrm{s} \approx 12.4\ \mathrm{h}$) for the wind. The model runs $30$ tidal periods until a quasi-periodic state is reached, i.e. the results shown in this paper are obtained from the $31$st period.

## 5.5 Results

### 5.5.1 Plume Structure in the Different Set-Ups

In order to give an impression of the position of the freshwater plume and the stratification in the Rhine ROFI, the modelled salinity is shown in Fig. 5.4. The distribution and mixing of the riverine water highly depends on discharge, tidal range and wind:
For a typical discharge, a mean tidal range and without wind (LMC set-up), the plume is approximately $20\ \mathrm{km}$ wide and $5\ \mathrm{m}$ thick. With time and, consequently, increasing northeastward distance from the river mouth, mixing reduces the stratification; the plume

attaches to the bottom and becomes narrower until vertical homogeneity is attained.
A higher discharge (HMC) causes a wider and thicker plume. The attachment to the bottom takes place closer to the river mouth, but stratification in the upper layer extends farther.
Spring tides (LSC) involve strong stirring at the bottom. Freshwater is mixed down already in front of the river mouth and vertical homogeneity is attained very soon.
Wind (LMW) has two effects: First, it induces mixing in the upper part of the water column so that there is no vertical stratification. Second, it moves the freshwater in the according direction. A strong southwest wind not only elongates the plume along the coast, but also causes downwelling. The plume reduces to a width of $5\ \mathrm{km}$ and ranges from the surface to the bottom.

### 5.5.2 Turbulent Kinetic Energy Dissipation Rate

Plan views of the modelled turbulent kinetic energy dissipation rate shortly before high water are shown in the first two columns of Fig. 5.5. For each case, one water column with high $\varepsilon$ at $2\ \mathrm{mbs}$ is chosen for comparison with the observations.
In the LMC set-up, the surface dissipation is highest at the northwest edge of the plume. The tidal cycle of the chosen water column exhibits maxima at the bottom at both high and low water, decreasing with height and showing a distinct phase delay. The bottom maximum at high water penetrates less far upward than the one at low water, which reaches up to the surface. In the upper $5\ \mathrm{m}$, $\varepsilon$ is highest about half an hour before as well as two hours after high water. Approximately two hours before low water, there is a smaller local peak. These three maxima come along with an increase of dissipation from mid-depth to the surface, which does not occur around low water.
With a higher discharge (HMC), the high dissipation rate below the surface covers a larger horizontal range. The temporal evolution is very similar, but $\varepsilon$ is smaller directly below the surface.
Increased stirring due to spring tides (LSC) deforms the plume and, thus, the distribution of dissipation. Both values and horizontal extent of the maximum $\varepsilon$ below the surface are smaller than in the LMC case. The bottom maxima, on the contrary, are higher and penetrate farther upward.
Stirring by strong winds (LMW) results in high dissipation in the upper $3$ to $5\ \mathrm{m}$, but it also inhibits the spatial and temporal variability. Consequently, the maxima of $\varepsilon$ in the upper layer around high water are more difficult to distinguish.

### 5.5.3 Tidal Cycle of Salinity and Stratification

In the two set-ups which are not subject to strong mixing by spring tides or wind, the isohalines exhibit a distinct descent at the time of the highest surface dissipation (Fig. 5.5c, f): In both cases, the isohalines in the upper layer stay at approximately constant height from low water to shortly before high water. Then, in the LMC set-up, they slightly ascend (salinity increases) before rather sharply descending (salinity decreases), which, in turn, is followed by a slower upward movement at and after high

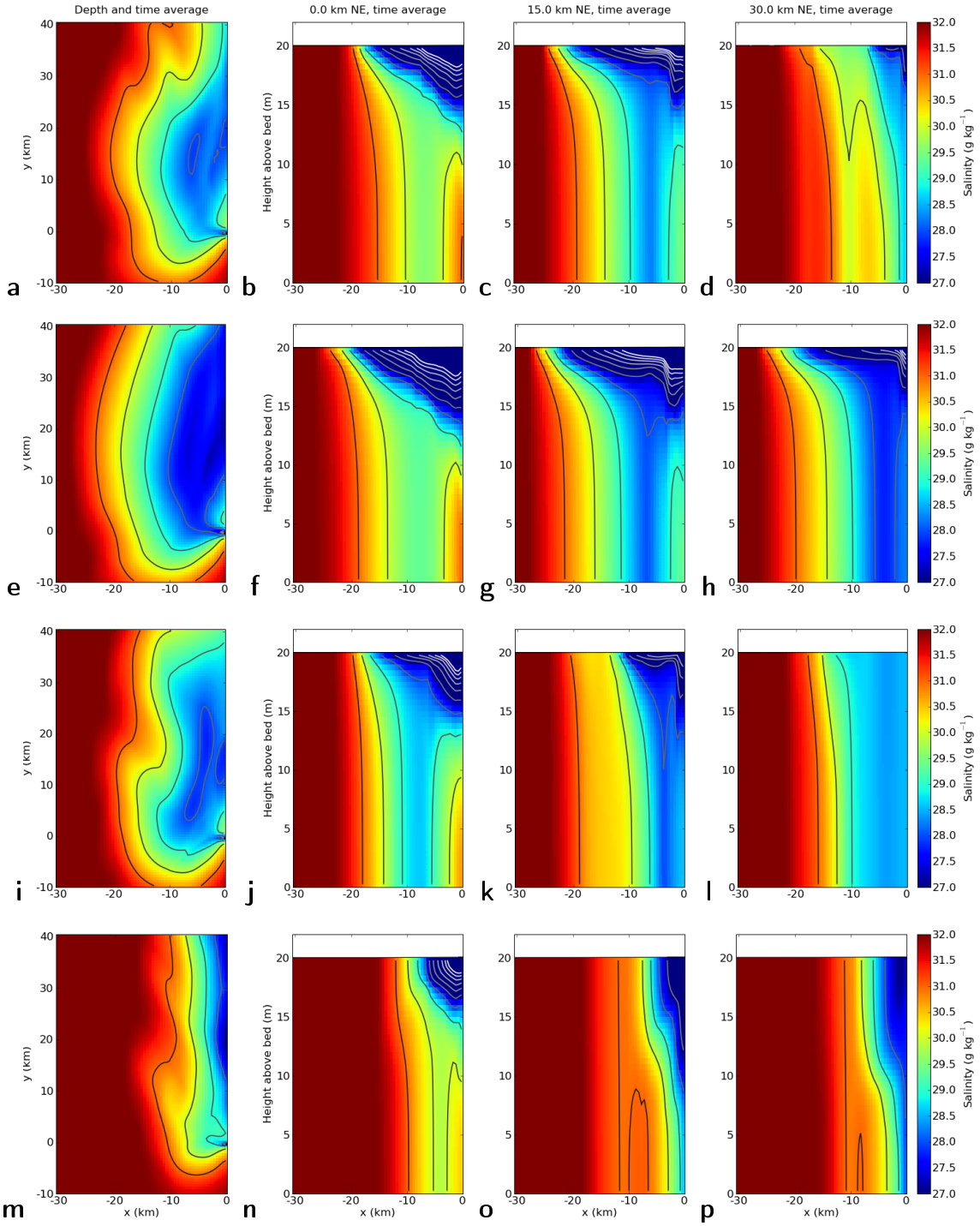


**Figure 5.4:** Salinity and isohalines ($1$ g/kg intervals) in the four different set-ups LMC, HMC, LSC and LMW (from top to bottom). The first column depicts plan views of the depth- and time- averaged salinity; the last three columns are time-averaged cross-sections at $0$, $15$ and $30$ km northeast of the river mouth (from left to right).

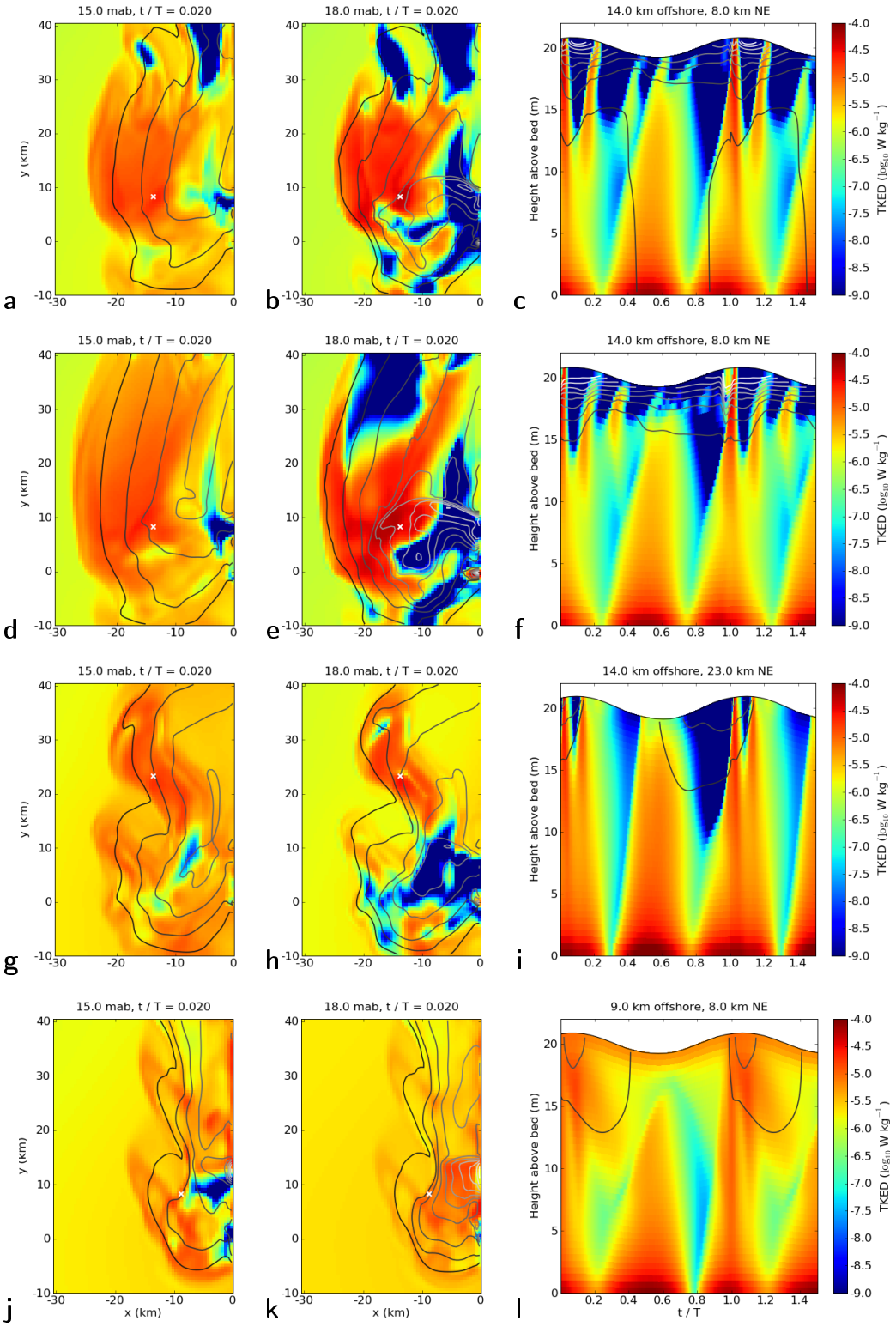


**Figure 5.5:** Turbulent kinetic energy dissipation rate with isohalines ($1\ \mathrm{g/kg}$ intervals) in the four different set-ups LMC, HMC, LSC and LMW (from top to bottom). The first two columns depict plan views of $15$ or rather $18\ \mathrm{mab}$ at the time of the upper-layer maximum $\varepsilon$; the white crosses mark the water columns of which the temporal evolution is shown in the last column. (High water coincides with $t/T = 0.075$, $T = 44,714$ s.)

water. With a higher discharge (HMC), the descent takes place faster and the upward movement occurs in two steps, which are separated by another local maximum in height.

## 5.6 Discussion

### 5.6.1 Comparison with the Observations

The simulated turbulent kinetic energy dissipation rate is in good agreement with the observations. The model seems to overestimate the bottom maxima and the upward penetration at low water, but the increase approximately from $6$ to $15$ mab around high water is well reproduced. Regarding the order of magnitude, the wind set-up (LMW) provides the best approach.
However, since the dissipation maximum below the surface is most distinct in the LMC set-up, only this one will be considered in the following investigations.

### 5.6.2 Sources of the High Dissipation Rate

#### 5.6.2.1 Turbulent Quantities

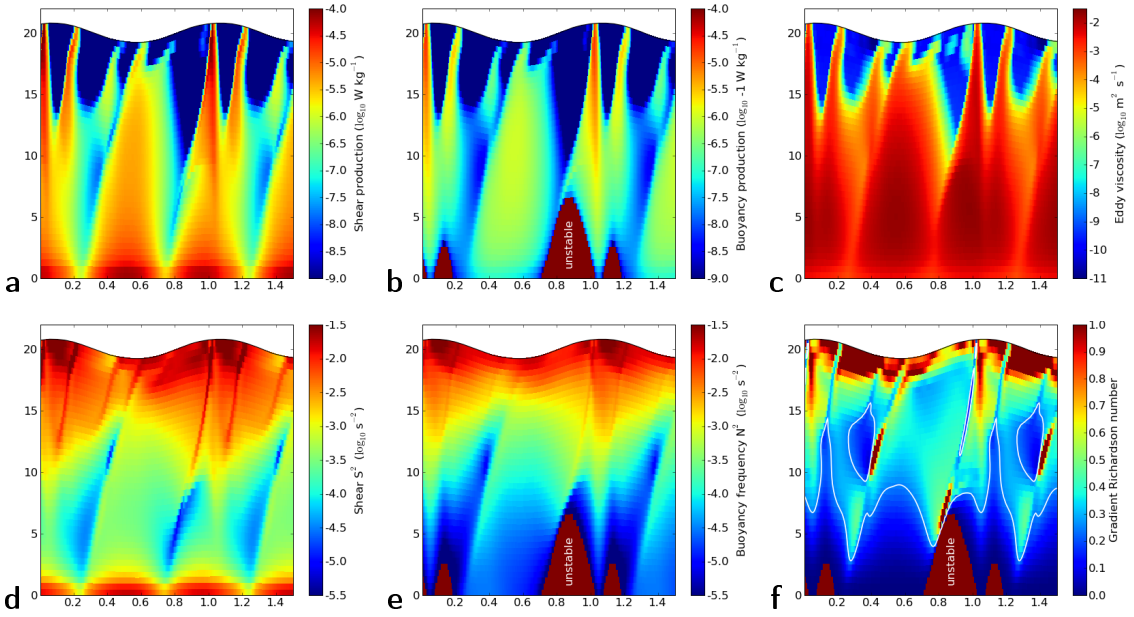


**Figure 5.6:** One and a half tidal cycles of turbulent quantities in the LMC set-up (water column $14$ km offshore and $8$ km northeast of river mouth, x-axis $t/T$ and y-axis mab as in Fig. 5.5c). **a** shear production, $P$, **b** buoyancy production, $B$ (logarithm of the additive inverse), **c** eddy viscosity of momentum, $\nu_t$, **d** shear squared, $S^2$, **e** buoyancy frequency, $N^2$, **f** gradient Richardson number, $Ri = N^2/S^2$, with isoline at $Ri = Ri_c = 0.25$. The brown patches at the bottom are related to unstable stratification (density increasing with height). There, $N^2$ and $Ri$ are negative and $B$ is positive.

Most of the time, stratification is stable, involving a positive buoyancy frequency, $N^2$ (Fig. 5.6e), a negative buoyancy production, $B$ (Fig. 5.6b), and, according to equation (5.2), $\varepsilon < P$. Only in the lower part of the water column, between low and high water as well as shortly after high water, stratification is unstable, meaning negative $N^2$, positive $B$ and $\varepsilon > P$.
A comparison of the dissipation rate (Fig. 5.5c) and the shear production (Fig. 5.6a) yields to $\varepsilon \approx P$. In accordance with this and equation (5.2), the absolute value of the buoyancy production is approximately one order of magnitude smaller than $\varepsilon$ and $P$, though it follows the same pattern. Consequently it can be reasoned that the (dissipated) turbulent kinetic energy is principally shear-generated.
Clearly, the shear squared, $S^2$ (Fig. 5.6d), exhibits distinct features very similar to the pattern of $P$ and $\varepsilon$: At the bottom, there are maxima at both high and low water decreasing with height and showing a phase delay; furthermore, two individual branches of high $S^2$ propagate from mid-depth to the surface, where they reach their maximum. These branches coincide with the rising edges of the below-surface maxima of shear production and dissipation rate.
The strong shear maxima occurring directly before as well as between the two branches, however, do not generate elevated levels of $\varepsilon$. This can be understood when considering the buoyancy frequency $N^2$ (Fig. 5.6e) at that position and time: $N^2$ is maximum (positive) at the surface, especially around high water, i.e. stratification is most stable and, thus, able to restrain the development of turbulence (see eddy viscosity, $\nu_t$, Fig. 5.6c). At the times of the high-shear branches, $N^2$ has local maxima, too, but they are relatively small in comparison to the shear maxima.
This relationship is well represented by the gradient Richardson number, $Ri = N^2/S^2$ (Fig. 5.6f): At the bottom, $Ri$ is low, particularly lower than the critical Richardson number, $Ri_\mathrm{c} = 0.25$, indicating mixing due to shear instabilities. In the upper layer, $Ri$ is generally high, meaning dynamic stability, except for the patches of shear maxima where $Ri$ is decreasing toward $Ri_\mathrm{c}$.

What causes this high shear squared coinciding with less stability so that turbulence is generated?

#### 5.6.2.2 Velocities and Shear

In order to explain the shear squared, $S^2$, the horizontal velocities (Fig. 5.7a, b) need to be examined: The alongshore velocity, $v$, is approximately double as high as the cross-shore velocity, $u$. It is in phase with the surface elevation and increases from bottom to surface. The absolute alongshore velocity at the surface is higher at high water than at low water, which is due to the tidal and density-driven residual current in the north-eastward direction. The cross-shore velocity exhibits a phase shift of $180°$ between the upper layer and the lower $15\ \mathrm{m}$. The resulting current ellipses have a clockwise sense of rotation at the surface and a counterclockwise sense of rotation below $15\ \mathrm{mab}$. The transition takes place in the area of the pycnocline.
The alongshore shear, i.e. the vertical gradient of the alongshore velocity, $\mathrm{d}v/\mathrm{d}z$

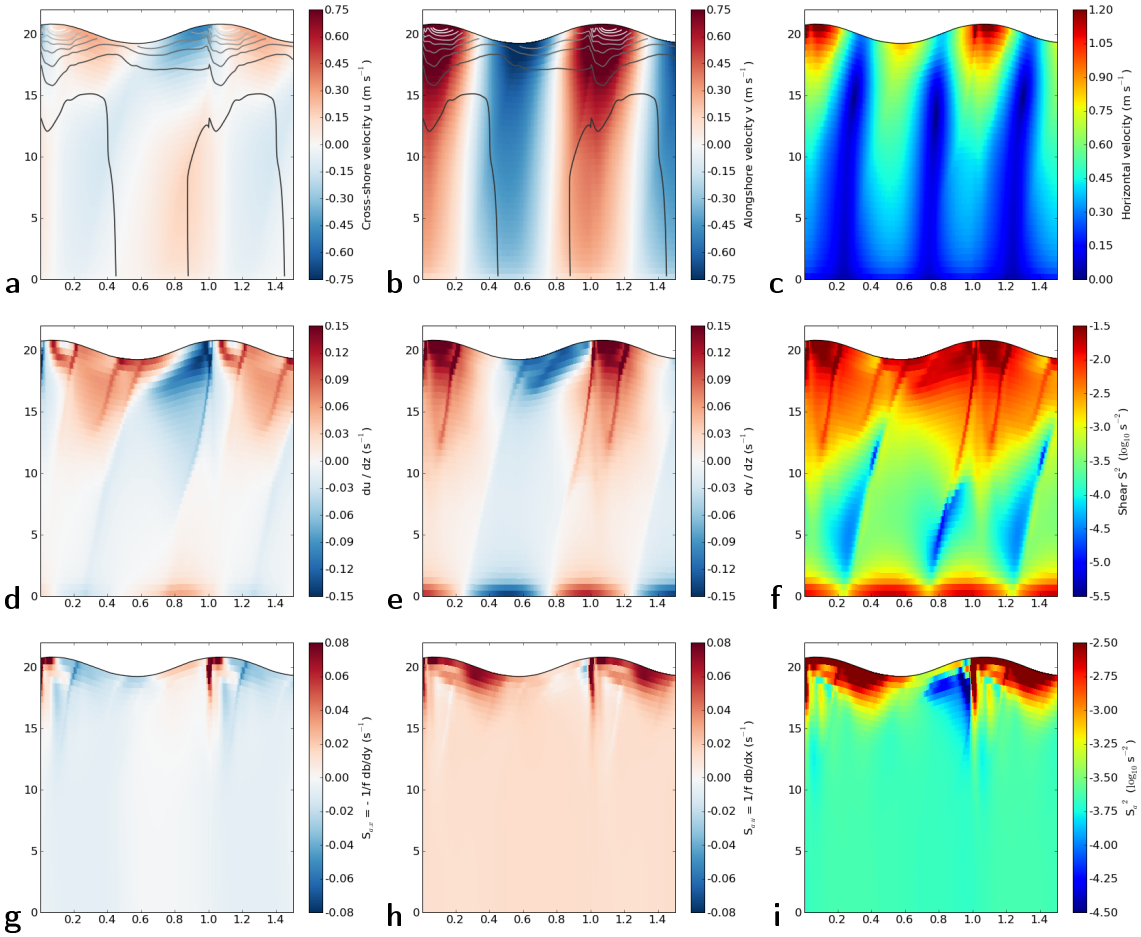


**Figure 5.7:** One and a half tidal cycles of velocities and shears in the LMC set-up (water column $14$ km offshore and $8$ km northeast of river mouth, x-axis $t/T$ and y-axis mab as in Fig. 5.5c). **a** cross-shore velocity, $u$, **b** alongshore velocity, $v$, both with isohalines ($1$ g/kg intervals, lowest is $30$ g/kg), **c** absolute horizontal velocity, $\sqrt{u^2+v^2}$, **d** cross-shore shear, $\mathrm{d}u/\mathrm{d}z$, **e** alongshore shear, $\mathrm{d}v/\mathrm{d}z$, **f** shear squared, $S^2 = (\mathrm{d}u/\mathrm{d}z)^2 + (\mathrm{d}v/\mathrm{d}z)^2$, **g** cross-shore thermal wind shear, $S_{\mathrm{g},x}$, **h** alongshore thermal wind shear, $S_{\mathrm{g},y}$, **i** thermal wind shear squared, $S_{\mathrm{g}}^2$ (see equation (5.3)).

(Fig. 5.7e), has maxima at the bottom at both high and low water, when bottom friction acts on the strong alongshore currents. These are responsible for the bottom maxima of $P$ and $\varepsilon$. At the surface, around high water, when the alongshore velocity is maximum (northeastward), $\mathrm{d}v/\mathrm{d}z$ is highest, too, and provides the main contribution to the high-water maximum of $S^2$. Around low water, the alongshore shear is maximum in the opposite direction (southwestward).
The cross-shore shear, i.e. the vertical gradient of the cross-shore velocity, $\mathrm{d}u/\mathrm{d}z$ (Fig. 5.7d), is generally weaker than $\mathrm{d}v/\mathrm{d}z$. Only the maxima around low water (southeastward) as well as the patch of strong cross-shore shear between low and high water (northeastward) significantly contribute to $S^2$.

As already described in section 5.5.3, the upper-layer isohalines (Fig. 5.7a, b) exhibit a peculiar pattern around high water, when shears are maximum. Therefore, the movement of the freshwater plume has to be considered.

#### 5.6.2.3 Plume Front Transition

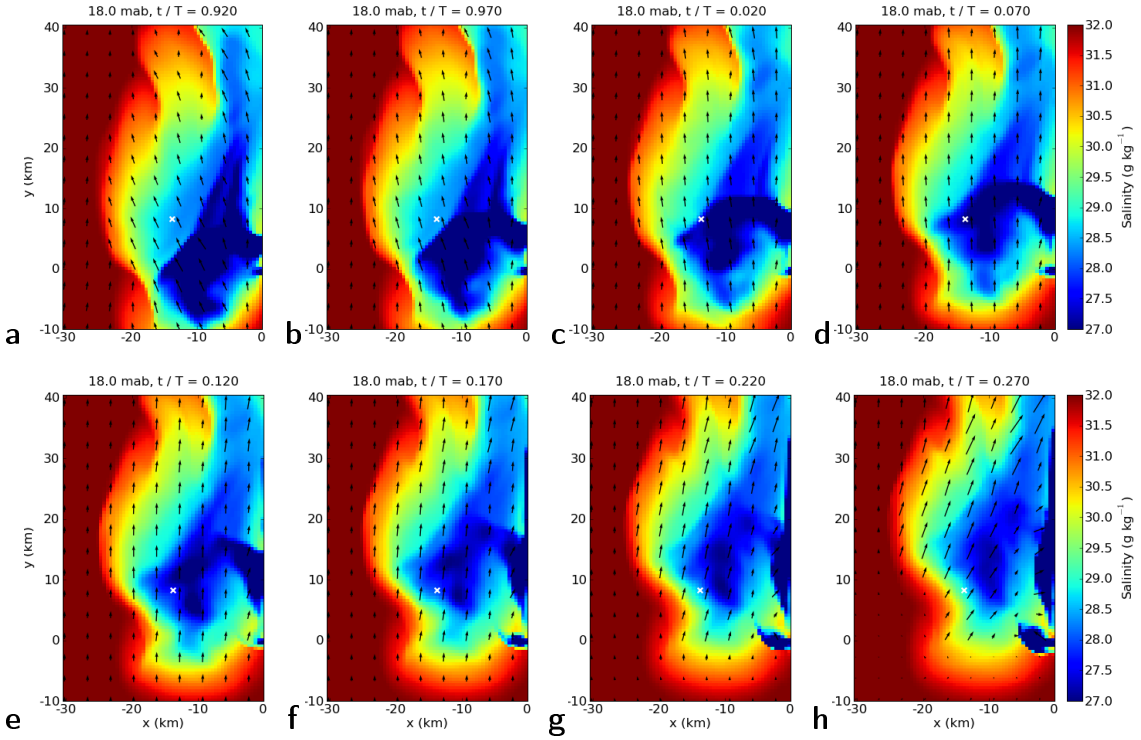


**Figure 5.8:** Plan views of salinity and horizontal velocity vectors in the LMC set-up at $18\ \mathrm{mab}$ from $1.9\ \mathrm{h}$ before to $2.4\ \mathrm{h}$ after high water ($\approx 4\ \mathrm{min}$ after **d**). The time interval between the views is $T/20$ ($\approx 37.3\ \mathrm{min}$); $t/T = 1$ is equivalent to $t/T = 0$.

In the $4$ hours around high water, the plume principally moves coast-parallel northeastward (Fig. 5.8a-g) so that a water column sufficiently close to the coast and the Rhine river mouth experiences two plume front transitions. The chosen water column is passed by the leading front of the plume (henceforth called the forefront) approximately half an hour before high water (Fig. 5.8c) and by the trailing front of the plume (henceforth called the back front) about two and a half hours later (Fig. 5.8g). The first front is more pronounced than the second one, i.e. horizontal and, since moving horizontally, temporal salinity gradients associated with it are stronger. This explains the sharp plunge of the isohalines before high water and their slower rise afterwards (Fig.s 5.5c; 5.7a, b). In the lower half of the water column, where the branches of high shear originate, salinity fluctuates between $29.5\ \mathrm{g/kg}$ around low water and $30.5\ \mathrm{g/kg}$ around high water. This fluctuation is driven by the cross-shore velocity, which points offshore between high and low water and onshore between low and high water (Fig. 5.7a).
The most rapid changes of salinity ($\mathrm{d}S/\mathrm{d}t$, Fig. 5.9) occur at the surface around high

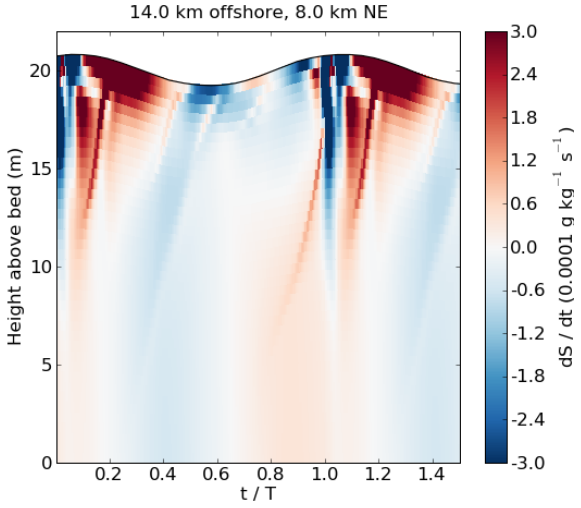


**Figure 5.9:** One and a half tidal cycles of the time derivative of salinity, $\mathrm{d}S/\mathrm{d}t$.

water, when the freshwater plume transits the water column. More interesting, however, are the two branches of increasing salinity (red colour) coinciding with high shears (Fig.s 5.7d, e, f). The first one is related to seawater driven onshore by the cross-shore velocity, as described above. Further upward, this movement is counteracted by the transition of the forefront of the plume, which leads to a drastic decrease of salinity. The second branch is generated by the back front of the plume.

#### 5.6.2.4 Thermal Wind

Since the horizontal gradients of salinity and, thus, density are very strong, vertical shear generated by thermal wind balance might be important. The thermal wind equations read as:

$$\begin{aligned} S_{\mathrm{g},x} &= \frac{\partial u_\mathrm{g}}{\partial z} = -\frac{1}{f}\frac{\partial b}{\partial y}\,, \; S_{\mathrm{g},y} = \frac{\partial v_\mathrm{g}}{\partial z} = \frac{1}{f}\frac{\partial b}{\partial x}\,, \\ S_\mathrm{g}^2 &= S_{\mathrm{g},x}^2 + S_{\mathrm{g},y}^2 = \frac{1}{f^2}\left[\left(\frac{\partial b}{\partial x}\right)^2 + \left(\frac{\partial b}{\partial x}\right)^2\right] \end{aligned} \tag{5.3}$$

with $S_\mathrm{g}$ the thermal wind shear (g for geostrophic), $f$ the Coriolis parameter and $b = -g(\varrho - \varrho_0)/\varrho_0$ the buoyancy ($g$ gravitational acceleration, $\varrho$ density, $\varrho_0$ reference density). The thermal wind shears are shown in the last row of Fig. 5.7. A comparison with the conventional shear (second row) does not lead to a satisfying explanation. Quite on the contrary, the cross-shore components point in the opposite directions (Fig. 5.7d versus g) and the alongshore thermal wind (Fig. 5.7h) is much smaller than the alongshore shear (Fig. 5.7e), especially with regard to the second high-water branch.

## 5.7 Conclusion

Three-dimensional numerical simulations including proper turbulence parameterisations provide a powerful tool for the investigation of physical processes in the coastal ocean. Even with idealised conditions, the measured turbulent kinetic energy dissipation rate in the Rhine region of freshwater influence is well reproduced.
In a water column located at the northwest edge of the plume, $\varepsilon$ has maxima at the bottom at both high and low water, which are related to tidal shear and which decrease with height. Furthermore, $\varepsilon$ exhibits two distinct peaks in the upper layer approximately half an hour before as well as two hours after high water.
The results of the simulations confirm that these peaks are neither caused by tidal shear production at the bottom, for $\varepsilon$, $P$ and $S^2$ increase from mid-depth to the surface; nor generated by convective instabilities, for stratification in the upper half of the water column is stable; nor related to meteorology, for they also occur in simulations without wind forcing.
It turns out that $\varepsilon \approx P$, i.e. that the turbulent kinetic energy dissipated here is shear-generated. The shear squared, $S^2$, is strongest at the surface and exhibits two distinct peaks coinciding with maximum $\varepsilon$ around high water. The northeastward alongshore shear provides the main contribution to these peaks, but also the northwestward cross-shore component shortly before high water is significant.
However, strong shear alone does not result in elevated turbulence as the patch between the two shear peaks reveals; stability, i.e. $N^2$, has to be relatively low at the same time, which leads to a gradient Richardson number, $Ri$, sufficiently small ($Ri_c = 0.25$) to allow for mixing due to shear instabilities. These conditions are fulfilled at the bottom, especially around high and low water, as well as in the upper layer half an hour before and two hours after high water.
At these times, the fore- and the back front of the freshwater plume transit the water column. The strong vertical salinity gradients associated with the plume give rise to elevated shear, $S^2$, and stability, $N^2$, but directly at the plume fronts, $S^2$ is much higher compared to $N^2$. The shear maxima cannot be explained by thermal wind due to the strong horizontal salinity gradients.
Field studies in the Liverpool Bay, in which straining is parallel to the main density gradients, have revealed dissipation maxima at the bottom at both high and low water as well as a local maximum of $\varepsilon$ in the upper half of the water column at the end of flood, i.e. shortly before high water (Rippeth et al., 2001). Burchard (2008) has confirmed this by numerical simulations.
In order to fully understand the phenomenon, further investigations are required. Specifically, further detailed field studies including turbulence measurements are needed in the Rhine ROFI.

**Acknowledgements** This work has been supported by the EU-funded project ECOOP (European COastal sea OPerational observing and forecasting system, Contract No. 36355).
The authors are grateful to Alejandro Souza (Liverpool, UK) for providing the measurement data (Fig. 5.2) and support in data analysis, to Gerben de Boer (Delft, The Netherlands) for

delivering the grid data as well as to Lars Umlauf (Warnemünde, Germany) for helpful discussions.
Furthermore, the first author wishes to thank Eefke van der Lee (Warnemünde, Germany) for assistance with MATLAB and for proofreading as well as *The Challenger Society for Marine Science* for granting her a Student Travel Award to the PECS (Physics of Estuaries and Coastal Seas) conference 2008 in Liverpool, where first results of this work were presented.


# Chapter 6

# Further Findings

In this chapter, further results of the LMC simulation ($1,500\ \mathrm{m^3/s}$ discharge, $2\ \mathrm{m}$ tidal range, no wind) are presented and compared to literature data (chapter 2). A different view of the salinity and the turbulent kinetic energy dissipation rate follows in the sections 6.3 and 6.4.

## 6.1 Classification of the Rhine River Plume

In the sections 2.2 and 2.4, five possible classification schemes of river plumes have been introduced and applied to the Rhine plume according to literature data. The following specification of the Rhine plume is based on the model results (LMC set-up unless otherwise noted).

(Open coast: Neither the *Maasvlakte* island southwest nor the breakwater northeast of the New Waterway are implemented in the model; the coastline is straight.)

Outflow geometry and recirculating bulge: In the model, the bay exit angle is $\theta = 90°$ and the radius of curvature is $r_c = 0$. The formation of a recirculating bulge is expected, but not directly visible due to the tidal currents. However, averaging of the horizontal currents over a full tidal cycle results in a velocity field clearly exhibiting recirculation (Fig. 6.1(a)). Though, in the LMW set-up (southwest wind with a wind stress of $0.125\ \mathrm{Pa}$), no recirculation occurs, but a northeastward coastal current develops already $2\ \mathrm{km}$ northeast of the river mouth (Fig. 6.1(b)).

Kelvin number greater than one: The plume's width and thickness are $W = 20\ \mathrm{km}$ and $H_p = 5\ \mathrm{m}$ (cp. sec. 5.5.1, Fig.s 5.4b, c); the water column below the plume spans $H_a = 15\ \mathrm{m}$. The density of the ambient water is $\rho_a = 1,025\ \mathrm{kg/m^3}$. The density of the plume varies with distance from the river mouth; at the surface and near the centre of the recirculating bulge, it is about $\rho_p = 1,015\ \mathrm{kg/m^3}$ (Fig. 6.1(a)). This yields an internal Rossby radius $R_1 = 5.4\ \mathrm{km}$ and a Kelvin number $K = 3.67 > 1$, which is in good agreement with the literature. The Coriolis force influences the freshwater outflow and causes both a recirculation and

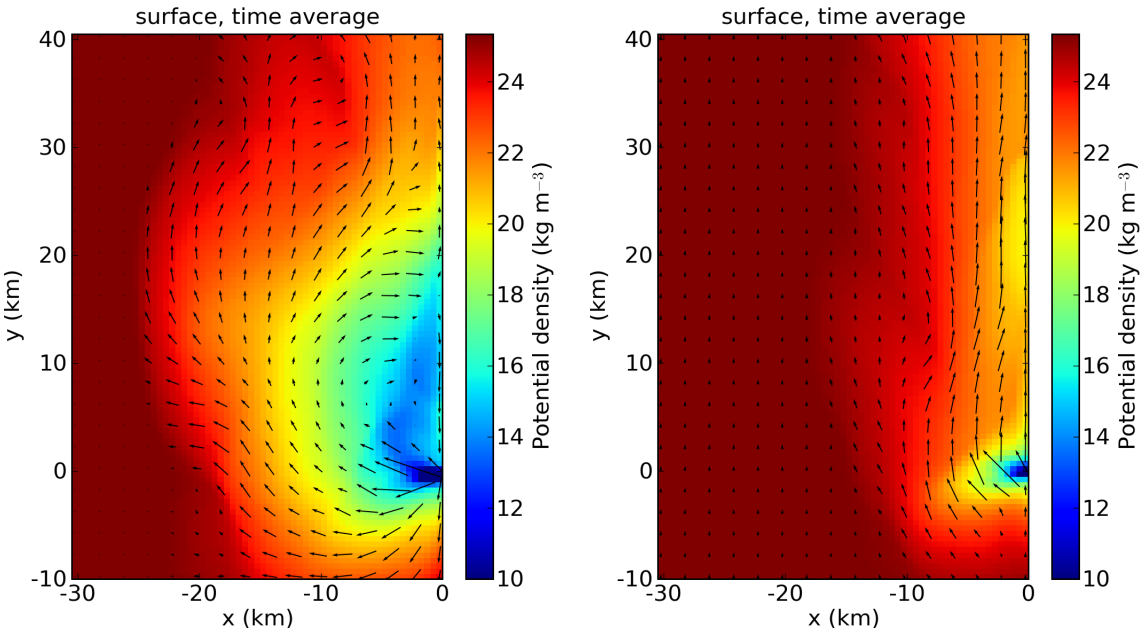


(a) LMC set-up. A recirculating bulge is formed, the surface centre of which is located approximately $4$ km offshore and $6$ km northeast of the Rhine river mouth.

(b) LMW set-up. The plume is much narrower and the surface density is higher. No recirculation bulge forms, but the currents' alongshore component points northeastward everywhere.

**Figure 6.1:** Plan view of the modelled potential density ($\sigma_t = \rho - 1,000\ \mathrm{kg/m^3}$) and horizontal velocity vectors at the surface averaged over one tidal cycle.

a narrow coastal current, but wind can exert significant effects, too (Fig. 6.1(b); cp. LMW set-up in sec. 5.5.1).

Intermediate case between bottom- and surface-advected plume: As shown in Fig. 5.4, the Rhine plume is partly bottom- and partly surface-advected. The isohalines are vertical in the lower half of the water column and bend offshore above. In the upper layer, there is a distinct stratification with horizontal isohalines in the centre of the plume (Fig. 5.4c). With increasing northeastward distance from the river mouth, tidal stirring mixes the less saline water down; the plume attaches to the bottom (Fig. 5.4d).
It should again be noted that this and the above classifications have been introduced neglecting tides. Without tidal forcing, the Rhine plume would presumably be plainly surface-advected.

Non-pulsed discharge and plume: The surface salinity (Fig. 6.2) does not reveal a pulsed plume. Viewing the horizontal currents (Fig.s 6.2, 6.3) leads to the conclusion that the outflow velocity of the river exceeds the tidal current's onshore component at any time; i.e. the pinching-off criterion is not fulfilled. A smaller river discharge might fulfil this criterion, but still, the ambient currents and the recirculation are likely to mix successive pulses as indicated in the last row of Fig. 6.2: The freshwater does be pulled apart slightly, but is reunified shortly thereafter. Only the

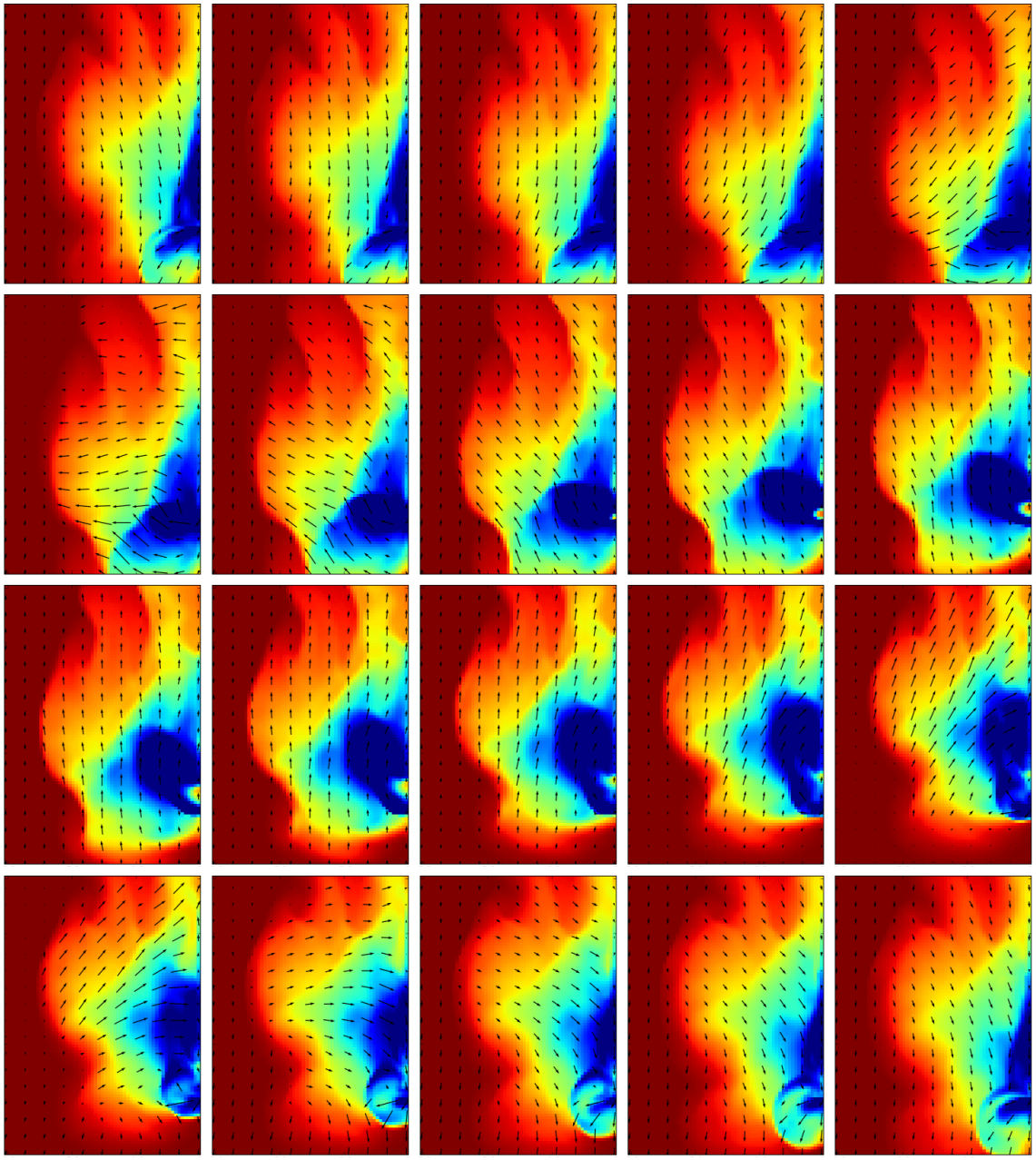

**Figure 6.2:** One tidal cycle of the salinity and the horizontal velocity vectors at the surface in the LMC set-up. The first plan view depicts the situation $4\ \mathrm{min}$ before low water; the time interval between the views is $T/20 \approx 37.3\ \mathrm{min}$. The axes are the same as in Fig. 5.8; the colour scale ranges from $17$ (blue) to $32\ \mathrm{g/kg}$ (red). (They are omitted for lack of space since they are not needed for the qualitative understanding of the figure.)
Around LW, currents are directed coast-parallel southwestward (downward in figure); the plume is forced in the corresponding direction. With increasing surface elevation, the currents turn clockwise to point offshore between LW and HW; the plume is removed from the coast. Around HW, the currents are strongest in the northeastward direction (upward in figure) and elongate the plume. With decreasing surface elevation, they turn further and point onshore between HW and LW; the plume is pressed against the coast. Since the river discharge is too strong to be withheld, the outflow continues, but the opposing tidal currents drive a wedge of more saline water between the plume and the subsequently discharged freshwater. However, the southwestward currents of the next LW bring the two parts together again.

"cockscomb" structure of the outer plume edge indicates an incomplete merging. Indeed, this structure is much more distinct and regular in the LMW set-up, which does generate a pulsed plume (Fig. 6.4). Though, the pinching-off criterion is not fulfilled in the way shown in Fig. 2.5 (sec. 2.2.5, an onshore/upstream tidal current opposing the downstream river discharge), but in the alongshore direction: The northeastward tidal current velocity is higher than the discharge velocity, so that the plume detaches from the subsequently discharging freshwater. The absence of a recirculating bulge in the LMW set-up (Fig. 6.1(b)) leads to the reasonable assumption that a distinct recirculation (Fig. 6.1(a)) strongly counteracts a pulsed plume.

Please note that the outflow (Fig. 6.3(a)) is minimum not between high and low water when you expect the rotary surface current to point onshore, but between low and high water. This is due to the fact that, in the narrow estuary, the surface tidal current is not rotary but reversing with the principal axis parallel to the river, i.e. perpendicular to the coastline. Thus, maximum upstream tidal currents occur between low and high water and maximum downstream tidal currents occur between high and low water (cp. sec. 2.5.5, Tab. 2.2, Fig. 2.14).

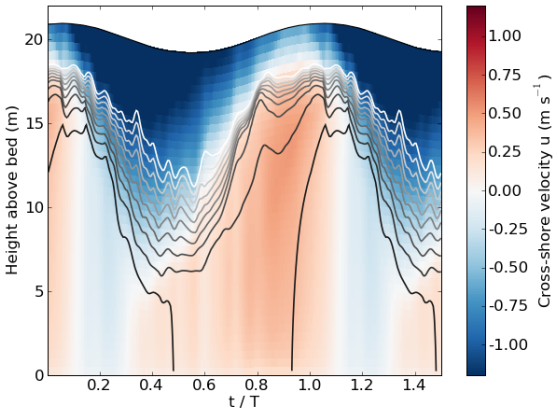


(a) The cross-shore velocity in the upper layer always points offshore. In the lower part of the water column, it is smaller and points onshore except for a short period after high water.

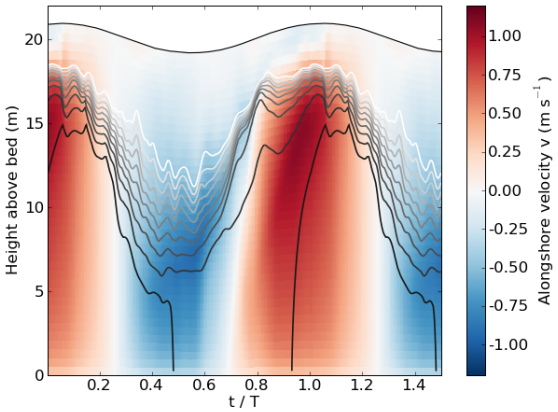


(b) The alongshore velocity in the upper layer is small compared to the lower layer or to the cross-shore velocity. In the lower part of the water column, it is in phase with the sea surface elevation.

**Figure 6.3:** One and a half tidal cycles of the horizontal velocity components and isohalines in the water column directly in front of the river mouth. The lowest (black) isohaline represents $31$, the highest (white) $22$ g/kg.
The plume is thickest around low and thinnest around high water. In the upper layer, the current is reversing with the principal axis parallel to the estuary; in the lower part of the water column, it is rotary with the principal axis parallel to the coastline and a counterclockwise sense of rotation.

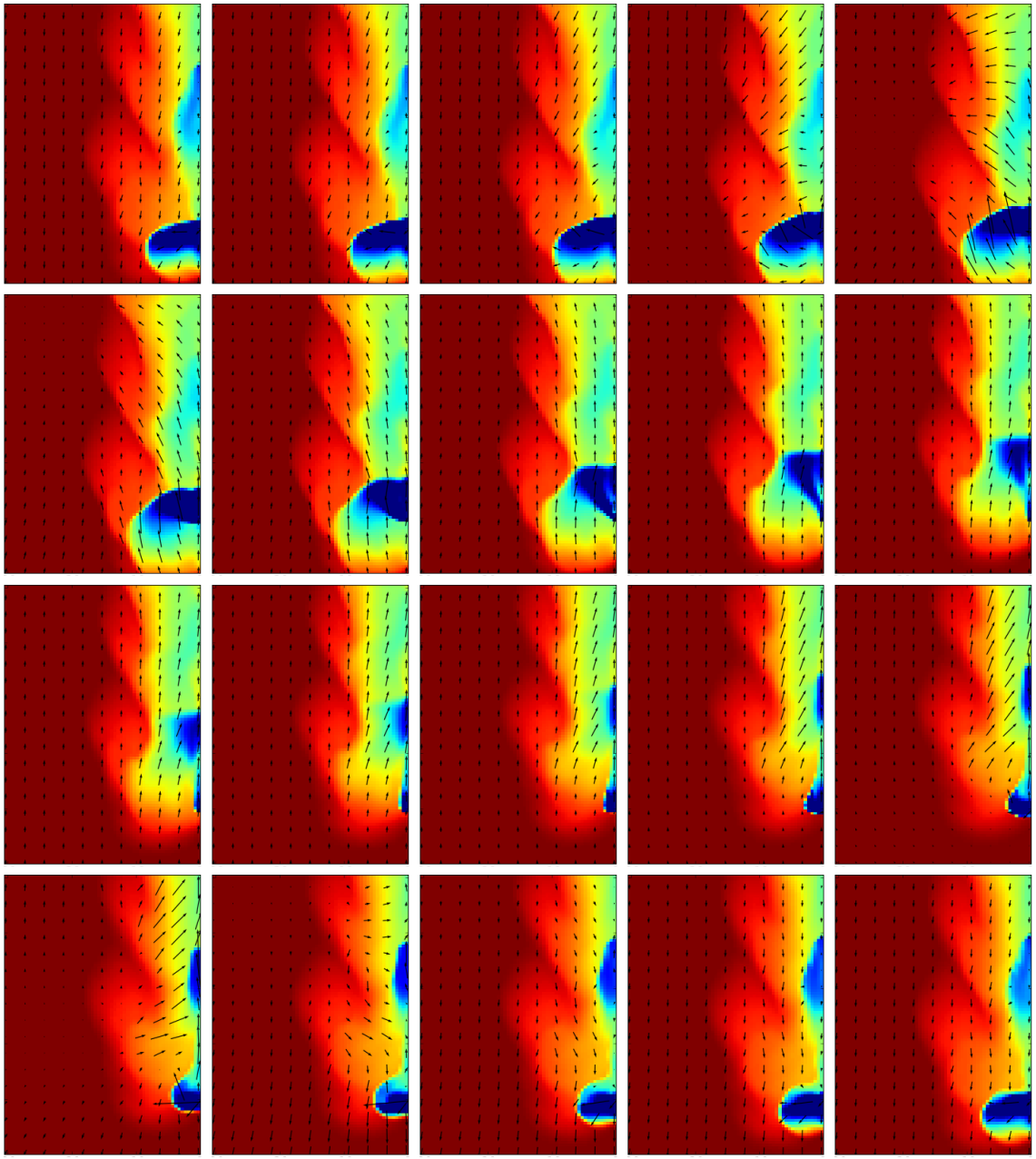

**Figure 6.4:** Same as Fig. 6.2, but in the LMW set-up and with the colour scale ranging from 22 (blue) to 32 g/kg (red).
Due to the southwest wind, the coast-parallel southwestward currents around LW are weaker than in the LMC set-up. The clockwise turning takes place faster, i.e. the period of offshore-pointing currents is shorter, so that the plume is hardly removed from the coast. Around HW, the northeastward currents are enhanced by the wind; the plume seems to be moved away from the river mouth with a velocity higher than the discharge velocity (another type of pinching-off criterion); two individual pulses are created. The subsequent onshore currents force more saline water between the pulses and let them separate so far that they are not brought together again by the southwestward currents of the next LW. However, the wind stirring is too strong to allow a life time exceeding one tidal cycle.

## 6.2 Modelled Residual Currents

The residual currents in the Rhine ROFI have been introduced in section 2.5.2; the range of the depth-averaged residual has been stated as $3$ to $8\ \mathrm{cm/s}$ (van Alphen et al., 1988), the range of the surface residual as $15$ to $20\ \mathrm{cm/s}$ (Simpson et al., 1993). In section 2.5.3, a maximum surface velocity of $0.8\ \mathrm{m/s}$ ($1.1\ \mathrm{m/s}$) has been assigned to the northeastward flood current and $0.7\ \mathrm{m/s}$ ($0.9\ \mathrm{m/s}$) to the southwestward ebb current at neap (spring) tides (van Alphen et al., 1988). The model basically reproduces these velocities, but seems to underestimate the residuals.

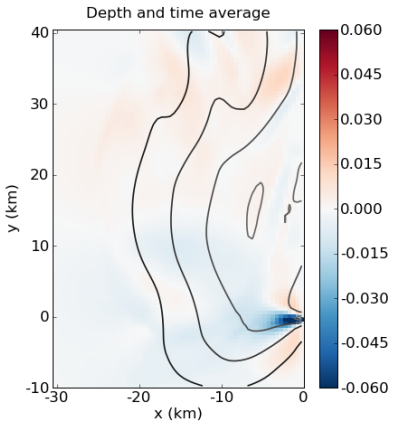


(a) Plan view of the depth-averaged residual cross-shore velocity.

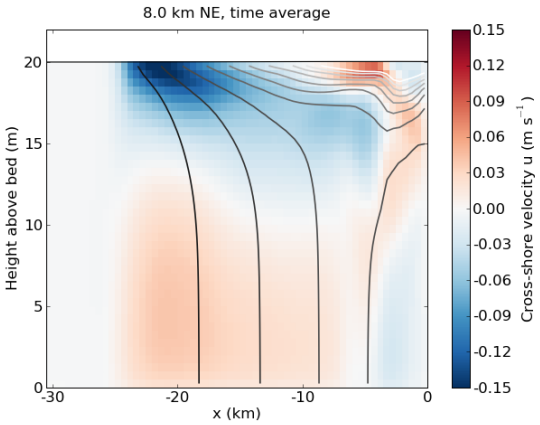


(b) Residual cross-shore velocity at a cross-section $8\ \mathrm{km}$ northeast of the river mouth.

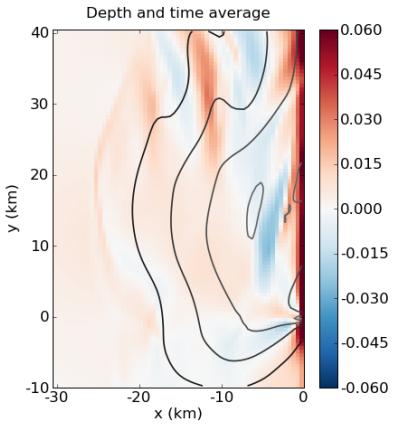


(c) Plan view of the depth-averaged residual alongshore velocity.

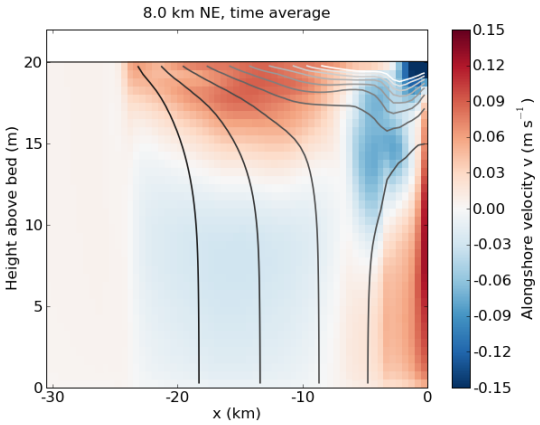


(d) Residual alongshore velocity at a cross-section $8\ \mathrm{km}$ northeast of the river mouth.

**Figure 6.5:** Plan views and cross-sections of the modelled residual velocity components and isohalines.

The depth-averaged residual current (Fig.s 6.5(a), (c)) strongly varies with both cross-shore and alongshore distance from the river mouth. A clockwise recirculation is recognisable, the centre of which is located approximately $7\ \mathrm{km}$ offshore and $13\ \mathrm{km}$ northeast of the Rhine river mouth (also cp. Fig. 6.1(a)). The strong, only $2\ \mathrm{km}$ wide, coast-parallel current in the northeastward direction is brought about by the alongshore component

below the plume (Fig. 6.5(d)). $20\ \mathrm{km}$ and farther away from the coast, where horizontal variations diminish, the depth-averaged residual velocity is approximately $1\ \mathrm{cm/s}$ northeastward.
Fig.s 6.5(b) and (d) show a cross-section of the residual velocity components and the isohalines close to the centre of the plume (cp. Fig. 6.1(a)). Water columns beyond approximately $24\ \mathrm{km}$ offshore are vertically homogeneous (salinity $32\ \mathrm{g/kg}$); the residual current flows northeastward and does not exceed $1\ \mathrm{cm/s}$ (see above). From $24$ to $8\ \mathrm{km}$ offshore, salinity decreases and stratification increases. There are two horizontal layers with opposing current directions: Between the bottom and $12$ to $15\ \mathrm{mab}$, the current points southward with about $5\ \mathrm{cm/s}$; in the upper layer, it points northwest- to northeastward with $18$ to $8\ \mathrm{cm/s}$.
A temporal evolution of velocities is shown in Fig. 6.6. In this specific water column, maximum surface velocities are $1.0\ \mathrm{m/s}$ for the northeastward flood current and $0.8\ \mathrm{m/s}$ for the southwestward ebb current, but the spatial variability is very high (cp. e.g. Fig.s 5.7a, b; 6.3).

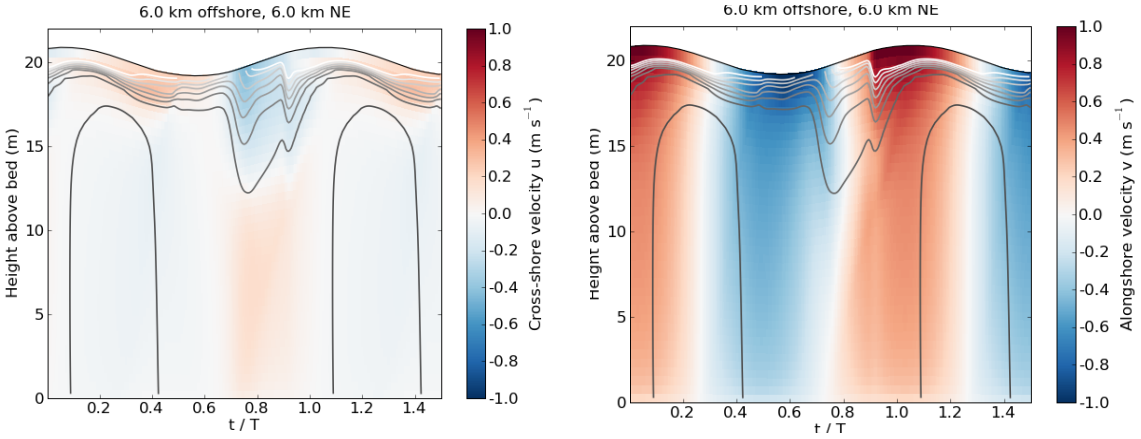


(a) The cross-shore velocity exhibits a phase shift of $180°$ between surface and bottom and of $\pm 90°$ with respect to the sea surface elevation.

(b) The alongshore velocity is in phase with the sea surface elevation and increases from bottom to surface.

**Figure 6.6:** One and a half tidal cycles of the horizontal velocity components and isohalines $6\ \mathrm{km}$ offshore and $6\ \mathrm{km}$ northeast of the river mouth. The lowest (black) isohaline represents $28$, the highest (white) $22\ \mathrm{g/kg}$.
The surface current rotates clockwise, the bottom current counterclockwise. Both ellipses' major axes lie approximately coast-parallel.

## 6.3 Interaction of Tidal Current Ellipses and Stratification

In the sections 2.5.5 and 2.5.6, the interaction between tidal current ellipses and stratification has been explained. In order to allow a better visualisation of the relationships,

a new point of view is introduced in Fig. 6.7 (based on an idea from Robert D. Hetland, College Station, Texas, USA); for convenience, it will henceforth be called the ellipse view.

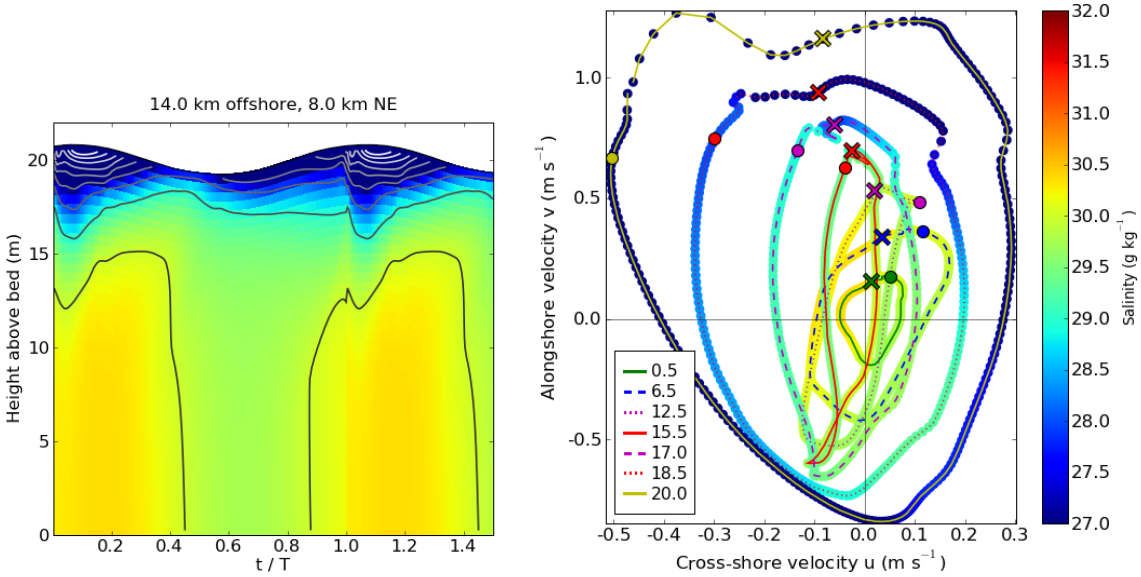


(a) Common view in a $t$-$z$ diagram (same colour scale as in (b)).

(b) Current ellipse view in a $u$-$v$ diagram. (The legend's unit is $\mathrm{mab}$.)

**Figure 6.7:** Different views of the salinity. Instead of colour-coded $t$-$z$ diagrams of velocity and salinity (Fig.s 5.7a, b; (a)), the salinity at a certain height can be treated as a function of $u$ and $v$. It can thus be represented by colour-coded markers along the current ellipse in a $u$-$v$ diagram (b).
The shown ellipses are traced out the long way from $\times$ ($15\ \mathrm{min}$ before HW) to $\bullet$; the time interval between the salinity circles is $T/200 \approx 3.7\ \mathrm{min}$.

The maybe more plain part of the interaction is the process of tidal straining. Let the tidal current ellipses be taken for granted with the following properties: Surface ellipses exhibit a clockwise, bottom ellipses a counterclockwise sense of rotation; their major axes lie coast-parallel and coincide with high water (northeastward) and low water (southwestward currents). Consequently, surface currents point onshore between HW and LW and offshore between LW and HW and for the bottom currents it is the other way around. The resulting shear interacts with the horizontal density gradient, which is strongest in the cross-shore direction (density increases with distance from the coast): Between HW and LW, stratification is established; between LW and HW, it is diminished or even destroyed (cp. Fig. 2.19). For the ellipse view of salinity, this means less surface salinity and higher bottom salinity around HW and higher surface salinity and less bottom salinity around LW as is evident in Fig. 6.8 in the water column $5\ \mathrm{km}$ offshore and $30\ \mathrm{km}$ northeast of the river mouth, by way of example.
The other part of the interaction is the influence of stratification on the ellipticity (see Fig. 2.17, app. A.3). This is also reproduced by the model (Fig. 6.8): The current structure in the stratified plume region (approx. $0$ to $20\ \mathrm{km}$ offshore, $-10$ to $60\ \mathrm{km}$

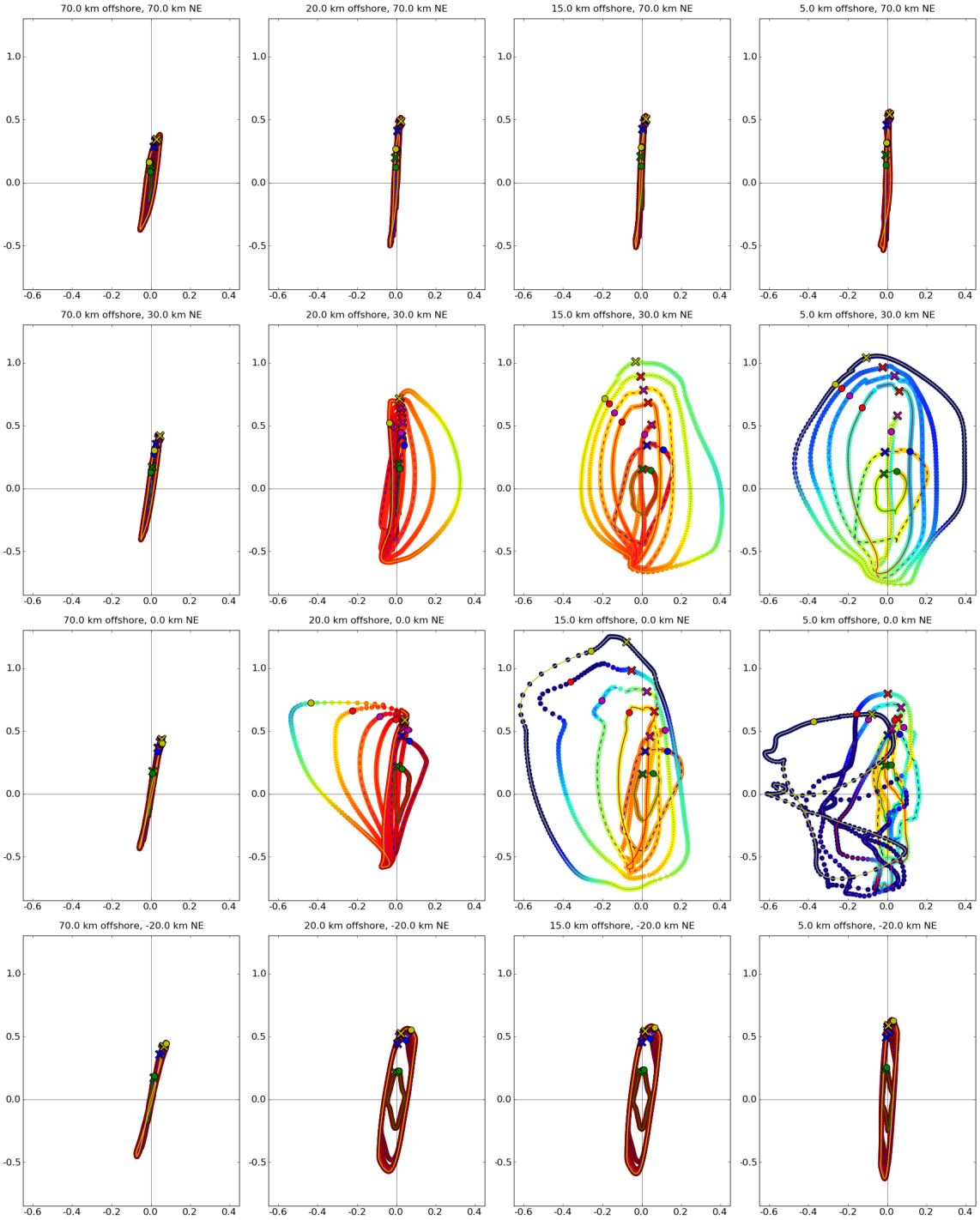


**Figure 6.8:** Ellipse view of the modelled salinity in 16 water columns spread over the model domain. For axes labels, the colour scale and the legend, refer to Fig. 6.7(b). Please mind the different scales in the offshore ($x$) and the northeastward ($y$) direction.
In front of the river mouth ($5$ km offshore, $0$ km northeast), the surface currents are influenced by the river discharge, so that the ellipses are distorted. See text for a general description.

northeast of the river mouth) is clearly recognisable as ellipses. Within $15\ \mathrm{km}$ offshore, the surface ellipticity is about $-0.4$ (clockwise, also see app. A.2), which is in good agreement with Fig. 2.16, and the bottom ellipses exhibit counterclockwise rotation. With increasing distance from the river mouth and, thus, decreasing stratification, the current ellipses become more and more degenerate; both surface and bottom currents are nearly rectilinear. (Farther than $80\ \mathrm{km}$ offshore, the ellipticity decreases from $0$ to approximately $-0.4$, i.e. clockwise rotation is assumed (Fig. 6.9). However, it should be noted that, in reality, these water columns are affected by the English coast, which is totally neglected in the model.) Southwest of the river mouth (last row of Fig. 6.8), the currents rotate counterclockwise (weak positive ellipticity) from bottom to surface (cp. Fig. 2.15).
Besides the ellipticity, also the current speed behaves as expected: It increases from the bottom to the surface and the residual is much weaker outside the ROFI (sec. 2.5.2; Simpson et al., 1993). Furthermore, a veering is visible in the stratified area, especially at $15/0$, $15/30$ and $5/30$ ($\mathrm{km}$ offshore/$\mathrm{km}$ northeast) of Fig. 6.8: The bottom ellipses veer clockwise, the surface ellipses slightly counterclockwise, which is in accordance with the result of the two-layer model (Fig. A.3). However, Visser et al. (1994) reported the bottom ellipse to be aligned in counterclockwise sense with respect to the coastline and the surface ellipse, i.e. in the opposite direction.

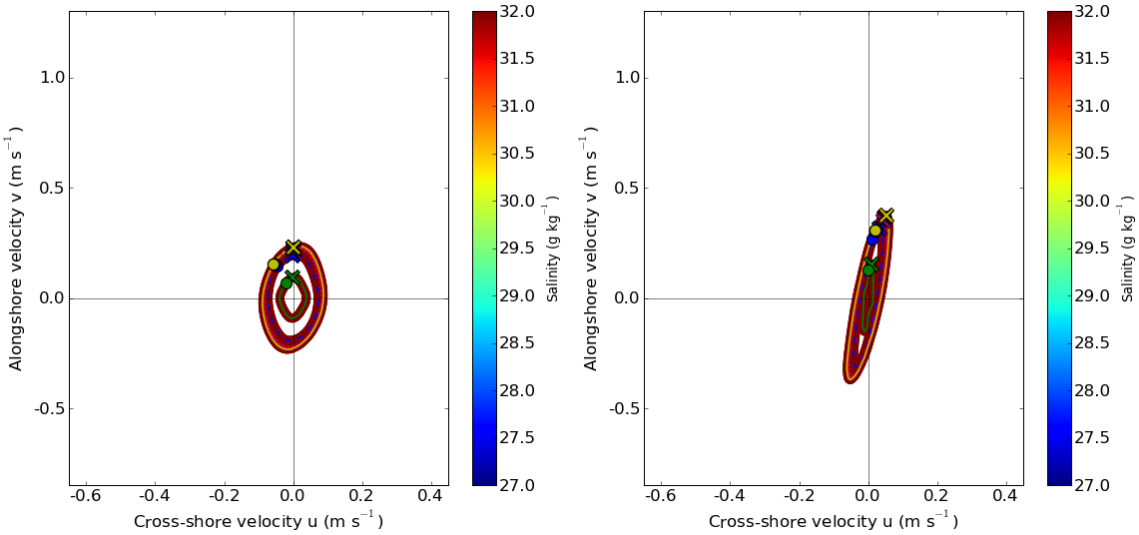


**Figure 6.9:** Ellipse view of the modelled salinity $234\ \mathrm{km}$ and $106\ \mathrm{km}$ offshore (both $8\ \mathrm{km}$ northeast of the river mouth). The legend of Fig. 6.7(b) applies.
The salinity is $32\ \mathrm{g/kg}$ (initial value) from the bottom to the surface. The current ellipses exhibit a clockwise sense of rotation; the ellipticity approaches $-1$ with increasing distance from the coast.

## 6.4 TKE Dissipation Rate Associated with the Tidal Current Ellipse

The ellipse view can, of course, be applied to any variable, including the turbulent kinetic energy dissipation rate, $\varepsilon$ (Fig. 6.10). This simplifies the recognition of relationships between the current direction and velocity on the one hand and the dissipation maxima on the other hand. Remarkably, especially the upper three current ellipses (17, 18.5 and 20 mab) exhibit distinct bends or rather double bends at the times of maximum $\varepsilon$. These involve a strong velocity shear (Fig. 5.7d, e, f) and, consequently, a high shear production of turbulent kinetic energy (Fig. 5.6a) and a high dissipation rate.

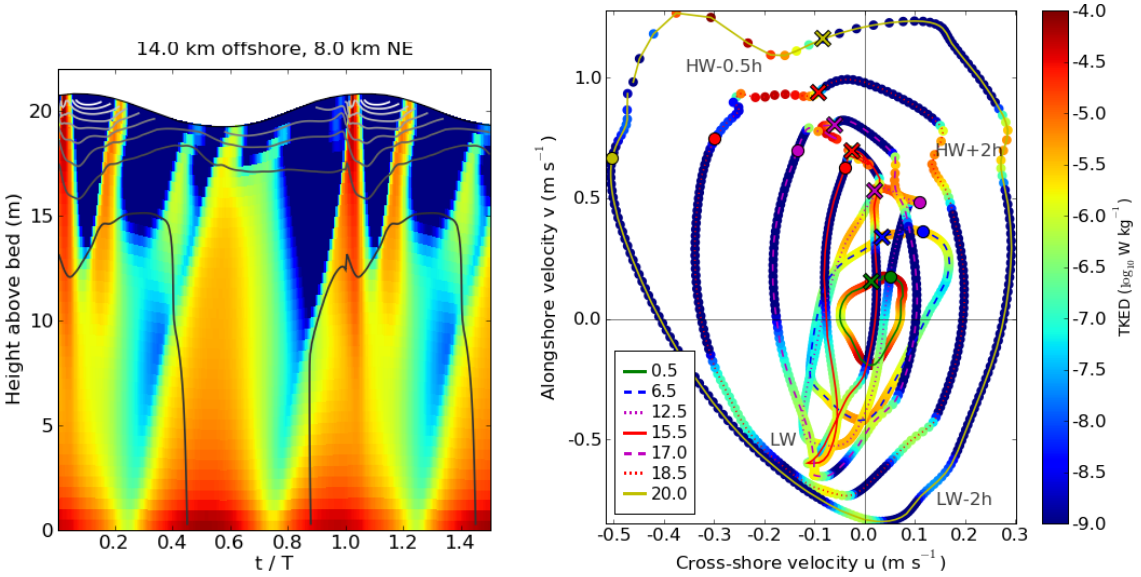


(a) Common view in a $t$-$z$ diagram (same colour scale as in (b)).

(b) Current ellipse view in a $u$-$v$ diagram. (The legend's unit is mab.)

**Figure 6.10:** Different views of $\varepsilon$ (cp. caption of Fig. 6.7). See text for description.

## 6.5 Conclusion

The model well reproduces the investigated properties. The Rhine plume behaves as expected regarding both general derivations (sec. 2.2) and specific literature data (sec. 2.4). Only concerning the pulsing of the discharge and the plume, the model results do not agree with the statements of de Ruijter et al. (1997). Particularly, a higher discharge in the model does not lead to a train of freshwater lenses as argued by de Ruijter et al. (1997), but has the opposite effect, namely an even more compact plume (without figure). However, wind has the mentioned impact and does cause a pulsed plume.
The modelled residual currents are slightly smaller than those given in the literature, but this is probably due to the wind. Wind is not included in the model (LMC set-up), but

represents a significant driving mechanism of the Dutch coastal current (e.g. van Alphen et al., 1988). Furthermore, the literature mostly refers to long-term means, so that it is not remarkable if a model forced by specific conditions is not fully representative.
The current ellipses and their relationship to the stratification are clearly shown. The process of tidal straining induces a semi-diurnal cycle of stratification (SIPS) in the ROFI; the influence of stratification on the ellipticity is evident even though a wide-ranging consideration is not possible due to the zooming out of the model grid into regions which are, in reality, close to the English coast or even land.
Further work on the analytical model (app. A.3) is intended. More investigations could also be focussed on the LMW (wind), the LSC (spring tide) and the HMC (higher discharge) set-up, which have hardly been utilised to gain additional results.

# Part III

# Closing Information

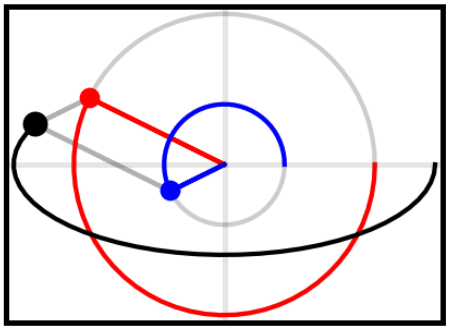

# Appendix A

# Calculations

## A.1 Equations of Motion for a Kelvin Wave [1]

The linearised inviscid shallow water equations read as (see e.g. Kundu and Cohen, 2002)

$$\begin{aligned} u_t - fv &= -g\eta_x \\ v_t + fu &= -g\eta_y \\ \eta_t &= -H \cdot (u_x + v_y) \end{aligned} \tag{A.1}$$

with $\eta$ the sea surface elevation, $t$ the time, $H$ the mean water depth, $u$ and $v$ the velocities in $x$- and $y$-direction, respectively, $f$ the Coriolis parameter and $g$ the gravitational acceleration. For shortening, subscripts represent derivatives, e.g. $\eta_t = \partial\eta/\partial t$.

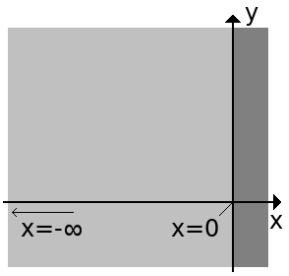


**Figure A.1:** Coordinate system applying to the Kelvin-wave solution at hand. The coast is aligned with the $y$-axis; dark shading represents land ($x > 0$), light shading represents the sea ($x < 0$).

Let the coast be aligned with the $y$-axis (Fig. A.1) and let us assume that a solution with $u = 0$ exists, i.e. that the vertically averaged cross-shore velocity is zero, and equations

[1] appendix to the sections 2.5.4 and 4.2

(A.1) reduce to

$$\begin{aligned} fv &= g\eta_x \\ v_t &= -g\eta_y \\ \eta_t &= -Hv_y \ . \end{aligned} \tag{A.2}$$

The boundary conditions associated with a Kelvin wave are the following:

$$\begin{aligned} \text{decay with distance from the coast:} \quad & \eta(-\infty, y, t) = 0 \\ \text{periodicity along the coast:} \quad & \eta(x, y+\lambda, t) = \eta(x, y, t) \\ \text{periodicity in time:} \quad & \eta(x, y, t+T) = \eta(x, y, t) \end{aligned} \tag{A.3}$$

with $\lambda = 2\pi/k$ the wave length ($k$ wave number) and $T = 2\pi/\omega$ the tidal period ($\omega$ angular frequency). These coincide with the ansatz

$$\{v(x,y,t),\ \eta(x,y,t)\} \ = \ \{\hat{v}(x),\ \hat{\eta}(x)\}\ \exp(\mathrm{i}[ky - \omega t]) \ . \tag{A.4}$$

Inserting this in the equations (A.2) and dividing by $\exp(\mathrm{i}[ky - \omega t])$ gives

$$\begin{aligned} f\hat{v} &= g\hat{\eta}_x \implies \hat{v} = g/f \cdot \hat{\eta}_x \\ \mathrm{i}\omega\hat{v} &= g\mathrm{i}k\hat{\eta} \implies \hat{v} = gk/\omega \cdot \hat{\eta} \\ \mathrm{i}\omega\hat{\eta} &= H\mathrm{i}k\hat{v} \implies \hat{v} = \omega/(kH) \cdot \hat{\eta} \ . \end{aligned} \tag{A.5}$$

Equating the last two of these equations and considering only non-trivial solutions leads to the dispersion relation of shallow water waves:

$$\left(\frac{\omega}{kH} - \frac{gk}{\omega}\right)\hat{\eta} \ = \ 0 \implies \omega^2 - gHk^2 \ = \ 0 \implies \omega = \pm k\sqrt{gH} \tag{A.6}$$

Consequently, the phase speed $c = |\omega/k| = \sqrt{gH}$ is non-dispersive, i.e. it does not depend on $k$.
With that, the last two equations of (A.5) become $\hat{v} = \pm\sqrt{g/H} \cdot \hat{\eta}$, which can be equated to the first equation:

$$\frac{g}{f}\hat{\eta}_x \ = \ \pm\sqrt{\frac{g}{H}}\hat{\eta} \implies \hat{\eta}_x \ = \ \pm\frac{f}{c}\hat{\eta} \tag{A.7}$$

The boundary condition of the decay with distance from the coast (first equation of (A.3)) requires

$$\hat{\eta} \ = \ a\ \exp\left(+\frac{f}{c}x\right) \tag{A.8}$$

($a$ amplitude at coast) and thus the final solution for the velocity and the sea surface elevation of a Kelvin wave is (considering the real part only) (cp. Kundu and Cohen,

2002)

$$\begin{aligned} u &= 0 \\ v &= a\sqrt{\frac{g}{H}}\,\exp\left(f\frac{x}{c}\right)\,\cos(ky-\omega t) \\ \eta &= a\,\exp\left(f\frac{x}{c}\right)\,\cos(ky-\omega t)\ . \end{aligned} \tag{A.9}$$

Obviously, $v$ and $\eta$ are in phase. Note that the $u$ and $v$ equations of (A.9) describe depth-averages. For a differentiation into two layers, see appendix A.3.

## A.2 Counter-Rotating Phasors and Ellipse Construction [2]

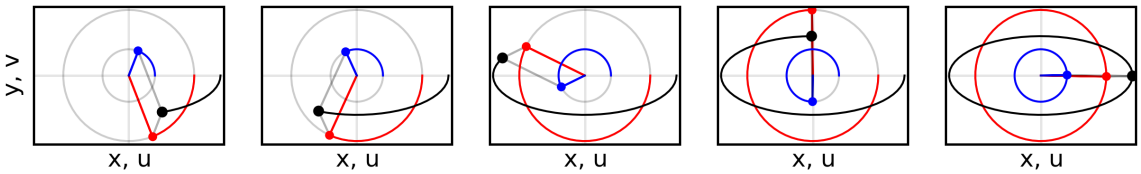


**Figure A.2:** Construction of an ellipse as the sum of two counter-rotating phasors with equal angular frequencies (inspired by `http://www.cut-the-knot.org/Curriculum/Geometry/DynoEllipse.shtml`).

Two counter-rotating phasors with constant lengths, $r_{1,2} \geq 0$, angular frequencies, $\omega_{1,2}$, and phase shifts, $\varphi_{1,2}$, can be expressed by the following equations:

$$\underline{p}_1(t) = \begin{pmatrix} x_{p_1} \\ y_{p_1} \end{pmatrix} = r_1 \cdot \begin{pmatrix} \cos(\omega_1 t + \varphi_1) \\ \sin(\omega_1 t + \varphi_1) \end{pmatrix} \tag{A.10}$$

$$\underline{p}_2(t) = \begin{pmatrix} x_{p_2} \\ y_{p_2} \end{pmatrix} = r_2 \cdot \begin{pmatrix} \cos(-\omega_2 t + \varphi_2) \\ \sin(-\omega_2 t + \varphi_2) \end{pmatrix} \tag{A.11}$$

For an ellipse, the angular frequencies have to be equal, $\omega_1 = \omega_2 = \omega$. If $\omega > 0$, $\underline{p}_1(t)$ rotates counterclockwise and $\underline{p}_2(t)$ rotates clockwise around the origin. Consequently, there is a time $t_0$ at which they meet and overlap, $\omega t_0 + \varphi_1 = -\omega t_0 + \varphi_2 = \vartheta$, so that shifting from $t$ to $t + t_0$ leads to

$$\underline{p}_1(t) = r_1 \cdot \begin{pmatrix} \cos(\omega t + \vartheta) \\ \sin(\omega t + \vartheta) \end{pmatrix} \tag{A.12}$$

$$\underline{p}_2(t) = r_2 \cdot \begin{pmatrix} \cos(-\omega t + \vartheta) \\ \sin(-\omega t + \vartheta) \end{pmatrix} \tag{A.13}$$

[2] appendix to the sections 2.5.5 and 6.3

with the same phase shift, $\vartheta$, for both phasors. Since the phase shift represents nothing more than the angle between $x$-axis and phasor at the time $t = 0$, it can be eliminated by rotating the coordinate system by the angle $-\vartheta$. (A positive angle implies counterclockwise rotation and a negative angle implies clockwise rotation.) Then, inserting the universal relationships $\cos(-\alpha) = \cos(\alpha)$ and $\sin(-\alpha) = -\sin(\alpha)$ yields the following sum of the two phasors:

$$\underline{P} \;=\; \begin{pmatrix} X \\ Y \end{pmatrix} \;=\; \begin{pmatrix} (r_1 + r_2)\ \cos(\omega t) \\ (r_1 - r_2)\ \sin(\omega t) \end{pmatrix} \tag{A.14}$$

With $\cos^2(\alpha) + \sin^2(\alpha) = 1$ valid for any angle $\alpha$, (A.14) can be transformed to

$$\frac{X^2}{(r_1 + r_2)^2} + \frac{Y^2}{(r_1 - r_2)^2} \;=\; 1\ , \tag{A.15}$$

which is an ellipse equation. $r_1 + r_2 = A \geq 0$ is the semi-major axis, $r_1 - r_2 = B$ the semi-minor axis. The ratio of $r_1$ and $r_2$ determines the ellipticity, $\varepsilon = B/A$, and, hence, the shape and the sense of rotation of the ellipse:

| ratio | ellipticity | shape | sense of rotation |
|---|---|---|---|
| $0 = r_2 < r_1$ | $\varepsilon = 1$ | circle | counterclockwise |
| $0 < r_2 < r_1$ | $0 < \varepsilon < 1$ | general ellipse | counterclockwise |
| $0 \neq r_1 = r_2$ | $\varepsilon = 0$ | straight line | (degenerate) |
| $0 < r_1 < r_2$ | $-1 < \varepsilon < 0$ | general ellipse | clockwise |
| $0 = r_1 < r_2$ | $\varepsilon = -1$ | circle | clockwise |

The ellipse generated in Fig. A.2 exhibits a counterclockwise sense of rotation since the longer phasor (red) turns in that direction.

## A.3 One-Point Two-Layer Model for a Kelvin Wave[3]

The linearised shallow water equations (A.1) are now extended towards a linear one-point two-layer system. The surface layer is denoted by a subscript $\mathrm{s}$ and the bottom layer by a subscript $\mathrm{b}$. Friction is again neglected except for the bottom drag; the associated linear drag coefficient is denoted by $c_\mathrm{d}$ and has the unit of a frequency. Derivatives are abbreviated by a single $\partial$, e.g. $\partial_t u_\mathrm{s} = \partial u_\mathrm{s}/\partial t$.

$$\partial_t u_\mathrm{s} - f v_\mathrm{s} \;=\; -g\partial_x \eta \tag{A.16}$$
$$\partial_t v_\mathrm{s} + f u_\mathrm{s} \;=\; -g\partial_y \eta \tag{A.17}$$
$$\partial_t u_\mathrm{b} - f v_\mathrm{b} \;=\; -g\partial_x \eta - c_\mathrm{d} u_\mathrm{b} \tag{A.18}$$
$$\partial_t v_\mathrm{b} + f u_\mathrm{b} \;=\; -g\partial_y \eta - c_\mathrm{d} v_\mathrm{b} \tag{A.19}$$

[3] appendix to the sections 2.5.5 and 6.3

For simplicity, let the two layers have equal thicknesses, $h_s = h_b = H/2$. The vertically averaged velocities have to agree with the first two equations of (A.9), i.e.

$$(u_\mathrm{s} + u_\mathrm{b})/2 = 0 \implies u_\mathrm{b} = -u_\mathrm{s} \tag{A.20}$$

$$(v_\mathrm{s} + v_\mathrm{b})/2 = v_0(x,\ y)\ \cos(\omega t) \implies v_\mathrm{b} = -v_\mathrm{s} + 2v_0\ \cos(\omega t)\ . \tag{A.21}$$

Inserting these substitutions into (A.18) and (A.19) results in

$$-\partial_t u_\mathrm{s} + f v_\mathrm{s} - 2 f v_0\ \cos(\omega t) = -g\partial_x \eta + c_\mathrm{d} u_\mathrm{s} \tag{A.22}$$

$$-\partial_t v_\mathrm{s} - 2v_0\omega\ \sin(\omega t) - f u_\mathrm{s} = -g\partial_y \eta + c_\mathrm{d} v_\mathrm{s} - 2c_\mathrm{d} v_0\ \cos(\omega t)\ . \tag{A.23}$$

Then [(A.16) − (A.22)]/2 and [(A.17) − (A.23)]/2 are calculated:

$$\partial_t u_\mathrm{s} - f v_\mathrm{s} + f v_0\ \cos(\omega t) = -\frac{c_\mathrm{d}}{2} u_\mathrm{s} \tag{A.24}$$

$$\partial_t v_\mathrm{s} + f u_\mathrm{s} + v_0\omega\ \sin(\omega t) = -\frac{c_\mathrm{d}}{2} v_\mathrm{s} + c_\mathrm{d} v_0\ \cos(\omega t) \tag{A.25}$$

The second of these two equations is multiplied by the imaginary unit, i, and then added to the first. Further on, a complex velocity is defined as $V = u_\mathrm{s} + \mathrm{i}v_\mathrm{s}$ (i.e. $\mathrm{i}V = \mathrm{i}u_\mathrm{s} - v_\mathrm{s}$) and inserted into the result:

$$\partial_t V + \left[\frac{c_\mathrm{d}}{2} + \mathrm{i}f\right] V = -\mathrm{i}v_0\omega\ \sin(\omega t) + [\mathrm{i}c_\mathrm{d} - f] v_0\ \cos(\omega t) \tag{A.26}$$

An ansatz for $V$ is

$$V = A\ \exp(\mathrm{i}\omega t) + B\ \exp(-\mathrm{i}\omega t) \tag{A.27}$$

such that

$$\partial_t V = \mathrm{i}\omega A\ \exp(\mathrm{i}\omega t) - \mathrm{i}\omega B\ \exp(-\mathrm{i}\omega t)\ ; \tag{A.28}$$

the trigonometric functions can be rewritten as

$$\cos(\alpha) = \frac{1}{2}\left[\exp(\mathrm{i}\alpha) + \exp(-\mathrm{i}\alpha)\right] \tag{A.29}$$

$$\sin(\alpha) = \frac{1}{2\mathrm{i}}\left[\exp(\mathrm{i}\alpha) - \exp(-\mathrm{i}\alpha)\right]\ . \tag{A.30}$$

Inserting the equations (A.27), (A.28), (A.29) and (A.30) into (A.26) and sorting with respect to the exponential function's argument give

$$\begin{aligned} &\left\{\left[\frac{c_\mathrm{d}}{2} + \mathrm{i}(f+\omega)\right] A - \mathrm{i}\frac{v_0}{2}\left[c_\mathrm{d} + \mathrm{i}(f+\omega)\right]\right\}\ \exp(\mathrm{i}\omega t) \\ = &\left\{-\left[\frac{c_\mathrm{d}}{2} + \mathrm{i}(f-\omega)\right] B + \mathrm{i}\frac{v_0}{2}\left[c_\mathrm{d} + \mathrm{i}(f-\omega)\right]\right\}\ \exp(-\mathrm{i}\omega t)\ . \end{aligned} \tag{A.31}$$

Since this equation has to be valid for any time $t$, the curly brackets have to vanish. From this it follows:

$$A = \mathrm{i}\frac{v_0}{2}\,\frac{c_\mathrm{d}+\mathrm{i}(f+\omega)}{\frac{c_\mathrm{d}}{2}+\mathrm{i}(f+\omega)} = \mathrm{i}\frac{v_0}{2}\,\frac{2a+\mathrm{i}b_+}{a+\mathrm{i}b_+} = \mathrm{i}\frac{v_0}{2}\left[1+a\,\frac{a-\mathrm{i}b_+}{a^2+b_+^2}\right] \quad \text{(A.32)}$$

$$B = \mathrm{i}\frac{v_0}{2}\,\frac{c_\mathrm{d}+\mathrm{i}(f-\omega)}{\frac{c_\mathrm{d}}{2}+\mathrm{i}(f-\omega)} = \mathrm{i}\frac{v_0}{2}\,\frac{2a+\mathrm{i}b_-}{a+\mathrm{i}b_-} = \mathrm{i}\frac{v_0}{2}\left[1+a\,\frac{a-\mathrm{i}b_-}{a^2+b_-^2}\right] \quad \text{(A.33)}$$

where the abbreviations $a = c_\mathrm{d}/2$ and $b_\pm = f \pm \omega$ have been introduced for convenience. Considering again the definition of $V$ and its ansatz (A.27), it is clear that

$$u_\mathrm{s} = \mathrm{Re}(V) = \mathrm{Re}(A\ \exp(\omega t)) + \mathrm{Re}(B\ \exp(-\omega t)) \quad \text{(A.34)}$$

$$v_\mathrm{s} = \mathrm{Im}(V) = \mathrm{Im}(A\ \exp(\omega t)) + \mathrm{Im}(B\ \exp(-\omega t)) \quad \text{(A.35)}$$

and with $\exp(\pm\alpha) = \cos(\alpha) \pm \mathrm{i}\sin(\alpha)$ (cp. eq.s (A.29) and (A.30)), the surface velocity components result in

$$u_\mathrm{s} = \frac{v_0}{2}\left\{a\left[\frac{b_+}{a^2+b_+^2}+\frac{b_-}{a^2+b_-^2}\right]\cos(\omega t) + a^2\left[-\frac{1}{a^2+b_+^2}+\frac{1}{a^2+b_-^2}\right]\sin(\omega t)\right\} \quad \text{(A.36)}$$

$$v_\mathrm{s} = \frac{v_0}{2}\left\{\left(2+a^2\left[\frac{1}{a^2+b_+^2}+\frac{1}{a^2+b_-^2}\right]\right)\cos(\omega t) + a\left[\frac{b_+}{a^2+b_+^2}-\frac{b_-}{a^2+b_-^2}\right]\sin(\omega t)\right\}\ . \quad \text{(A.37)}$$

Inserting in (A.20) and (A.21) yields the bottom velocity components:

$$u_\mathrm{b} = -\frac{v_0}{2}\left\{a\left[\frac{b_+}{a^2+b_+^2}+\frac{b_-}{a^2+b_-^2}\right]\cos(\omega t) + a^2\left[-\frac{1}{a^2+b_+^2}+\frac{1}{a^2+b_-^2}\right]\sin(\omega t)\right\} \quad \text{(A.38)}$$

$$v_\mathrm{b} = -\frac{v_0}{2}\left\{\left(-2+a^2\left[\frac{1}{a^2+b_+^2}+\frac{1}{a^2+b_-^2}\right]\right)\cos(\omega t) + a\left[\frac{b_+}{a^2+b_+^2}-\frac{b_-}{a^2+b_-^2}\right]\sin(\omega t)\right\} \quad \text{(A.39)}$$

An example is shown in Fig. A.3.

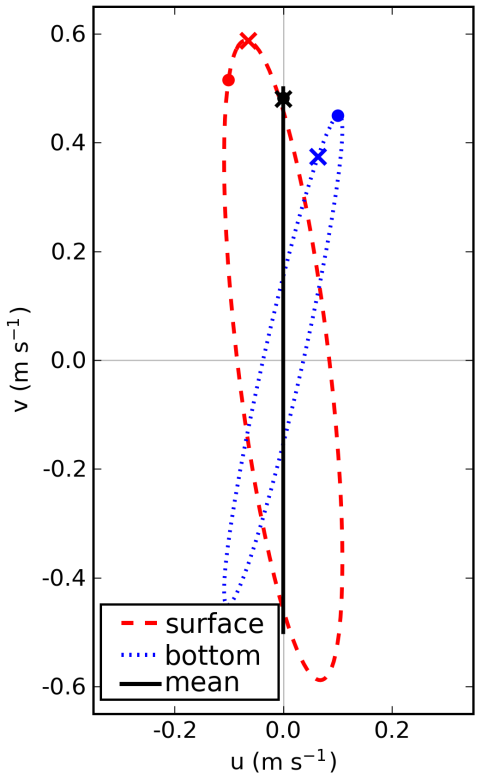


**Figure A.3:** Surface, bottom and depth-averaged tidal current ellipse according to equations (A.36) to (A.39). The current vectors trace out the long way from $\times$ to $\bullet$, i.e. the surface ellipse exhibits a clockwise, the bottom ellipse a counterclockwise sense of rotation. The vertically averaged tidal current is rectilinear and coast-parallel. The parameters have been set as follows: $v_0 = 0.5$ m/s, $c_\mathrm{d} = 5 \cdot 10^{-5}$/s, $f = 1 \cdot 10^{-4}$/s, $\omega = 2\pi/(44,714$ s).

# List of Tables



# List of Figures

# References


Avicola, G. and P. Huq, 2003a: The characteristics of the recirculating bulge region in coastal buoyant outflows. *J. Mar. Res.*, **61**, 435–463.

— 2003b: The role of outflow geometry in the formation of the recirculating bulge region in coastal buoyant outflows. *J. Mar. Res.*, **61**, 411–434.

Backx, J. J. G. M., G. van der Berg, N. Geilen, A. de Hoog, E. J. Houwing, M. Ohm, M. van Oirschot, and M. van Wijngaarden, 2002: Heavily Modified Waters in Europe, Case Study on the Haringvliet Estuary.
URL `http://www.sepa.org.uk/hmwbworkinggroup/studies/netherlands/haringvliet.pdf`

Banas, N. S. and B. M. Hickey, 2005: Mapping exchange and residence time in a model of Willapa Bay, Washington, a branching, microtidal estuary. *J. Geophys. Res.*, **110**.

Bormans, M. and C. Garrett, 1989: A simple criterion for gyre formation by the surface outflow from a strait, with application to the Alboran Sea. *J. Geophys. Res.*, **84**, 3733–3742.

Bowden, K. F., 1983: *Physical oceanography of coastal waters*. Ellis Horwood Ltd., Chichester.

Burchard, H., 2008: Combined effects of wind, tide and horizontal density gradients on stratification in estuaries and coastal seas. *J. Phys. Oceanogr.*, submitted.

Burchard, H. and K. Bolding, 2001: Comparative analysis of four second-moment turbulence closure models for the oceanic mixed layer. *J. Phys. Oceanogr.*, **31**, 1943–1968.

— 2002: GETM – a general estuarine transport model. Scientific documentation. Technical Report EUR 20253 EN, European Commission.

Burchard, H., K. Bolding, and M. R. Villarreal, 2004: Three-dimensional modelling of estuarine turbidity maxima in a tidal estuary. *Ocean Dyn.*, **54**, 250–265.

Burchard, H., G. Flöser, J. V. Staneva, R. Riethmüller, and T. Badewien, 2008: Impact of density gradients on net sediment transport into the Wadden Sea. *J. Phys. Oceanogr.*, **38**, 566–587.

Burchard, H., F. Janssen, K. Bolding, L. Umlauf, and H. Rennau, 2009: Model simulations of dense bottom currents in the Western Baltic Sea. *Cont. Shelf Res.*, in print.

Burchard, H., H. Lass, V. Mohrholz, L. Umlauf, J. Sellschopp, V. Fiekas, K. Bolding, and L. Arneborg, 2005: Dynamics of medium-intensity dense water plumes in the Arkona Sea, Western Baltic Sea. *Ocean Dyn.*, **55**, 391–402.

Burchard, H. and L. Umlauf, 2007: *Turbulence in natural waters*. Lecture notes on Marine Turbulence, Leibniz Institute for Baltic Sea Research at the University of Rostock.
URL `http://www.io-warnemuende.de/homepages/wgburchard/index.php?Itemid=83`

Carbajal, N., 2000: A criterion to locate regions with anticyclonic tidal current rotation. *Cont. Shelf Res.*, **20**, 281–292.

Cheng, Y., V. M. Canuto, and A. M. Howard, 2002: An improved model for the turbulent PBL. *J. Atmos. Sci.*, **59**, 1550–1565.

de Boer, G. J., J. D. Pietrzak, and J. C. Winterwerp, 2006: On the vertical structure of the Rhine region of freshwater influence. *Ocean Dyn.*, **56**, 198–216.

— 2008: Using the potential energy anomaly equation to investigate tidal straining and advection of stratification in a region of freshwater influence. *Ocean Model.*, **22**, 1–11.

de Jonge, V. N., 1990: Response of the Dutch Wadden Sea ecosystem to phosphorus discharges from the River Rhine. *Hydrobiologia*, **195**, 49–62.

de Ruijter, W. P. M., A. van der Giessen, and F. C. Groenendijk, 1992: Current and density structure in the Netherlands coastal zone. *Dynamics and Exchanges in Estuaries and the Coastal Zone*, D. Prandle, ed., volume 40 of *Coastal and Estuarine Studies*, 529–550.

de Ruijter, W. P. M., A. W. Visser, and W. G. Bos, 1997: The Rhine outflow: A prototypical pulsed discharge plume in a high energy shallow sea. *J. Mar. Sys.*, **12**, 263–276.

Dewey, R. K., W. R. Crawford, A. E. Gargett, and N. S. Oakey, 1987: A microstructure instrument for profiling oceanic turbulence in coastal bottom boundary layers. *J. Atmos. Ocean. Tech.*, **4**, 288–297.

Fischer, H. B., E. J. List, R. C. Y. Koh, J. Imberger, and N. H. Brooks, 1979: *Mixing in inland and coastal waters*. Academic Press, London.

Fisher, N. R., J. H. Simpson, and M. J. Howarth, 2002: Turbulent dissipation in the Rhine ROFI forced by tidal flow and wind stress. *J. Sea Res.*, **48**, 249–258.

Garvine, R. W., 1995: A dynamical system for classifying buoyant coastal discharges. *Cont. Shelf Res.*, **15**, 1585–1596.

Hessner, K., A. Rubino, P. Brandt, and W. Alpers, 2001: The Rhine outflow plume studied by the analysis of synthetic aperture radar data and numerical simulations. *J. Phys. Oceanogr.*, **31**, 3030–3044.

Hetland, R. D., 2008: The effects of mixing and spreading on density in near-field river plumes. *Dyn. Atmos. Oceans*, doi:10.1016/j.dynatmoce.2008.11.003.

Hofmeister, R., 2006: *Model studies on stratification in the Limfjord*. Diploma thesis, Leibniz Institute for Baltic Sea Research at the University of Rostock.
URL `http://www.io-warnemuende.de/homepages/wgburchard/index.php?Itemid=83`

Kundu, P. K. and I. M. Cohen, 2002: *Fluid Mechanics*. Academic Press, San Diego, London, second edition.

Laane, R. W. P. M., 2005: Applying the critical load concept to the nitrogen load of the river Rhine to the Dutch coastal zone. *Estuar. Coast. Shelf Sci.*, **62**, 487–493.

Lesieur, M., 1997: *Turbulence in fluids*, volume 40 of *Fluid mechanics and its applications*. Kluwer Academic Publ., Dordrecht, 3rd edition, 515 pp.

Mellor, G. L. and T. Yamada, 1974: A hierarchy of turbulence closure models for planetary boundary layers. *J. Atmos. Sci.*, **31**, 1791–1806.

— 1982: Development of a turbulence closure model for geophysical fluid problems. *Rev. Geophys. Space Phys.*, **20**, 851–875.

Nienhuis, P. H., 1992: Eutrophication, water management, and the functioning of Dutch estuaries and coastal lagoons. *Estuaries*, **15**, 538–548.

Pietrzak, J., 1998: The use of TVD limiters for forward-in-time upstream-biased advection schemes in ocean modeling. *Mon. Weather Rev.*, **126**, 812–830.

Prandle, D., 1982: The vertical structure of tidal currents. *Geophys. Astrophys. Fluid Dyn.*, **22**, 29–49.

Reynolds, O., 1895: On the dynamical theory of incompressible viscous fluids and the determination of the criterion. *Phil. Trans. R. Soc. Lond. A*, **186**, 123–164.

Rippeth, T. P., N. R. Fisher, and J. H. Simpson, 2001: The cycle of turbulent dissipation in the presence of tidal straining. *J. Phys. Oceanogr.*, **31**, 2458–2471.

Simpson, J. H., 1997: Physical processes in the ROFI regime. *J. Mar. Sys.*, **12**, 3–15.

Simpson, J. H., W. G. Bos, F. Schirmer, A. J. Souza, T. P. Rippeth, S. E. Jones, and D. Hydes, 1993: Periodic stratification in the Rhine ROFI in the North Sea. *Oceanolog. Acta*, **16**, 23–32.

Simpson, J. H., J. Brown, J. Matthews, and G. Allen, 1990: Tidal straining, density currents, and stirring in the control of estuarine stratification. *Estuaries*, **13**, 125–132.

Soulsby, R. L., 1990: Tidal-current boundary layers. *The Sea*, **9A**, 523–566.

Souza, A. J., N. R. Fisher, J. H. Simpson, and M. J. Howarth, 2008: Effects of tidal straining on the semidiurnal cycle of dissipation in the Rhine region of freshwater influence: Comparison of model and measurements. *J. Geophys. Res.*, **113**, C01011, doi:10.1029/2006JC004002.

Souza, A. J. and I. D. James, 1996: A two-dimensional (x-z) model of tidal straining in the Rhine ROFI. *Cont. Shelf Res.*, **16**, 949–966.

Souza, A. J. and J. H. Simpson, 1996: The modification of tidal ellipses by stratification in the Rhine ROFI. *Cont. Shelf Res.*, **16**, 997–1007.

— 1997: Controls on stratification in the Rhine ROFI system. *J. Mar. Sys.*, **12**, 311–323.

Souza, A. J., J. H. Simpson, and F. Schirmer, 1997: Current structure in the Rhine region of freshwater influence. *J. Mar. Res.*, **55**, 277–292.

Stanev, E. V., J.-O. Wolff, H. Burchard, K. Bolding, and G. Flöser, 2003: On the circulation in the East Frisian Wadden Sea: Numerical modelling and data analysis. *Ocean Dynamics*, **53**, 27–51.

Staneva, J., E. V. Stanev, J.-O. Wolff, T. H. Badewien, R. Reuter, B. Flemming, A. Bartholomä, and K. Bolding, 2009: Hydrodynamics and sediment dynamics in the German Bight. A focus on observations and numerical modelling in the East Frisian Wadden Sea. *Cont. Shelf Res.*, in print.

Stips, A., T. Pohlmann, K. Bolding, and H. Burchard, 2004: Simulating the temporal and spatial dynamics of the North Sea using the new model GETM (General Estuarine Transport Model). *Ocean Dyn.*, **54**, 266–283.

Umlauf, L. and H. Burchard, 2003: A generic length-scale equation for geophysical turbulence models. *J. Mar. Res.*, **61**, 235–265.

Umlauf, L., H. Burchard, and K. Bolding, 2005: General Ocean Turbulence Model. Source code documentation. Technical Report 63, Leibniz Institute for Baltic Sea Research, Warnemünde, Germany.

Umlauf, L. and U. Lemmin, 2005: Inter-basin exchange and mixing in the hypolimnion of a large lake: the role of long internal waves. *Limnol. Oceanogr.*, **50**, 1601–1611.

van Alphen, J. S. L. J., W. P. M. de Ruijter, and J. C. Borst, 1988: Outflow and three-dimensional spreading of Rhine river water in the Netherlands coastal zone. *Physical Processes in Estuaries*, J. Dronkers and W. van Leussen, eds., Springer, Berlin, 70–92.

van der Giessen, A., W. P. M. de Ruijter, and J. C. Borst, 1990: Three-dimensional current structure in the Dutch coastal zone. *Neth. J. Sea Res.*, **25**, 45–55.

Visser, A. W., A. J. Souza, K. Hessner, and J. H. Simpson, 1994: The effect of stratification on tidal current profiles in a region of freshwater influence. *Oceanolog. Acta*, **17**, 369–381.

Visser, M., W. P. M. de Ruijter, and L. Postma, 1991: The distribution of suspended matter in the Dutch coastal zone. *Neth. J. Sea Res.*, **27**, 127–143.

Wiseman, W. J., Jr. and R. W. Garvine, 1995: Plumes and coastal currents near large river mouths. *Estuaries*, **18**, 509–517.

Xia, Z., N. Carbajal, and J. Südermann, 1995: Tidal current amphidromic system in semi-enclosed basins. *Cont. Shelf Res.*, **15**, 219–240.

Yankovsky, A. E. and D. C. Chapman, 1997: A simple theory for the fate of buoyant coastal discharges. *J. Phys. Oceanogr.*, **27**, 1386–1401.

# Declaration According to the Examination Regulations §17(5)

I hereby declare that I have written this thesis without any help from others with the exception of the first two paragraphs of section 5.4, which have been written by Hans Burchard (Warnemünde, Germany).
I further declare that I have used no sources and auxiliary means others than those mentioned.

Rostock, 5 January 2009 Elisabeth Fischer